Structural Design of a 6-DoF Hip Exoskeleton using Linear Series Elastic Actuators

Xiao Li

Thesis submitted to the Faculty of the
Virginia Polytechnic Institute and State University
in partial fulfillment of the requirements for the degree of

Master of Science
in
Mechanical Engineering

Alexander Leonessa, Chair
Alan T. Asbeck, Co-Chair
Steve C. Southward

4 August 2017
Blacksburg, Virginia

Structural Design of a 6-DoF Hip Exoskeleton using Linear Series Elastic Actuators

Xiao Li

(ACADEMIC ABSTRACT)

A novel hip exoskeleton with six degrees of freedom (DoF) was developed, and multiple prototypes of this product were created in this thesis. The device was an upper level of the 12-DoF lower-body exoskeleton project, which was known as the Orthotic Lower-body Locomotion Exoskeleton (OLL-E). The hip exoskeleton had three motions per leg, which were roll, yaw, and pitch. Currently, the sufferers of hemiplegia and paraplegia can be addressed by using a wheelchair or operating an exoskeleton with aids for balancing. The motivation of the exoskeleton project was to allow paraplegic patients to walk without using aids such as a walker or crutches. In mechanical design, the hip exoskeleton was developed to mimic the behavior of a healthy person closely.

The hip exoskeleton will be fully powered by a custom linear actuator for each joint. To date, there are no exoskeleton products that are designed to have all of the hip joints powered. Thus, packaging of actuators was also involved in the mechanical design of the hip exoskeleton. As a result, the output torque and speed for the roll joint and yaw joint were calculated. Each hip joint was structurally designed with properly selected bearings, encoder, and hard stops. Their range of motions met desired requirements. In addition, a backpack assembly was designed for mounting the hardware, such as cooling pumps, radiators, and batteries. In the verification part, finite element analysis (FEA) was conducted to show the robustness of the structural design. For fit testing, three wearable prototypes were produced to verify design choices. As a result, the weight of the current hip exoskeleton was measured as 32.1 kg.

Structural Design of a 6-DoF Hip Exoskeleton using Linear Series Elastic Actuators

Xiao Li

(GENERAL AUDIENCE ABSTRACT)

Currently, patients who suffer from paraplegia are commonly treated with wheelchairs. However, the drawbacks of using wheelchairs introduced new medical challenges. One of the medical issues is the decrease in bone density. To address these medical problems and increase the quality of life of patients, lower-body exoskeletons are produced to assist with walking. To date, most of the current exoskeleton products require aids for balancing patients' walking, and they don't have fully actuated joints at the hip. As for the hip exoskeleton introduced in this thesis, all of the hip joints will be powered. Also, this device was the upper design of the Orthotic Lower-body Locomotion Exoskeleton (OLL-E), which aimed to create a self-balancing exoskeleton with total 12 of lower-body joints powered. The final goal of OLL-E is to assist the patient to walk at normal human speed without using aids.

This thesis discusses the process of designing a hip exoskeleton, which starts from requirements development to modeling and prototype tests. The conservative calculations and assumptions made in this paper guided the structural design of the hip exoskeleton. The robustness of the structures was ensured with rigorous finite element analysis. In the end, wearable prototypes were produced to examine the fitting tests. Overall, this design of the hip exoskeleton provided critical references for the future development of the OLL-E.

Contents

List of Figures

List of Tables

Chapter 1

Introduction

Lower-body exoskeletons have become popular in the field of medical rehabilitation, orthotics, and human augmentation. As rehabilitation devices, several exoskeleton products have been developed to help spinal cord injuries (SCIs) and strokes patients, such as Lokomat [14], ReWalk [15], and HAL [16]. For moderate SCI patients, exoskeletons can serve as orthotics to aid in walking. Vanderbilt University developed the hip and knee joints, which coupled orthosis with the hybrid functional electrical simulation (FES) approach to command position trajectories [17]. Another application of exoskeletons can be used to improve human strength and endurance. However, the operators of these types of exoskeletons are required to be in good physical condition. The University of California, Berkeley produced an exoskeleton named BLEEX, which improved the user's strength and endurance for carrying payloads during locomotion [3, 18].

The topic of this thesis is a part of the NSF funded research project, which is developing a 12-DoF, self-balancing, compliant lower-body robotic orthotic, known as the Orthotic Lower-body Locomotion Exoskeleton (OLL-E). The hip exoskeleton is the upper level design of the OLL-E and will be integrated with the lower level design. In this thesis, there was a total of six DoF at the hip exoskeleton and three DoF per leg (roll, yaw, and pitch). Each joint will be powered by a linear actuator.

1.1 Motivation

Limited mobility can be caused by many conditions, such as muscle contractions, cerebral palsy, stroke, or polio syndrome. One of the most damaging and profound influences on human lives is spinal cord injuries. Traumatic SCIs can be caused by any number of incidents including motor vehicle accidents (36-48%), violence (5-29%), falls (17-21%), and recreational activities (7-16%), and 10,000 new cases are reported every year in the USA [19]. Furthermore, SCIs can result in paraplegia for patients and cause serious health ramifi-

cations, such as decreased bone density, decreased muscle tone, obesity, and impaired bowel and bladder function [15].

One common treatment for those who suffer from hemiplegia and paraplegia with mobility limitations is using a wheelchair. However, there are a set of new medical issues and concerns for wheelchair-dependent users. These users spend most of their daily time sitting on wheelchairs for mobility at home, school, work, and play. Upper extremity pain can be developed due to chronic overuse of upper weight-bearing activities, which can lead to soft tissue disorders and degenerative changes in the shoulder joints [20]. In addition, long-time use of wheelchairs with seated position can lead to loss of the rate of bone density [21] and pressure sores [22]. Research in the emerging field of exoskeletons has been directed at addressing the medical challenges of traditional physical therapy.

The common purpose of lower-body exoskeletons is to provide aids for those patients with limited mobility and improve their health and quality of life. However, most exoskeletons today only actuate 4 to 8 DoF total and are not capable of balancing without the use of aids. The drawbacks of using aids for balancing include increased burdens on upper body when leaning some of the body weight, and the reduced ability of patients to perform manipulation tasks. The overall NSF project of OLL-E will develop a 12-DoF fully actuated self-balancing lower-body exoskeleton. With the novel mechanisms and compliant linear series elastic actuators (LSEAs), each DoF of the exoskeleton will match with human joints, and a high fidelity impedance control will be implemented on the whole lower body. The LSEAs can provide compliant interaction during fore-controlled at each joint and walk with state-of-the-art whole-body control techniques. In this thesis, the hip roll and yaw joints were both force-controlled with custom linear actuators in addition to the pitch joint. The force control of the yaw joint allowed for balancing control in the transverse plane of the exoskeleton. The design of frame structures of the hip exoskeleton not only collocated exoskeleton and human joints, but provided packaging designs for actuators.

1.1.1 Humanoids at TREC

In the TREC lab at Virginia Tech, there were three force-controlled humanoid robots: SAF-FiR, the Shipboard Autonomous Firefighting Robot [23], THOR, the Tactical Hazardous Operations Robot [24], and ESCHER, the Electric Series Compliant Humanoid for Emergency Response [1]. These robots all had the high-performance design of LSEAs. The design of LSEAs on THOR had a cantilevered beam as an elastic element, which paralleled with high-precision ball screw, and was capable of exerting a peak load of 2225 N [2]. The custom actuators design on OLL-E leveraged the experiences from the THOR's LSEA design. The most recent self-balancing humanoid robot, ESCHER, which participated the competition DARPA Robotics Challenge (DRC) finals, was standing 1.78 m tall and weighing 77.5 kg with 38 DoFs, as shown in Fig. 1.1 [1]. OLL-E will have the same number of powered DoF as ESCHER's lower body and have the similar configurations of the actuators as ESCHER had.

The design of the OLL-E used some reference data from ESCHER including the powered joint placements, segments masses, and inertias.

1-DOF Spinning LIDAR
2-DOF Neck
3-DOF Shoulder
1-DOF Waist
1-DOF Elbow
3-DOF Hip
3-DOF Wrist
4-DOF Hand
1-DOF Knee
2-DOF Ankle
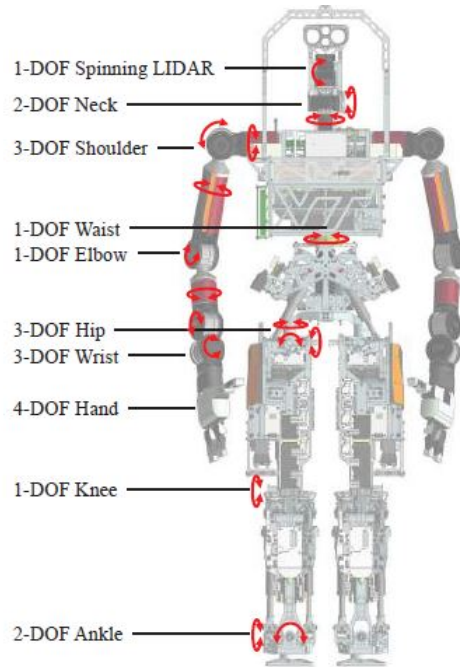
Figure 1.1: Overview of ESCHER's degrees of freedom [1].

1.2 Literature Review

The research of lower-body exoskeletons can be traced back to the 1970s with the development of a 6-DoF complete active exoskeleton at the Mihailo Pupin Institute in Belgrade by Miomir Vukobratovic et al [25]. The joints were actuated by a large pneumatic double-acting cylinder with a peak force of about 1100 N, and the joint positions were detected by linear feedback potentiometers. This exoskeleton could only do gait walking on level ground stabilized by supporting cranes.

Since the 1990s, University of Tsukuba started to develop Hybrid Assistive Limbs (HAL), which currently has five generations [26, 27]. HAL-3 ad 4 researched on the abilities to help disabled people regain normal activities. HAL-5 had both lower and upper body to augment the operator's strength and endurance. There were 3 DoFs per leg (hip, knee, and foot, respectively), and only hip and knee joints were powered with actuators that had DC Servo motor with harmonic drive [28]. The control method of HAL was to produce muscle contraction torque following the operator's intention by referring to the myoelectricity (EMG) [28, 29, 30, 31, 32, 33, 34, 35, 36]. HAL-5 (Type-B) that had the same number DoFs

3

as HAL-3 could hold and lift heavy objects up to 70 kg with a continuously operating time of 2 hours 40 minutes [27].

Berkeley Lower Extremity Exoskeleton (BLEEX) was the first exoskeleton capable of independent motion, and in the meantime, provided augmentation for the operator [18, 37, 38, 39, 40, 41, 42]. The BLEEX had 7 DoFs per leg: 3 DoFs at the hip, 1 DoF at the knee, and 3 DoFs at the ankle. However, only four of them were actuated: hip pitch and roll joints, knee joint, and ankle pitch joint. The rest of DoFs were passive by using springs and elastomers. The BLEEX design requirements were pseudo-anthropomorphic and developed by using Clinical Gait Analysis (CGA) to achieve similar limb masses and inertias to a human. Overall, the BLEEX could be driven by a 75 kg operator and walked at the average speed of 0.9 m/s with 34 kg of payload. However, the actuators on the suit were hydraulic and provided a massive density of power (2.27 kW) for regular walking [37].

There are other exoskeletons providing gait assistance and rehabilitation, such as Lokomat and ReWalk. Lokomat provided a driven gait orthosis (DGO) for patients on an automated treadmill training [14]. The patient was fixed to the device with respect to the moving treadmill belt, and the hip and knee joints were controlled by a real-time system using a physiological gait pattern. Rewalk was a lower-body exoskeleton that provided rehabilitation for SCI patients [15]. The hip and knee joints were powered by DC motors with rechargeable batteries while the operator could only walk using crutches for balancing. A tilt sensor installed in the chest to sense the angle change of the torso, in order to generate alternating limb-coordinated motion. There are also several lower-body exoskeleton gait assistance products in the world, such as ARKE from Bionik Laboratories, EXO GT from Exo Bionics, REX from REX Bionics, and Phoenix from SuitX. Most of these exoskeletons were powered only at hip and knee joints with one DoF, separately, and they all required aids for balancing. Therefore, the development of OLL-E can be a breakthrough in achieving a better solution to assisting patients without the use of aids through a full lower-body self-balancing control.

1.3 Thesis Organization

This thesis mainly focuses on the developments of the architecture of the hip exoskeleton, which will be integrated with the lower level of the OLL-E. Chapter 2 contains the leaf spring analysis for the series linear actuator. Chapter 3 discusses the development of requirements of joints for OLL-E. Chapter 4 provides the mechanical designs for each joint at the hip, actuators packaging, and the design of the external backpack. Chapter 5 includes finite element analysis of some critical parts, bolts preload documentation, and tests with 3D printed wearable prototypes. Chapter 6 is a conclusion of this thesis including the recommendations of improving the design of the hip exoskeleton, and the future work can be done for the whole project.

Chapter 2

Contributions to Actuators Design

2.1 Leaf Spring Analysis

Currently, applications of SEAs are widespread in the field of robotics. The benefits of SEAs include high force fidelity, energy storage, low impedance and high force control bandwidth [43, 44, 45]. In addition, cantilevered springs have been used on numerous actuators as compliant elements [46, 47, 48]. The humanoid robots THOR and ESCHER at the TREC lab of Virginia Tech both have installed Linear Series Elastic Actuators (LSEAs) that had an elastic component between the actuator and the base [2, 1]. The elastic element was made of Titanium Ti-6Al-4V (Grade 5) acting as a cantilever beam. The titanium spring was mounted parallel to the linear actuator and connected with a lever arm, as shown in Fig. 2.1. This LSEA was designed by previous TREC member, Coleman Knabe. A load transmission was going from the ball nut to the center of the universal joint attached to the lever arm. This load was going to force the titanium beam in pure bending [2]. The peak force for the THOR hip LSEA was recorded as 2225 N with compliant 372 kN/m spring stiffness rate [2].
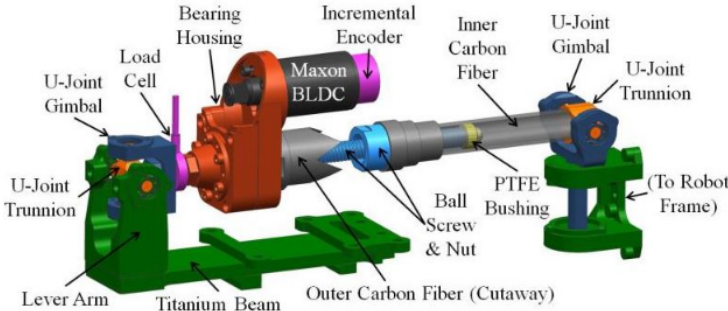
Figure 2.1: Rendering of the THOR Hip LSEA [2].

For this exoskeleton project, a single-motor LSEA could provide a maximum of 4649.7 N input load, which was about twice as much as the peak force from the THOR LSEA. Thus, a new design of a leaf spring was required to provide the compliance for the amount of load. The basic requirements for the design of the leaf spring were that the spring would not yield under 4649.7 N load and have enough compliance for energy storage.

The material of the leaf spring was determined to be Titanium Ti-6Al-4V (Ti Grade 5), Annealed because it has high strength and is well-known for use in applications subject to high-stress field [49]. According to the datasheet from MatWeb, the yield strength of Ti Grade 5 is 880 MPa, and the shear strength is 550 MPa [4], as shown in Table 2.1. In this section, four cases were analyzed to help determine the design of the leaf spring. One of the difficulties was to find out the dimensions of the leaf spring to meet the requirements. An EXCEL table was created with built-in equations to explore the results of different sizes of springs. Since there were three variables (span, width, and thickness), two variables needed to be fixed. The width of the spring could be set because it depended on the attached universal joints width, which was 40 mm. The span length and thickness of the spring needed to be attempted by trial and error. However, according to the maximum bending stress equation (2.1) and moment of inertia equation (2.2), it was easy to find out that the thickness of the beam's cross-section had a critical effect on the result of the bending stress. Thus, fixing the thickness of the beam first could help reduce significant change on the effect. For the compliance, the elastic stiffness of the leaf spring system ideally needed to achieve 500 N/mm.

$$f_{b-max} = \frac{Mc}{I} \tag{2.1}$$

$$I = \frac{bt^3}{12} \tag{2.2}$$

where M was the maximum bending moment, c was half of the beam thickness, I was the moment of inertia of beam section area, b was the width of the beam, and t was the thickness of the beam.

Table 2.1: Property of Titanium Grade 5 [4]

Property	Value
Tensile Yield Strength	880 MPa
Density	4.43 g/cm^3
Shear Strength	550 MPa
Modulus of Elasticity	113.8 GPa
Shear Modulus	44.0 GPa
Poisson's Ratio	0.342

Simple Cantilever Beam

The first case was a simple cantilever beam with one end fixed. A concentrated force was applied on the free end. Fig. 2.2 shows the leaf spring free body diagram (FBD) of the first case. The equation to determine the maximum deflection was shown in Eq. 2.3. The results of Case 1 are shown in Table 2.2. The highlighted row shows the limitation of the span length before the beam fails.
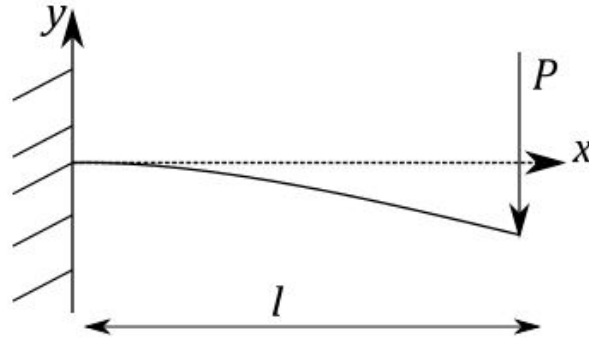
Figure 2.2: Configuration of simple cantilever beam in loading.

$$\delta_{max} = \frac{Pl^3}{3EI} \tag{2.3}$$

where δ_{max} is the maximum deflection of the beam, P is the concentrated load at the end of the beam, l is the span length of the beam, and E is the elastic modulus of the titanium.

Table 2.2: Results of simple cantilever beam

l (mm)	b (mm)	t (mm)	P (N)	δ_{max} (mm)	f_{b-max} (MPa)
⋮	⋮	⋮	⋮	⋮	⋮
115	40	10	4649.7	6.214	802.07
120	40	10	4649.7	7.060	836.95
125	40	10	4649.7	7.980	871.82
130	40	10	4649.7	8.977	906.69
⋮	⋮	⋮	⋮	⋮	⋮

7

Simple Supported Beam

The second case added a simple support after the fixed end of the beam. This could increase the stiffness of the beam. In order to increase the deflection, the thickness of the beam needed to be reduced. The thickness of this case was 8 mm. The FBD of the configuration of the beam is shown in Fig. 2.3. The distance a between the support and fixed end was small, so the deflection in this section could be negligible.
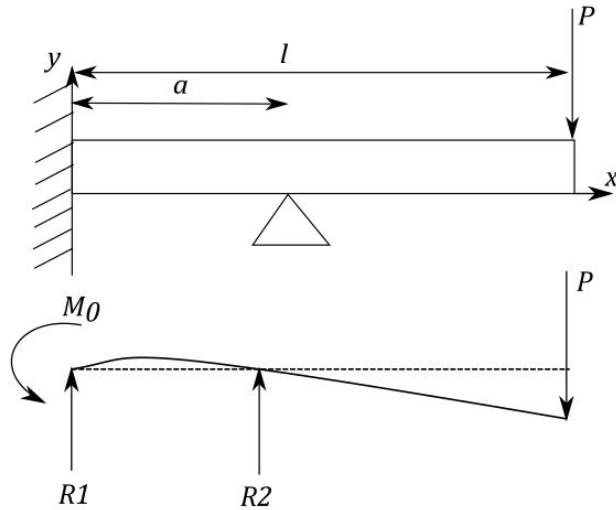
Figure 2.3: Configuration of simple supported beam in loading.

The reaction force at the fixed end of the beam was:

$$R_1 = \frac{3P(l-a)}{-2a} \tag{2.4}$$

The reaction force at the simple support was:

$$R_2 = P + \frac{3P(l-a)}{2a} \tag{2.5}$$

The reaction moment at the end of beam was:

$$M_0 = \frac{P(l-a)}{-2} \tag{2.6}$$

The deflection of the beam, δ could be derived in term of the length of beam, x:

$$EI\delta = \frac{-R_1 x^3}{6} - \frac{R_2(x-a)^3}{6} + \frac{M_0 x^2}{2} \tag{2.7}$$

From Eq. 2.7, the maximum deflection of this beam would happen at the end of the beam. The results of this beam configuration are shown in Table 2.3. The highlighted row indicates that the beam did not achieve the desired deflection before fail.

Table 2.3: Results of simple supported beam

l (mm)	b (mm)	t (mm)	a (mm)	P (N)	δ_{max} (mm)	f_{b-max} (MPa)
⋮	⋮	⋮	⋮	⋮	⋮	⋮
75	40	8	5	4649.7	2.884	762.84
80	40	8	5	4649.7	3.535	817.33
85	40	8	5	4649.7	4.277	871.82
90	40	8	5	4649.7	5.117	926.31
⋮	⋮	⋮	⋮	⋮	⋮	⋮

Z-shaped Spring

The third case was a Z-shaped configuration that had uniform cross section area with one end fixed, as shown in Fig. 2.4. The span length of OB and AC were assumed to be the same. The arm length of AB should be short in order to minimize the size of the whole configuration. The additional deflection at B gave an advantage of increasing the compliance of this configuration.
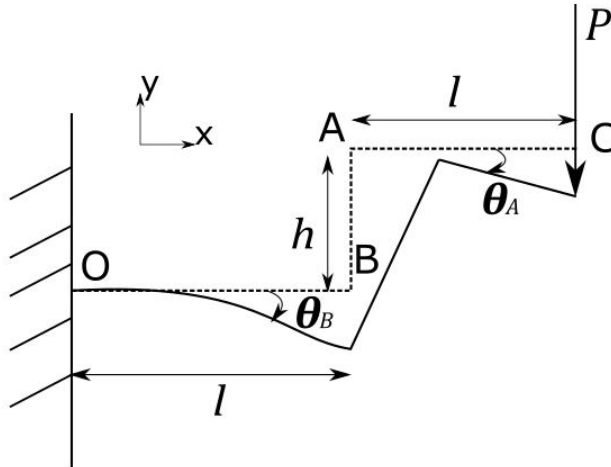
Figure 2.4: Configuration of Z-shaped spring in loading.

By superposition theorem, the deflection at C in x-axis was composed of two parts: the slope due to the force, P and moment, M_B, and the deflection due to moment, M_A. The deflection

9

at C in y-axis was superposed by the deflection of OB section, compression of AB section, and the deflection of AC section.

For OB section, the deflection in y-axis at B due to force, P was calculated as:

$$\triangle y_P = \left[\frac{Px^2}{6EI}(x - 3l) \right]_{x=l} = \frac{-Pl^3}{3EI} \tag{2.8}$$

The deflection in y-axis at B due to moment, $M_B = -Pl$, was expressed as:

$$\triangle y_{M_B} = \left[\frac{M_Bx^2}{2EI} \right]_{x=l} = \frac{M_Bl^2}{2EI} \tag{2.9}$$

Thus, the total deflection at B in y-direction by superposition theorem was:

$$\triangle y_{OB} = \triangle y_P + \triangle y_{M_B} \tag{2.10}$$

The slope, θ_B at B due to deflection was calculated as following:

$$\theta_B = \left\{ \frac{d}{dx} \left[\frac{Px^2}{6EI}(x - 3l) + \frac{M_Bx^2}{2EI} \right] \right\}_{x=l} = \left[\frac{Px}{6EI}(3x - 6l) + \frac{M_Bx}{EI} \right]_{x=l}$$
$$= \left\{ \frac{l}{2EI}[-Pl + 2M_B] \right\} \tag{2.11}$$

For AB section, the deflection in y-axis due axial load was calculated as:

$$\triangle y_{AB} = \frac{-Pl}{EA} \tag{2.12}$$

The deflection in x-axis due to moment at A, $M_A = -Pl$ was shown as:

$$\triangle x_{AB} = \left[\frac{M_Ax^2}{2EI} \right]_{x=l} = \frac{M_Al^2}{2EI} \tag{2.13}$$

The slope at A, θ_A due to the moment was expressed as:

$$\theta_A = \left[\frac{d}{dx} \left(\frac{M_Ax^2}{2EI} \right) \right]_{x=l} = \frac{M_Al}{EI} \tag{2.14}$$

For AC section, the deflection in y-axis due to load, P, was shown as following:

$$\triangle y_{AC} = \frac{-Pl^3}{3EI} \tag{2.15}$$

Therefore, the deflection of point C from nominal was:

$$\triangle C_x = \triangle x_{AB} + h\sin(\theta_B) \tag{2.16}$$
$$\triangle C_y = \triangle y_{OB} + \triangle y_{AB} + \triangle y_{AC} + h[1 - \cos(\theta_B)] + l\sin(\theta_A) \tag{2.17}$$

The overall magnitude of the deflection of point C was:

$$\delta_{max} = \sqrt{\triangle C_x^2 + \triangle C_y^2} \tag{2.18}$$

Eq. 2.1 was used to calculate the maximum bending stress, which happened at fixed point O. The results from different span lengths is shown in Table 2.4.

Table 2.4: Results of Z-shaped spring

l (mm)	b (mm)	t (mm)	h (mm)	P (N)	δ_{max} (mm)	f_{b-max}(MPa)
⋮	⋮	⋮	⋮	⋮	⋮	⋮
40	40	10	20	4649.7	1.650	557.96
45	40	10	20	4649.7	2.273	627.71
50	40	10	20	4649.7	3.035	697.46
55	40	10	20	4649.7	3.950	767.2
60	40	10	20	4649.7	5.032	836.95
65	40	10	20	4649.7	6.296	906.69
⋮	⋮	⋮	⋮	⋮	⋮	⋮

L-shaped Spring

The fourth case was an L-shaped configuration (Fig. 2.5), which was inspired by the leaf spring design from the THOR [2]. The entire configuration had uniform cross section area. The height of arm AB was 48 mm due to the size limit of the universal joint attached to the arm. The linear actuator that was parallel to the leaf spring axially loaded on the center of the universal joint. The deflection of point B was combined by the elongation of section OA in x-direction and the vertical deflection of section OA in y-direction.
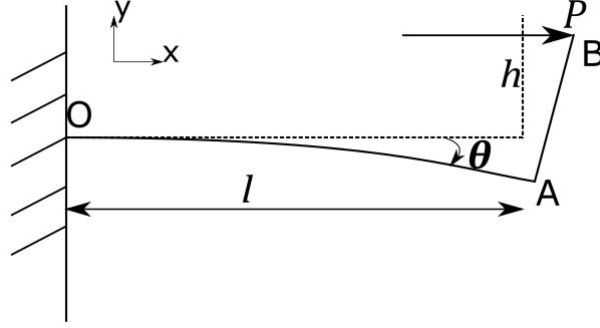
Figure 2.5: Configuration of L-shaped spring beam in loading.

The elongation of section OA was calculated as:

$$\triangle x_{OA} = \frac{-Pl}{EA} \tag{2.19}$$

The deflection of section OA due to the moment load at A, $M_A = -Ph$ was:

$$\triangle y_{OA} = \left[\frac{M_A x^2}{2EI}\right]_{x=l} = \frac{M_A l^2}{2EI} \tag{2.20}$$

The slope, θ at A due to the moment load was:

$$\theta = \left[\frac{d}{dx}\left(\frac{M_A x^2}{2EI}\right)\right]_{x=l} = \frac{M_A l}{EI} \tag{2.21}$$

Therefore, the deflection of point B from nominal was:

$$\triangle B_x = \triangle x_{OA} + h\sin(\theta) \tag{2.22}$$
$$\triangle B_y = \triangle y_{OA} + h[1 - \cos(\theta)] \tag{2.23}$$

The overall magnitude of the deflection of point B was:

$$\delta_{max} = \sqrt{\triangle B_x^2 + \triangle B_y^2} \tag{2.24}$$

The critical position of this design happened at the wall, O. Since this configuration had a fixed length of the arm AB, the moment load at the A was constant during the change of the beam's span length. Table 2.5 shows the results of deflections and bending stress of the leaf spring with different span lengths. Note that the highlighted row achieved an elastic stiffness of 522 N/mm.

Table 2.5: Results of L-shaped spring

l (mm)	b (mm)	t (mm)	h (mm)	P (N)	δ_{max} (mm)	f_{b-max}(MPa)
$\vdots$	$\vdots$	$\vdots$	$\vdots$	$\vdots$	$\vdots$	$\vdots$
90	40	8	48	4649.7	6.985	523.09
95	40	8	48	4649.7	7.577	523.09
100	40	8	48	4649.7	8.197	523.09
105	40	8	48	4649.7	8.844	523.09
110	40	8	48	4649.7	9.518	523.09
$\vdots$	$\vdots$	$\vdots$	$\vdots$	$\vdots$	$\vdots$	$\vdots$

Summary

Table 2.6 compares different properties of these cases, such as volume, weight, and factor of safety. Each case experienced the same input load, which was 4649.7 N and achieved the same amount of deflections. Case 4 (L-shaped spring), which had the highest safety of factor in the yield strength, was the most competitive among these cases. In addition, the L-shaped spring had the smallest size and the lightest weight among these cases. Therefore, the L-shaped spring configuration was the wise choice that had a strong structure and a small packaging size for providing the desired compliance.

Table 2.6: Summary of Four Cases

Properties	Case 1	Case 2	Case 3	Case 4
Volume (cm^3)	52.6	34.87	119.39	34.67
Weight (kg)	0.233	0.16	0.529	0.15
Deflection (mm)	9.29	9.29	9.29	9.29
F.S. yield	0.942	0.777	0.846	1.682

2.3 Universal Joint

The use of the universal joints (U-joints) on the actuators was inspired from the applications in THOR. THOR has used a variety of universal joints [2]. The universal joints on THOR were custom made in-house. Fig. 2.6 shows a universal joint configuration of the upper ankle on THOR. The universal joints were attached at the end of each actuator on THOR. The

primary function was to constrain the actuation force to be an axial load acting along the center axis of the ball screw. According to the CAD model of THOR, the size of the universal joints at different positions varied from 35 mm to 44 mm lengthwise. Since these universal joints were only used for actuators rated as 2225 N peak force, a new type of universal joint was required for a single-motor actuator with calculated 4649.7 N peak input force and a dual-motor actuator with calculated 6730 N peak input force. Instead of machining many of the universal joints in-house, off-the-shelf products were used to save machining time.

Figure 2.6: The universal joints on humanoid robots in TREC lab

Load test

A manufacturing company, named Hangzhou Speedway Import & Export Co., Ltd., had a proper size of one type of universal joint. As shown in Fig. 2.7, the universal joint was mainly composed of three parts: caps, needle bearings, and a cross. The size of the U-joint was 16 mm x 38 mm, and the cost was only 5.2 dollars per piece [50]. With the rated torque of 120 Nm, the maximum radial load due to an axial force acting on the needle bearing was calculated to be approximately 6.32 kN. Thus, the total allowable axial load acting at the center of the universal joint was 12.64 kN. This number was much greater than the peak loads of both the single-motor and dual-motor actuators. However, experimental tests were required to prove the strength of this product further.
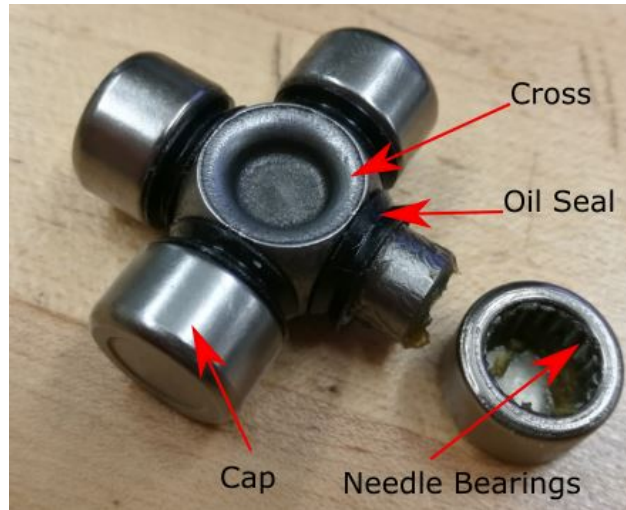
Figure 2.7: Product of the universal joint

Compression load tests were conducted with an Instron machine on universal joints. The universal joint was tested separately with aluminum and steel supports. As shown in Fig. 2.8, a movable crosshead was controlled to move down with a constant speed and continuously apply a compression load at the center of the universal joint until breaking the U-joint. Fig. 2.9 shows a broken universal joint after Instron test.
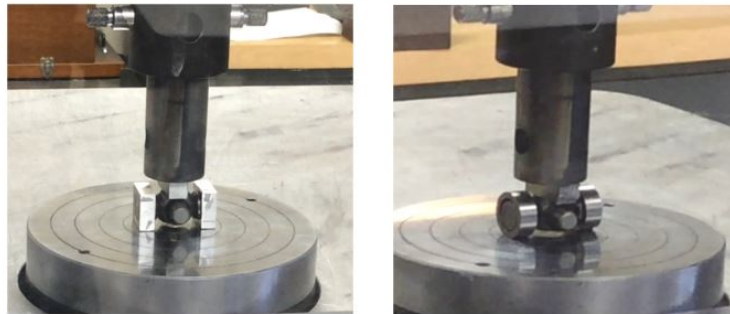
Figure 2.8: Instron Machine Test. Aluminum supports at left and steel supports at right.

Figure 2.9: A failed universal joint.

The load that Instron applied versus the displacement of the crosshead was monitored by the computer. The plots from the computer are shown in Fig. 2.10. The point of F shows where the universal joint failed, and point of M shows where the universal joint started to yield. A summary of compression forces and axial stresses tested for different supports are shown in Table 2.7. As shown in the table, the yield forces required to deform the universal joint for either support were much greater than the peak load of a dual-motor actuator. Therefore, this experimental test proved that the universal joint was strong enough to support the input loads from actuators.
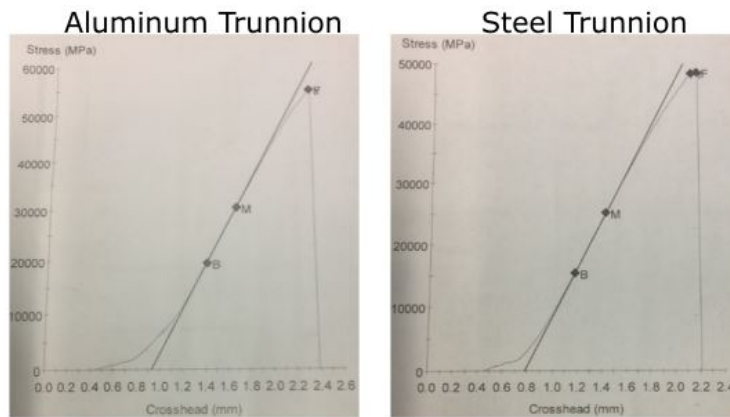
Figure 2.10: Stress vs. crosshead displacement plot (printed from the Instron computer).

Table 2.7: Summary of the test results of the U-joint

	Steel support	Aluminum support
Ultimate Compression (N)	42,529.207	38,101.936
Ultimate Stress (MPa)	54,149.9	48,512.9
Yield Compression (N)	23,963.299	19,192.088
Yield Stress (MPa)	30,511.039	24,436.13

Universal joints at Hip roll and yaw

The hip roll and yaw joints were both powered by a single-motor actuator, separately. At each end of the actuator, the universal joints were supported by yokes to connect the actuator to the frame of the exoskeleton, as shown in Fig. 2.11. The size of yokes that were used to package the universal joints were profoundly affected by the range of operating angles. The operating angles of universal joints can be determined when the range of motions of each hip joint is defined. THOR had a variety of universal joints with a wide range of operating angles [2]. However, the joints of hip exoskeleton had very limited range of motions based on healthy human behaviors. This highly affected the range of angles of universal joints. The other affecting factor is the way actuators are placed. The details of packaging actuators and universal joints will be discussed in Chapter 4.
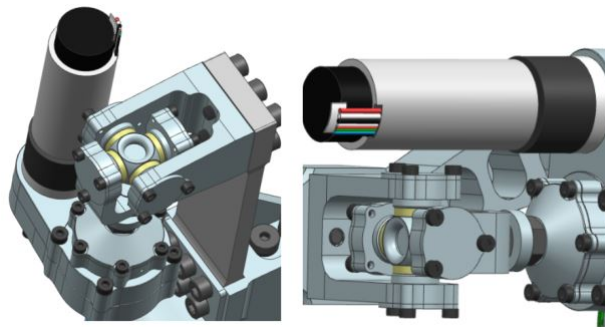
Figure 2.11: Universal joints attached to single-motor actuators in CAD models. From left to right: hip yaw actuator, hip roll actuator.

Chapter 3

Exoskeleton Requirements Development

3.1 Human Data Research

The requirements for OLL-E were to allow for safe and comfortable operation of the exoskeleton. Therefore, the exoskeleton should be anthropomorphic and kinematically similar to a human. In order to achieve an optimal design, a deep understanding of human data was essential.

Human walking has two requisites [51]: One is that there is a periodic gait movement of each foot from one position to the next; The other one is that there are sufficient ground reaction forces during walking to support the body. Any form of bipedal walking is not possible without these two elements [52, 53]. Many papers have discussed the gait cycle of human walking [52, 54, 55, 56, 57]. Human walking can be considered as repeated cyclic patterns of movement. With the assumption of the same successive cycles, a single gait cycle can represent the pattern of human walking [52]. There are two main phases [54]: about 60% of the gait cycle is the stance phase, which means most of the time the foot is in contact with the ground; The left 40% is swing phase, which begins when the toe starts off the ground and stops when the swinging foot contacts the ground.

3.1.1 Range of Joint Motion

OLL-E will have 12 degrees of freedom in total and 6 degrees of freedom on each leg. These DoFs will include: hip with yaw, roll and pitch joints; knee with a pitch joint; ankle with pitch and roll joints. Fig. 3.1 describes different joints rotations of a human lower body. In order to develop the design requirements, understanding the range of these joints rotations was critical. The human joints movements change with age and are more restricted in the

older age group [5]. A. Roaas focused on healthy male subjects that were 30-40 years old based on 210 hips and 180 knees and 192 ankle joints [5]. W.G. Allread had a sample of a 40-year old age group of 100 males and 100 females [6]. B. Appleton shows the range of mobilities in the perspective of stretching exercise [7]. The range of each joint mobility could be estimated by taking the smallest lower and upper bounds of the range in these tables. This was a safe estimation for not harming the operator caused by exceeding the limits of motion. Therefore, a summary of defining the joints motion is shown in the following Table 3.1.
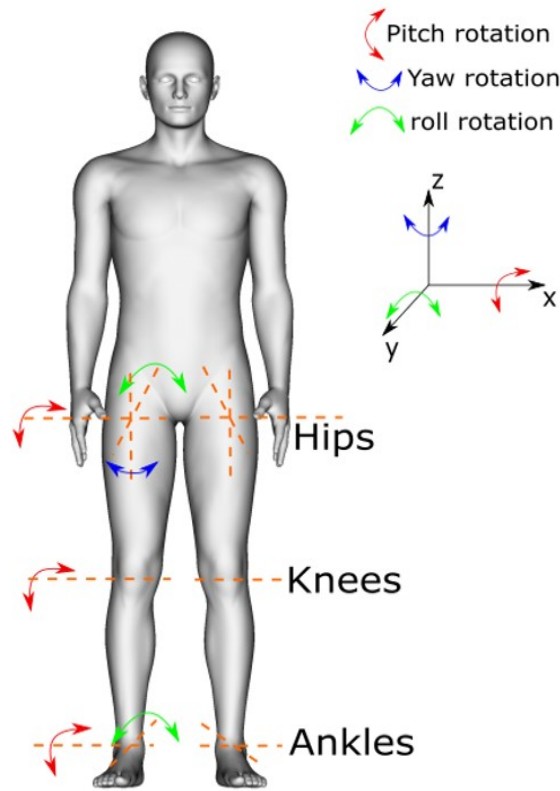
Figure 3.1: Joint motion of human lower body

Table 3.1: Range of motion (deg.) of the hip, knee and ankle joints. Data was summarized from Table [5], [6], and [7]

Joint	Motion	Range
Hip	Extension	0 - 30
	Flexion	90 - 130
	Abduction	15 - 50
	Adduction	15 - 30
	Internal rotation	20 - 40
	External rotation	10 - 45
Knee	Extension	0 - 10
	Flexion	87 - 122
Ankle	Platarflexion	5 - 20
	Dorsiflexion	10 - 45
	Abduction	11 - 20
	Adduction	15 - 30

3.1.2 Body Segments

The study of human body segment parameters (BSP) has been developed by many generations of researchers. One of the earliest studies can be traced back to 1860 by E. Harless, who did the first dissection of cadavers [58, 59]. The pioneering works developed by W.Dempster and C. Clauser have also been commonly cited for studying anthropometrics and biomechanics [60, 58, 61]. W. Dempster did extensive examinations on eight male corpses and determined mass, the center of mass location and moment of inertia values of major body segments [60, 58]. Furthermore, one of the great contributions he did was developing traditional proportional methods for computing body segment parameters for 2-D analyses [62]. The proportional methods included the segment mass and the segment center of gravity. The lengths of body segments were also estimated by W. Dempster and coworkers [60, 63]. The segment lengths were further expressed as a percentage of the body height [64, 9, 8]. Table 3.2 summarizes the lower body segment lengths expressed as a fraction of body height H. The data was gathered and adapted from [9, 65, 8].

Table 3.2: Lower body segment lengths expressed as a fraction of body height H. Data was gathered and organized from [8, 9].

Segment	Formula
Thigh length	$0.245H$
Shin length	$0.246H$
Foot length	$0.152H$
Foot height	$0.039H$
Lower leg length	$0.285H$
Total leg length	$0.530H$

The mass of each body segment could be estimated using proportional methods developed by W. Dempster. The standard calculation of finding segment masses was multiplying the total body mass by the proportion that each segment accounted for the total mass [62]. Note that these ratio values derived by W. Dempster were mainly used for adult males. The sum of all the ratio values must be equal to 1. The equation of calculating segment mass could be directly expressed as following [62]:

$$m_s = P_s m_{total} \tag{3.1}$$

where m_{total} was the total body mass, and P_s was the segment's mass proportion. The summation of proportion values, P_s was expressed as following [62]:

$$\sum_{s=1}^{S} P_s = 1 \tag{3.2}$$

where S was the total number of body segments, and s was the segment number. The lower body segment masses are summarized in the Table 3.3. The mass data was derived from W. Dempster in 1955, and then has been adjusted and compiled by several researchers [60, 63, 62, 9].

21

Table 3.3: Lower body segment masses expressed as a fraction of body weight M. Data was gathered and organized from [9]
.

Segment	Definition	Fraction Formula
Foot	Lateral malleolus/head metatarsal II	$0.0145M$
Shin	Femoral condyles/medial malleolus	$0.0465M$
Thigh	Greater trochanter/femoral condyles	$0.1M$
Lower leg	Femoral condyles/medial malleolus	$0.061M$
Total leg	Greater trachanter/medial malleulus	$0.161M$

Another BSP as a valuable reference for designing the lower body exoskeleton was the center of gravity (CoG). The center of gravity and center of mass (CoM) were in essentially the same locations and were interchangeable in the field of biomechanics [62]. The CoG was the point where the motionless body would stay balanced. In order to quantify the CoG, body segments were assumed to be rigid, and the shape and structure could be ignored [62]. In 1955, W. Dempster developed the formulas that expressed the distance from each endpoint of a segment to that segment's CoG as a fraction of the segment's length [60, 62]. The proportion formulas are shown below [62]:

$$R_{proximal} = \frac{r_{proximal}}{L} \tag{3.3}$$

$$R_{distal} = \frac{r_{distal}}{L} \tag{3.4}$$

where $r_{proximal}$ and r_{distal} were the distances from proximal and distal ends to the segment's CoG, respectively. L was the length of the segment. The percentages of the CoG distance from either the distal or the proximal end have been organized and compiled by several investigators, as shown in Table 3.4 [9]. Note that the segments definitions in Table 3.4 were the same as Table 3.3.

Table 3.4: Lower body segment distance proprotions of CoG in relation to segment endpoints. Data gathered and organized from [9].

Segment	$r_{proximal}/L$	r_{distal}/L
Foot	0.50	0.5
Shin	0.433	0.567
Thigh	0.433	0.567
Lower leg	0.606	0.394
Total leg	0.447	0.553

Another important parameter was the width between hip joints, known as pelvic width. In order to mimic the hip roll motion, the design of hip roll joints should be close to the location of human hip joints. Knowing the pelvic width could help define the primary size of the hip exoskeleton. There were a few papers related to the pelvic width [11, 10, 12]. The pelvic width was the distance between the centers of the right and left femoral heads [12]. The other general definition of the pelvic width was defined as the distance between the two anterosuperior iliac spines [66]. S. Cho collected data from 98 Korean adults (47 females and 51 males), and the pelvic width was determined by the distance between the bilateral pelvic markers [10]. The subjects from G. K. Seidel's experiments were 65 adult cadavers (35 females and 30 males), and measurements were taken from bony landmarks of de-fleshed pelves [11]. G. Daysal used radiographic parameters from 118 patients who underwent supine abdominal radiography to define the pelvic widths [12]. The pelvic widths determined from these results had a wide variance, as shown in Table 3.5. The variation might be caused by factors of experimental subjects and environments. In order to better estimate the pelvic width, a wearable prototype can be helpful. The prototype was built and discussed in the next section.

Table 3.5: Pelvic width (cm) of different experimental results. Data was collected and organized from [10, 11, 12].

Subjects	Mean (SD)
98 Korean adults	26.4 (2.3)
65 adult cadavers	23.8 (1.7)
118 adult patients	20.7 (1.0)

3.2 Lower-Body Exoskeleton Prototype

In order to test the functionalities of all joints' configurations, a full 12-DoF lower body exoskeleton prototype was developed. The goal was to make the whole architecture kinematically similar to a human's. The natural design of all the DoF axes should pass through the corresponding human joints. The materials used for building the structure were mainly 8020 aluminum t-slotted extrusions.

3-DoF design at the hip

The design of the 6-DoF at the hip was inspired from BLEEX, as shown in Fig. 3.2 [3]. The objective of the BLEEX exoskeleton was to assist the operator to carry heavy payloads over

rough terrain or up staircases. BLEEX could not let all three axes of rotation pass through the human hip joint because this would result in singularities at some hip postures. Only hip pitch and roll joints were actuated, and the yaw joint was passive. For hip yaw joint, BLEEX changed the initial design by moving the rotation axis above the pitch joint (labeled "Hip yaw (option 2)" in Fig. 3.2) to the back of the center of the frame (labeled in "Hip yaw (option 1)" in Fig. 3.2). The reason was that the heavy payloads on the backpack would create a large moment about the "Hip yaw (option 2)".
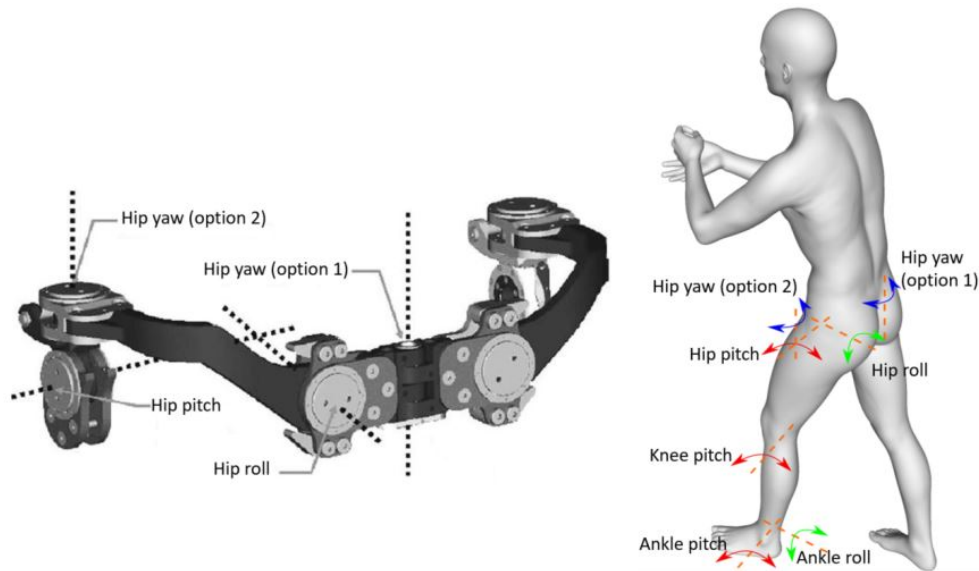
Figure 3.2: BLEEX 6-DoF design at the hip (left picture) [3] and a human model with options of placing hip yaw joint (right picture).

As for OLL-E, the hip yaw was powered by a linear actuator. As shown in the right picture of Fig. 3.2, the placement of hip yaw joint in option 2 was very close to the hip pitch joint. This placement let both the hip pitch and hip yaw joint set on the side of the human leg. Therefore, this configuration of the hip yaw joint could closely mimic the motion of the human leg. The other problem for placing the hip yaw joint at the back of the frame was a lack of space for packaging a linear actuator when hip roll actuators come in play. In the end, the first prototype design of the hip pitch and yaw joints was shown in Fig. 3.3. The right picture shows the hip pitch and yaw joints built by 8020 aluminum one-inch square extrusions with pivots. The left picture shows the CAD model based on dimensions from the prototype.
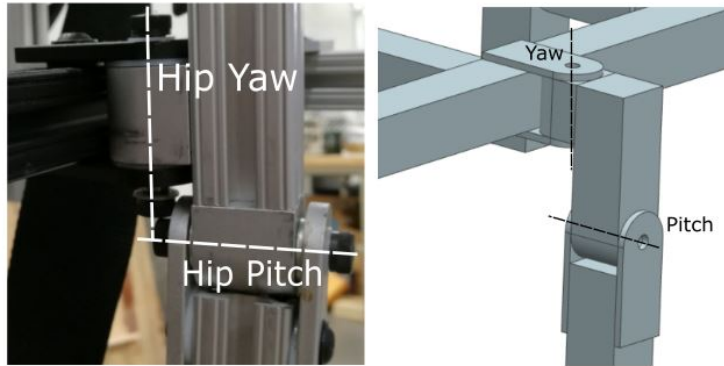
Figure 3.3: Prototype design of hip pitch and yaw joints.

The placement of the roll joint was at the back of the human hip, so the rotation axis passed through the hip ball and socket joint. However, the difficulty was to match the exoskeleton's roll joints closely with the operator's. As mentioned in Section 3.1, the pelvic width of human defined the distance between the center to center of the hip joints. At first, the joints distance was estimated by measuring the focal distance of the hip breadth. After several people experimentally wore the prototype, the initial measurement of the joints distance worked well for people's roll joints movement. Fig. 3.4 shows the prototype of the hip roll joint and its simplified dimensioned CAD. The estimated width of the roll joints was 203.2 mm, which was close to the result from [12]. Thus, 207 mm of the pelvic width in [12] could be a good reference for the hip roll joint design.
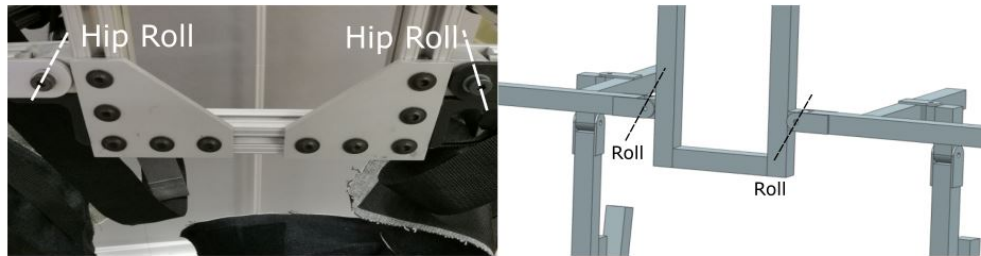
Figure 3.4: Prototype design of the hip roll joints.

Knee and ankle joints

The knee joint of the exoskeleton only had one degree of freedom, which had a large range of flexion motion. The joint location should match with the operator's knee joint. The prototype of the knee joint and its CAD are shown in Fig. 3.5. The length of the upper leg and lower leg were adjustable by moving the locking bracket and knee joint position, separately. As for the design of the ankle, it had two DoF (pitch and roll). Similarly to

the design of hip joints, the axes of ankle pitch and yaw should pass through the operator's ankle joint. The foot plate had a passive movable hindfoot joint used for toe-off. Fig. 3.6 shows the prototype design of the ankle joints and the foot plate.
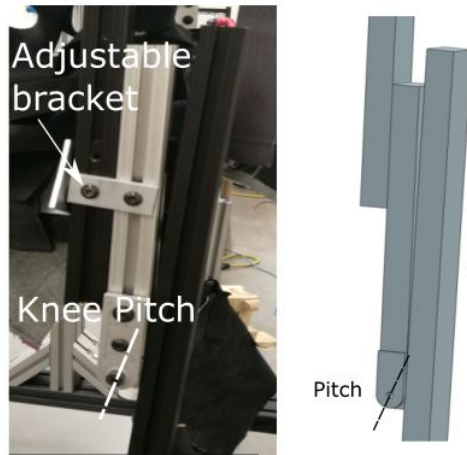
Figure 3.5: Prototype design of the knee joint.
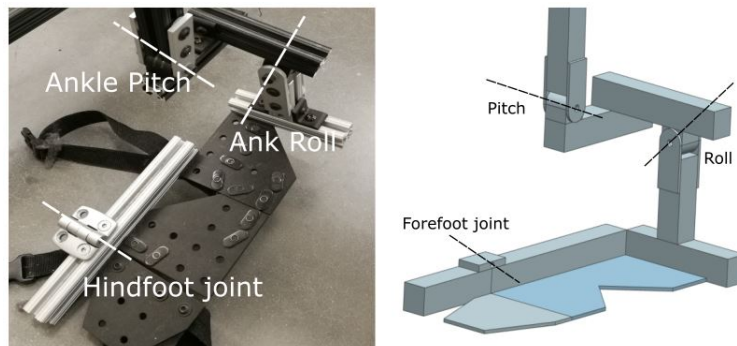
Figure 3.6: Prototype design of the ankle and the foot plate.

Prototype test

The wearable prototype of 12-DoF lower-body exoskeleton was built with the adjustability feature for the hip breadth and the length of the upper and lower leg so that this prototype could be worn by different sizes of people. Fig. 3.7 shows the full size of the exoskeleton prototype and the CAD model. The prototype was hanging by mounting on a gantry. As shown in Fig. 3.7, people could wear it through the waist and shoulder belts and the custom-made harnessing at the upper and lower legs and foot plates. The waist and shoulder belts were bought off the shelf. The upper and lower leg harnessing was made by sewing multiple

Velcro strips together with a cloth. The foot harnessing was made by straps with buckles on forefoot and midfoot.

Figure 3.7: Prototype of 12-DoF lower-body exoskeleton.

Fig. 3.8 shows a full gait cycle by wearing the exoskeleton prototype. The operator was doing a normal walking in a straight line for about 8 seconds. The walking was video recorded with a frame rate 31.5 Hz. In addition, a variety of postures were tested when wearing the prototype as well. Those poses were made by the operator self-balancing without supports, as shown in Fig. 3.9. In the end, the operator could feasibly walk around corners and in circles. The results of postures and walking tests showed that there were no singularities at this configuration of 12 DoF. Therefore, this prototype provided an important reference for future designs of joint configurations.
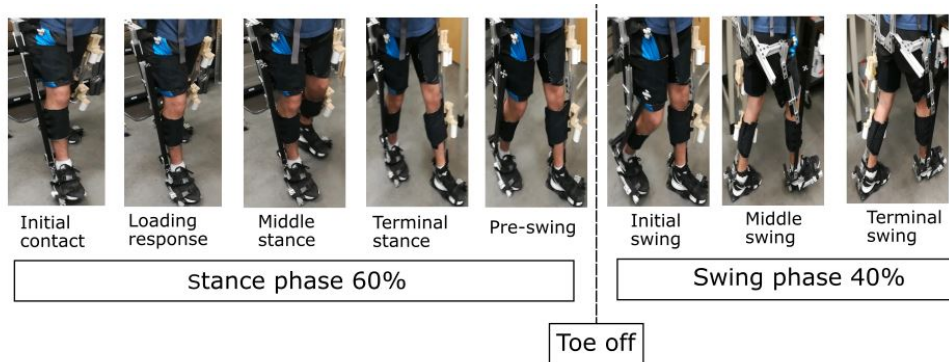
Figure 3.8: 100% gait cycle walking with the exoskeleton prototype.
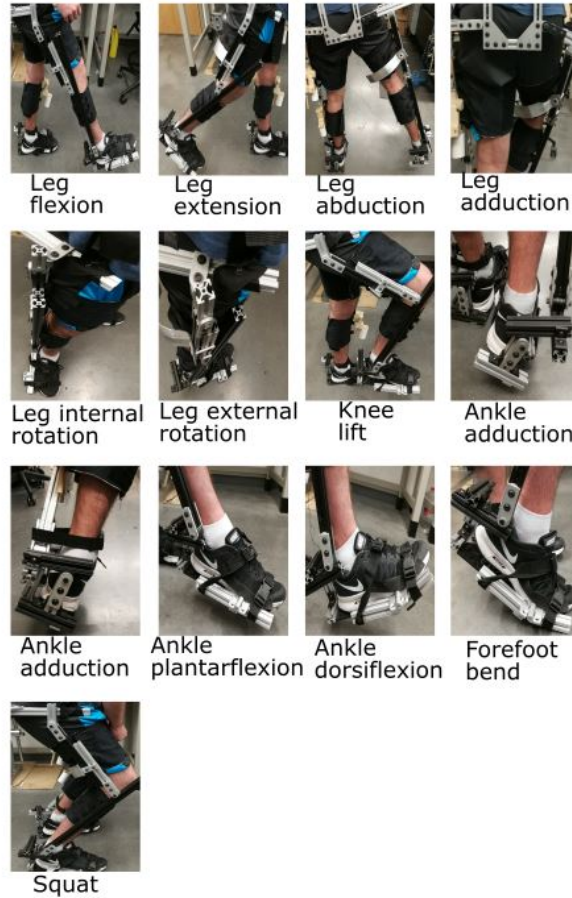
Figure 3.9: Postures test with the exoskeleton prototype.

3.3 Theoretical Analysis

The mechanical design of OLL-E was from scratch. The mechanical requirements for each degree of freedom were initially unknown. Defining the requirements of each DoF would be the priority before approaching the design of the frame structures. Therefore, some assumptions and limitations were needed, in order to proceed the analysis of requirements.

One of the critical assumptions was estimating the properties of the whole exoskeleton. This assumption was made based on ESCHER, which was a humanoid robot built in TREC lab at Virginia Tech [1]. It had total a weight of 77.5 kg and 1.78 m of height in standing. The motions of ESCHER lower body was kinematically anthropomorphic, so it was reasonable to assume that the lower-body exoskeleton could have similar properties. Table 3.6 lists ESCHER properties that were used in further analysis.

Table 3.6: ESCHER's mechanical properties. Data was gained from ESCHER CAD model.

Lower-body segments	$r_{proximal}$ (m)	Mass of segments (kg)
Thigh	0.207	7.1064
Lower leg	0.165	6.6896
Foot	0.0436	1.798
Total leg	0.2873	13.796

Body segments assumptions

The total weight of the operator and the exoskeleton were limited to 150 kg. Thus, the operator weight could be inferred as 75 kg given 75 kg of the exoskeleton. The height of the operator was limited to 1.85 m. Based on ESCHER's mass distribution, the hip and upper body mass budget was 47.4 kg. By using the W. Dempster's proportional technique (Section 3.1), the properties of the lower body segments could be estimated, as shown in Table 3.7.

Table 3.7: Segments properties of a 1.85 m, 75 kg human operator.

Segments	Length (m)	Mass (kg)	$r_{proximal}$ (m)
Thigh	0.45325	7.5	0.19625
Lower leg	0.52725	4.575	0.31951
Foot	0.2812	1.0875	0.1406
Whole leg	0.9805	12.075	0.43828

The positions of CoGs of combining exoskeleton and human legs needed to be calculated to help analyze the torque loads at each joint. The masses and CoGs in Table. 3.6 and 3.7 could be used to determine the CoG positions of whole leg, lower leg and foot, and foot, respectively. The formula used for determining CoG relative locations was shown as follows:

$$x = \frac{\sum_{i=1}^{n} m_i x_i}{M} \tag{3.5}$$

where m_i was the mass of the ith section, x_i was the distance from CoG to the the same proximal of ith section, and M was the total mass of sections. For example, the equation for finding the distance of total leg's CoG to the proximal end was calculated as:

$$x_{leg} = \frac{m_{Eleg}x_{Eleg} + m_{Hleg}x_{Hleg}}{m_{Eleg} + m_{Hleg}} \tag{3.6}$$

where m_{Eleg} was the mass of the lower body of the exoskeleton, x_{Eleg} was the relative distance of CoG to the proximal end, and m_{Hleg} was the mass of the whole leg of the operator. The properties of combining the operator and the exoskeleton lower bodies were shown in Table. 3.8.

Table 3.8: Properties of combining the operator and the exoskeleton

Segments	$r_{proximal}$ (m)	Total mass (kg)
Whole leg	0.35779	25.871
Lower leg	0.23622	11.2646
Whole foot	0.08015	2.8855

Joint loads analysis

The purpose of finding loads at each joint was to guide the selections of bearings and structural designs. The methods of estimating loads at each DoF were complicated and were not trivial, especially when considering dynamic motions. The circumstances of dynamics are hard to be simulated because human behaviors are random and hard to be predictable. Instead, using static situations to estimate loads could be much simpler. However, static estimations should be conservative, in order to better take care of dynamic conditions to some extent.

There were two extreme cases of static postures for determining maximum moment load at each joint: one was leg abduction, and the other one was leg flexion. These postures were both assumed to have 90° rotating away from standing position because this angel could give the longest moment arm. The moments were determined from a 3g force of the total weight of the operator leg and the exoskeleton leg. Another extreme situation was that the operator stood on one leg, and the whole body weight of the system acted on this one leg at a 3g load. In this situation, the maximum load force acted on each hip joint was 4500 N. Although leg abduction might not have a 90° of motion in real design criteria, this assumption was conservative and convenient for calculating loads given the unknown range of motions. The actual loads on joints were adjusted after the range of movements were finalized. The addition of a 3g load was a conservative assumption, which was used to accommodate to dynamic situations.

The load analysis was conducted based on the body segments data in Table. 3.8 and the prototype CAD model made in Section 3.2. Use hip roll joint calculations as an example to show the process of finding the moment loads at each joint. Fig. 3.10 shows the extreme cases of the leg abduction and flexion at 90°, respectively. The CoG of the whole leg of the human and exoskeleton was at a distance of D_P from the pitch joint. In order to find the moment reaction at roll joint, the distances (D_x, D_y, and D_z) in three axes directions were

used for calculations.
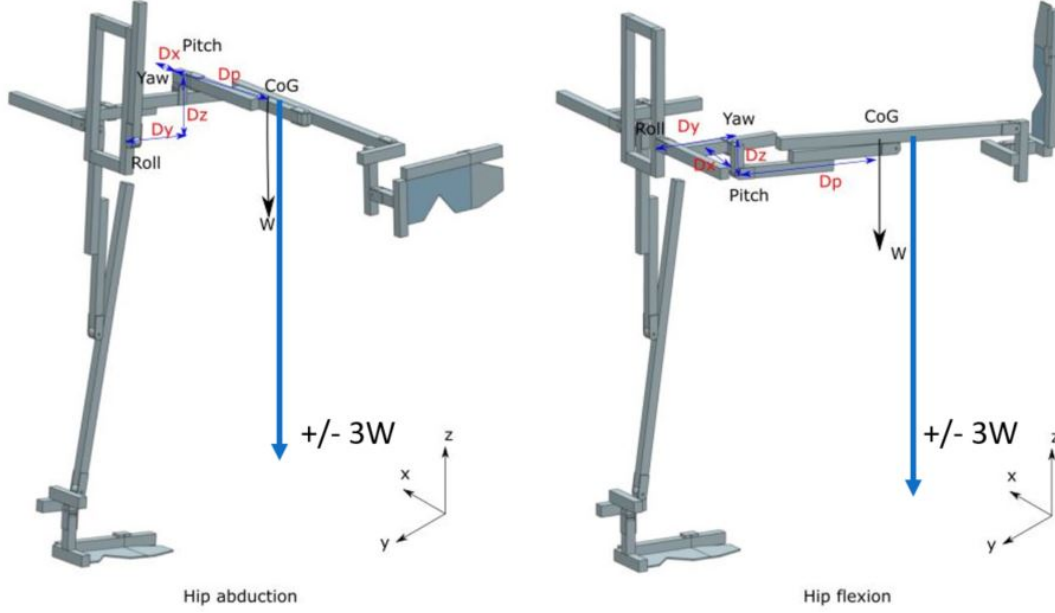
Figure 3.10: Extreme cases of leg abduction and flexion postures.

The moment reactions for hip abduction and flexion at the roll joint in x, y, and z axes directions could be calculated, respectively, as follows:

$$M_x^{Abd} = F_z D_y + F_y D_z \tag{3.7}$$

$$M_y^{Abd} = F_z(D_x + D_p) + F_x D_z \tag{3.8}$$

$$M_z^{Abd} = F_x D_y + F_y D_x \tag{3.9}$$

$$M_x^{Flex} = F_z(D_y + D_p) + F_y D_z \tag{3.10}$$

$$M_y^{Flex} = F_z D_x + F_x D_z \tag{3.11}$$

$$M_z^{Flex} = F_x D_y + F_y D_x \tag{3.12}$$

Assuming that there were no other external loads in x-axis and y-axis, and $F_z = W$ was only caused by the weight of the whole leg in the z-axis. Therefore, by using the equations above, the results of reacting moments and forces at each joint were summarized in Table 3.9.

31

Table 3.9: Extreme cases of two static postures results of moments and reaction forces

DoF	Axis direction	Extreme leg abduction		Extreme leg flexion	
		3g*Force (N)	3g*Moment (Nm)	3g*Force (N)	3g*Moment (Nm)
	x	0	95.036	0	367.459
Hip roll	y	0	311.101	0	118.014
	z	761.384	0	761.384	0
	x	0	0	0	90.808
Hip pitch	y	0	272.423	0	0
	z	761.384	0	761.384	0
	x	0	0	0	272.423
Hip yaw	y	0	272.423	0	0
	z	761.384	0	761.384	0
	x	0	0	0	85.872
Knee pitch	y	0	85.872	0	0
	z	363.522	0	363.522	0
	x	0	0	0	6.807
Ankle pitch	y	0	6.807	0	0
	z	84.920	0	84.920	0
	x	0	2.242	0	6.807
Ankle roll	y	0	6.807	0	4.059
	z	84.920	0	84.920	0

3.4 Summary of Joint Requirements

In this chapter, the results from the research of human data are discussed, and these properties helped make assumptions and constrain requirements of the exoskeleton. The range of each DoF motion is summarized in Table 3.1. The properties of lower-body segments and the experiment results of the exoskeleton prototype provided valuable references for the mechanical designs on each joint. Overall, the capabilities of the OLL-E were based on total weight of 150 kg of the operator and the exoskeleton. In Table 3.10, the maximum loads at each hip joint are summarized. Table 3.11 shows the required peak torque and velocity results that were developed by my co-worker, John Kendrick.

Table 3.10: Maximum loads at each joint.

DoF	Max. moment (Nm)	Max. load force (kN)
Hip roll	311.1	4.5
Hip pitch	272.4	4.5
Hip yaw	272.4	4.5

Table 3.11: Peak torques and velocities at each joint developed by John Kendrick.

DoF	Peak torque (Nm)	Peak velocity (rad/s)
Hip roll	208.5	0.8
Hip pitch	200	5.1
Hip yaw	101.9	1.8
Knee pitch	394.7	7.2
Ankle pitch	197.2	5.1
Ankle roll	89.5	5.9

Chapter 4

Hip Exoskeleton Design

4.1 Joint Configuration Synthesis

In order to start the design of the hip exoskeleton, figuring out relative locations of each joint and understanding reaction loads were critical. The joint requirements and a built-in human model in software NX 11 helped to guide the design criteria of joints. Fig. 4.1 shows the initial scheme of hip 6-DoF locations based on the built-in human model. The hip breadth of this human model was set to be 360 mm, which accounted for about 50th percentile of aged 19-65 US people [67].
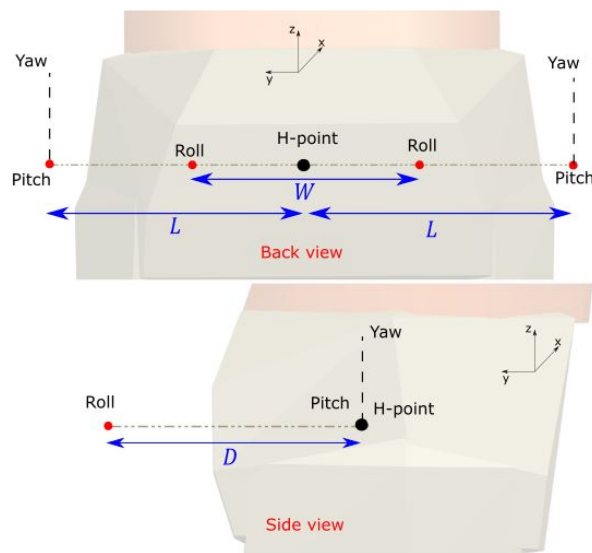
Figure 4.1: Initial scheme of 6-DoF locations at the hip.

The H-point that the human model provided was the relative location of the hip and the pivot point of the upper leg. Therefore, this point could be used for aligning joint axes. The idea of this layout of joints in Fig. 4.1 was inheriting the prototype design from Chapter 3. The pitch joint axis passed through the H-point, and the yaw joint axis was aligned with the center of the pitch joint. Although the human ball and socket hip joint was not shown in this human model, its position could be estimated by finding out the intersection between roll and pitch joint axes. Chapter 3 determined the distance between roll joints, $W = 207$ mm. These two roll joints were symmetrical about the H-point, as shown in Fig. 4.1. The distance of D and L were estimated based on the size of bearing housings and the clearances between the exoskeleton and human body.

Unfortunately, this initial estimation of scheme layout was not working well as the design proceeded. Some issues developed: first of all, the location of roll joints was too low in the z-axis direction, and this caused the structure to interfere with the human body; Secondly, the length, L was smaller than expected when wearing the 3D printed assembly. This issue might be caused by not considering the thickness of the operator's clothes; Finally, the length, D of the structure was not long enough to pass the operator's pitch joint when wearing 3D printed parts. The reason for this was that the depth of a person's hip in the x-axis direction had size differences for different persons. Therefore, the original scheme layout was modified with changing the locations of joints. However, the pitch joint still stayed in the original x-y plane where the H-point was at. The roll joints were moved up 30 mm higher than the pitch joint. In fact, this adjusted height was matched with the roll-pitch distance in the 12-DoF wearable prototype. Fig. 4.2 displays the modified layout of joint locations. Table 4.1 shows comparisons after changes. These changes suggest that adjustability features were necessary to be considered in the future design.
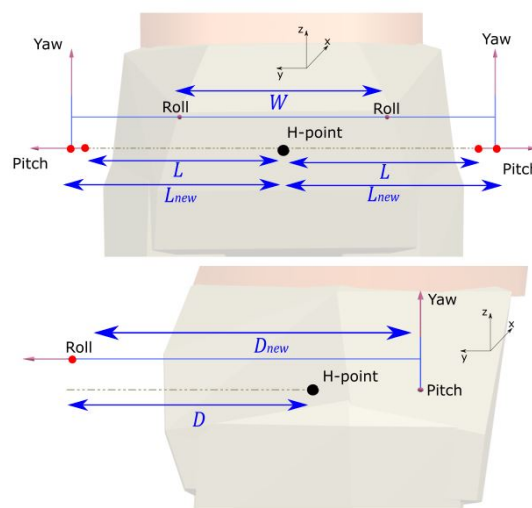
Figure 4.2: Modified scheme of 6-DoF locations at the hip. Dashed line is the original layout, and blue line is the modified layout.

Table 4.1: Comparisons of joint location layout.

D (mm)	D_{new} (mm)	L (mm)	L_{new} (mm)
197.8	211.3	174.5	258.7

4.1.1 Force analysis

Force analysis was the critical step before proceeding the design of the structure. In this section, reaction loads were developed at each joint based on the layout in Fig 4.2. The loads calculated in Table. 3.9 could be helpful, but these loads were conservative calculations based on 90° range of motions for all joints. In actual design criteria, the range of movements of each joint would not be 90° exactly. Therefore, having general equations for each joint could be useful for future joints designs. Fig. 4.3 shows the free body diagrams of each joint for leg flexion and abduction, respectively. The maximum reaction force at each joint was equal to the gravity of the whole leg, W. For example, the reacting moment and torsion for leg flexion at the roll joint were calculated as follows:

$$M_{r1} = -W l_1 \tag{4.1}$$

$$T_1 = W \sin(\theta_1)(l_2 + l_4) \tag{4.2}$$

while the reacting moments for leg abduction were calculated as follows:

$$M_{r3} = -W \sin(\theta_2)(l_1 + l_3 + l_4) \tag{4.3}$$

$$T_4 = W \sin(\theta_2) l_2 \tag{4.4}$$

where M_{r1} and M_{r2} were resisting moments for rotations. The torsions of T_1 and T_2 affected the robust designs of structures. Other joint reacting moments could be calculated similarly. Note that these moments were using a 3g factor of loads. A summary of maximum loads on hip joints with defined range of motions is shown in Table 4.2.
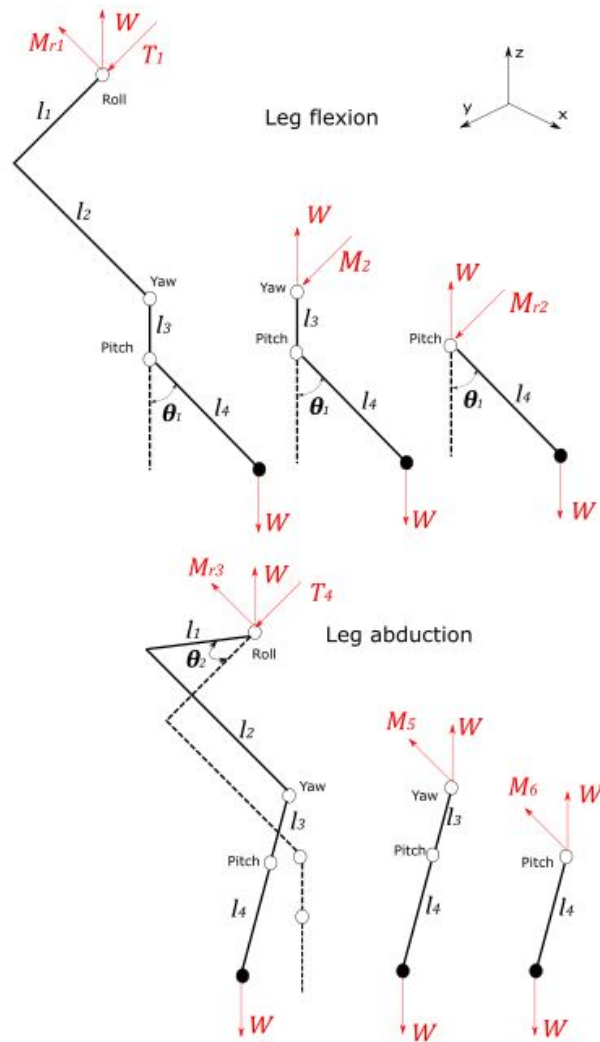
Figure 4.3: Free body diagrams of each joint at two positions, respectively.

Table 4.2: A summary of maximum loads at hip joints.

Joint	Max. moment (Nm)	Max. load force (N)
Roll	462.18	4500
Yaw	268.20	4500
Pitch	272.02	4500

4.2 Joint Design

This section focuses on the design of each joint at the hip, including bearing selection and installation, hard stop design and installation, and the limit switch and encoder packagings. According to the requirements developed in Chapter 3, the range of motions (RoMs) for each joint of the hip exoskeleton are summarized in Table 4.3 below. The neutral position was standing straight.

Table 4.3: Summary of RoMs for each joint at the hip exoskeleton.

Joint	RoM (deg.)
Hip roll	+30°/-30°
Hip yaw	+40°/-30°
Hip pitch	+100°/-30°

The major material chose for designing the hip exoskeleton was Aluminum 7075 T6. This type of metal has light weight and high strength and is famous for using in aircraft and terrain vehicles. As for the shaft at each joint, the material was StressProof® 1144 carbon steel, which is stress relieved by cold drawing and has high tensile strength. The rest of other components will be made of common Aluminum 6061 T6. Table 4.4 lists properties of these materials. Fig. 4.4 is the overview of the hip exoskeleton assembly. The hip exoskeleton was mainly composed of five assemblies: the hip roll joint assembly highlighted in pink color, hip yaw joint assembly highlighted in yellow color, hip pitch joint assembly highlighted in green color, actuators highlighted in orange, and the backpack assembly highlighted in purple. These assemblies will be discussed in details in later sections.

Table 4.4: Properties of major materials used in hip exoskeleton. Data was collected from [13].

Property	Al 6061 T6	Al 7075 T6	StressProof® 1144
Density (g/cc)	2.7	2.81	7.85
Yield strength (MPa)	276	503	689
Elastic modulus (GPa)	68.9	71.7	200
Poisson's ratio	0.33	0.33	0.29
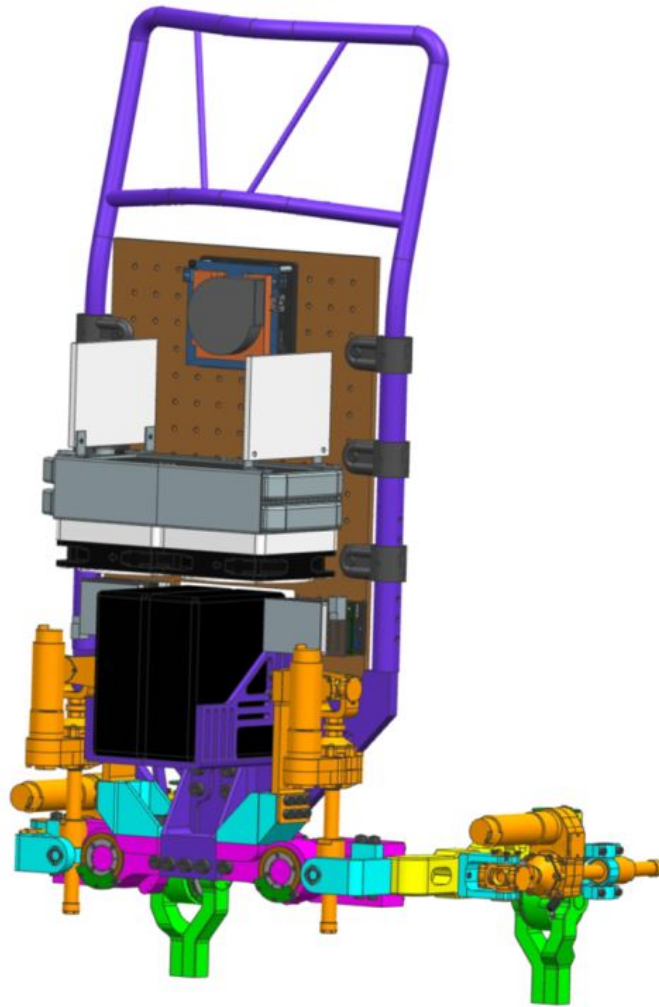
Figure 4.4: Overview of the hip exoskeleton assembly with colored different sub-assemblies.

4.2.1 Bearing selection

Following the static force analysis described in Section 3.3 and 4.1, the radial and axial loads on bearings were calculated to determine the type of bearing. The fact was that force reacting on bearings was tremendous, particularly for radial loads. Therefore, the selected bearing should be able to handle the heavy loads in both radial and axial directions. One of the best choices was the tapered roller bearing.

A tapered roller bearing is composed of an outer ring, an inner ring, and tapered rollers. The advantage of a tapered roller bearing can take radial and axial loads simultaneously. A

single-row bearing can only take one direction of axial load. Thus, in order to take account for both directions of axial loads, a pair of sing-row bearings was used. The arrangement of the pair of bearings in the housing was assigned back-to-back because this way let the effective load center of two bearings point outward, which gave a long support base to distribute loads more evenly. Fig. 4.5 illustrates the free body diagram of the back-to-back arrangement. Table 4.5 lists the tapered roller bearing used in each joint, including the maximum force acting on each joint, and the static and dynamic load ratings of each bearing. Note that the maximum applied force was at a 3g load. The maximum applied load on each bearing was below both the static and dynamic load ratings. Maintaining the peak force within the static rating ensured the bearings will not be damaged. Also, the applied peak load was less than the dynamic load rating allowing the bearings to endure many cycles of operations.

F_r: external radial load
F_a: external axial load
a: effective load center
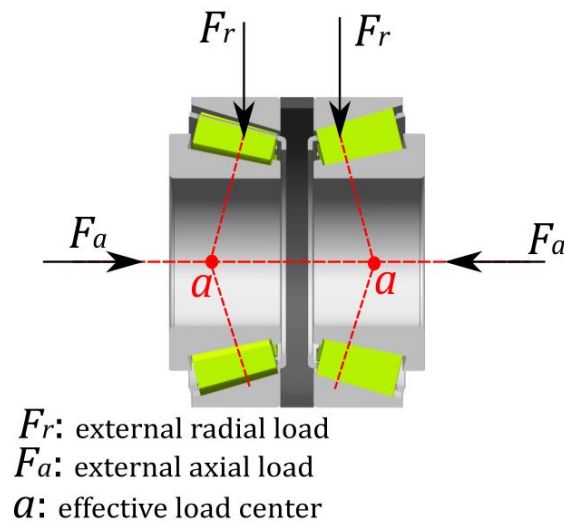
Figure 4.5: Free body diagram of back-to-back arrangement of tapered roller bearings.

Table 4.5: Tapered roller bearing used on each joint at the hip exoskeleton.

Joint	IDxODxW (mm)	Max. load (kN)	Static load rating (kN)	Dynamic load rating (kN)
Roll	20x42x15	18.86	27	24.2
Yaw	17x40x12	14.29	18.6	19
Pitch	17x40x12	14.09	18.6	19

4.2.2 Hip roll

An exploded view of the hip roll components is shown in Fig. 4.6 with number callouts for each piece. Table 4.6 briefly describes their names and functions. The major components of this assembly are the hip roll housing and the hip roll arm. The details of these parts will be discussed in this section.
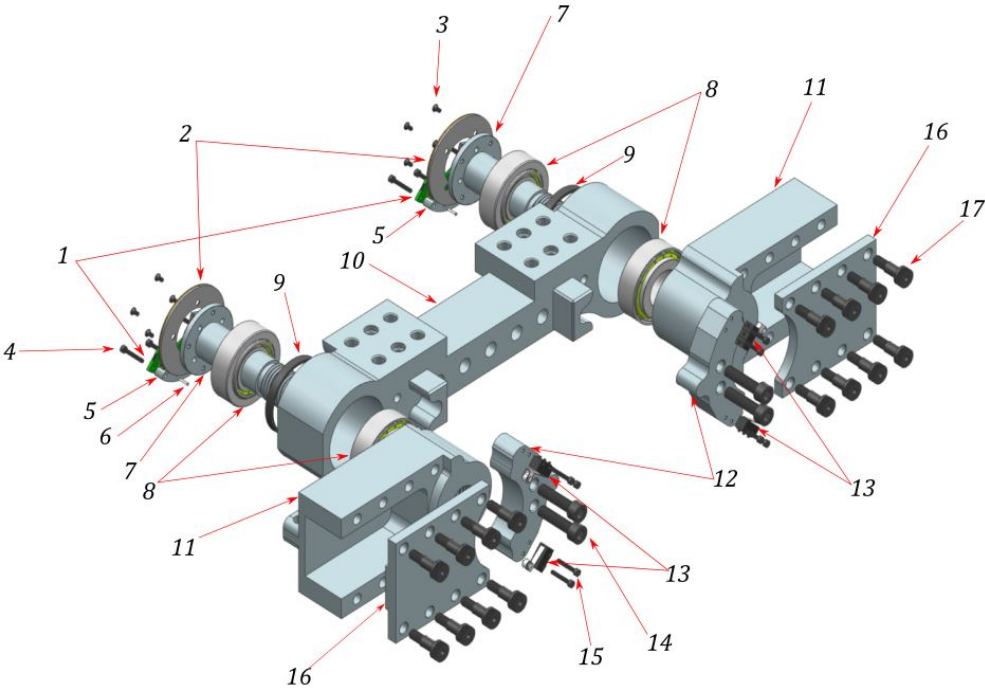
Figure 4.6: Exploded view of hip roll assembly with labeled components.

Table 4.6: Summary of labeled components in hip roll assembly

Label	Name	Functions
1 and 2	AksIM^{TM} absolute ring encoder	16 bits per revolution
3	Flathead M2.5 bolt	Mounts the encoder on the top of the shaft
4	Socket head M3 bolt	Mounts the encoder readhead
5	Readhead Standoff	Keeps the readhead required distance from the encoder
6	Dowel pin	Provides alignment for the standoff
7	Custom shaft bolt	Provides output transmission
8	Paired tapered roller bearings	Distribute radial and axial loads
9	Bearing spacer	Provides supporting base for bearings
10	Hip roll housing	As a housing and a mounting base for other features
11	Hip roll arm	Transmits the motion of the hip roll
12	Hard stops	Stop the movement of the roll joint at safe limits
13	Limit switches	Shuts off the power before hitting the hard stop
14	Socket head M6 bolt	Mounts hard stops
15	Socket head M2 bolt	Mounts limit switches
16	Arm clamp	Clamps the yaw housing frame into the U-channel
17	M5 shoulder screw	Mounts the arm clamp in position
	Internal snap ring (not shown)	Retains the bearings from the other side

The tapered roller bearings were installed in back-to-back arrangement with a 4.5 mm spacer in between. This arrangement determined the size of the housing. The distance between two roll joint housings from center to center was determined according to Fig. 4.2. A custom shaft bolt was used to clamp the pair of bearings together with the hip roll arm. Fig. 4.7 depicts the dimensions of the custom shaft bolt. There was a relief cut between the shaft and the thread parts used for threading tool runout. The thread size was M20 by 2 mm pitch. As shown in Fig. 4.7, one of the hole patterns on the shaft was used to mount the encoder ring. The other hole pattern, which appeared on every shaft of each joint, was used for tightening the shaft by a custom-made spanner wrench. Torquing on the custom bolt can give a preload applied on bearings to eliminate the backlash. Fig. 4.8 displays the view-cut section of the inside of the housing. The hip roll arm had a flange feature that was against the inner cone face of one side of the bearing. The shaft passed through a shoulder pocket, which was used to align the shaft. There was a small clearance used for tightening between the end of shaft part and the bottom of shoulder pocket. The internal snap ring kept the bearings from moving out. The snap ring was made of 302 stainless steel and manufactured by SMALLEY, which had a yield strength of 15,147 N [68].
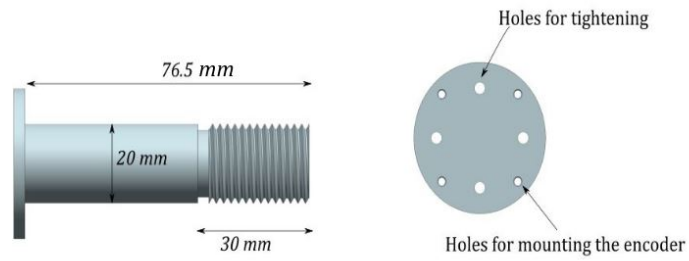
Figure 4.7: Views of the custom shaft bolt for hip roll.
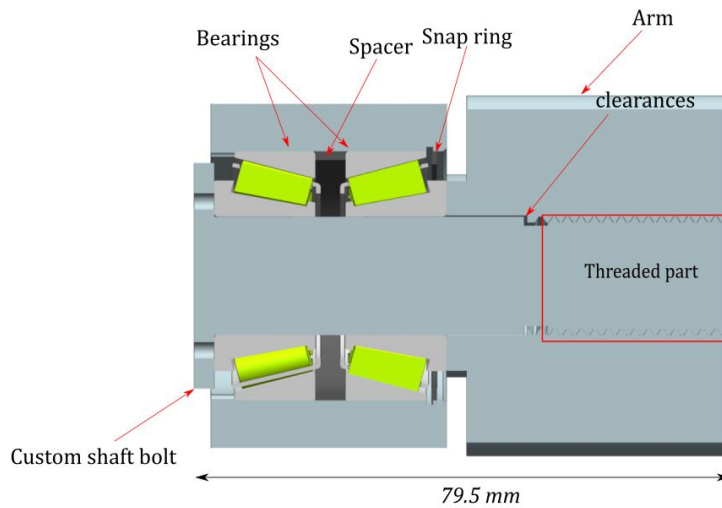
Figure 4.8: View-cut section of the hip roll joint.

As for the hip roll housing, the design changed from simple to complex. At first, it had the function of providing the housing for the roll joint bearings. However, as the design proceeded, this component became a significant transition for connecting and mounting other components. Fig. 4.9 illustrates some features that the hip roll housing had.
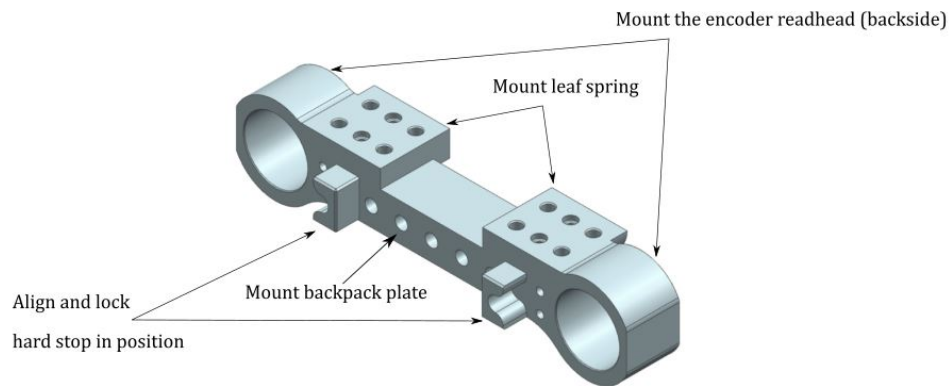
Figure 4.9: Isometric view of the hip roll housing with features.

Fig. 4.10 shows major functions that the hip roll arm has. Besides the pocket that allowed the custom bolt to pass through, this arm part also had two other features. One was providing a bearing pocket to support a ball screw trunnion with a lug, as shown in the backside view. The other feature was the U-channel that yaw housing frame could fit inside, as shown in the front view. In the meantime, this U-channel allowed the frame to move in and out for adjustability. This feature will be described more in details in the next section.
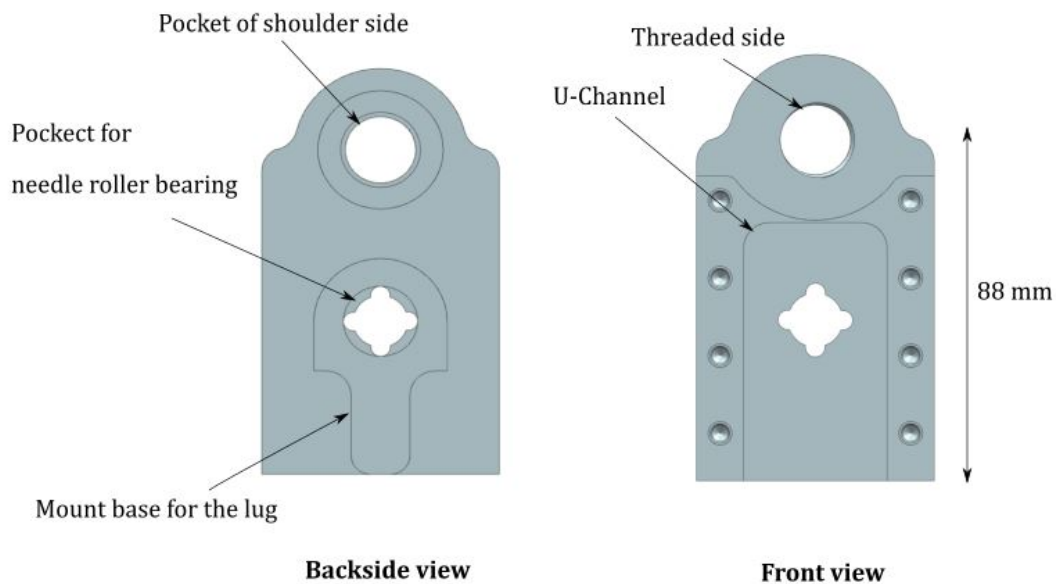
Figure 4.10: Backside and front views of the hip roll arm.

The encoder used for each joint was a non-contact absolute rotary encoder. Compared to a shaft encoder, this non-contact type did not have a misalignment issue, and it had more resistance to wear-out and required easier installation. The encoder module had two components: a readhead board and an axially magnetized ring. For the hip roll joint, the ring was mounted on the movable shaft, and the readhead was mounted on the stationary roll housing, as shown in Fig. 4.11.
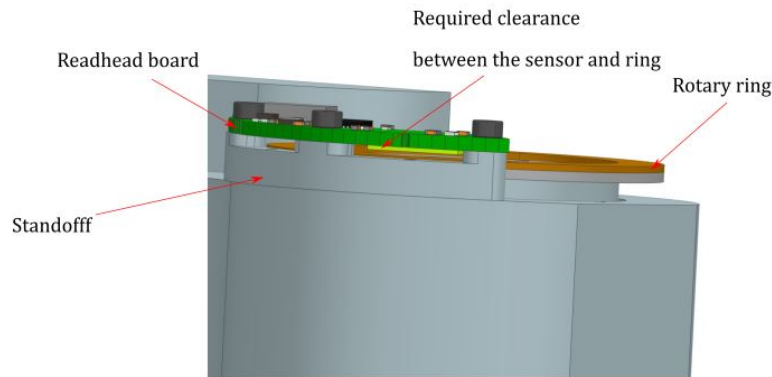
Figure 4.11: Side view of the encoder mounting.

Finally, the design of the hard stop and the position of the limit switches were significant because they could prevent the exoskeleton from harming the operator. The hard stop was made of stainless steel and placed in the path of the arm rotation. As shown in Fig. 4.12, the arm was pushing the limit switches to the off position at $\pm 28°$, and was entirely stopped at $\pm 30°$ when contacting with the hard stop. There was an impact load when the arm hitting the hard stop. The peak angular velocity of the arm was 1.26 rad/s calculated by John Kendrick. Given R in the figure, the linear velocity was about 0.055 m/s. Using the assumed the total leg weight, the impact load acting the hard stop was about 5.2 Ns using 3g factor. This amount of load was relatively small.
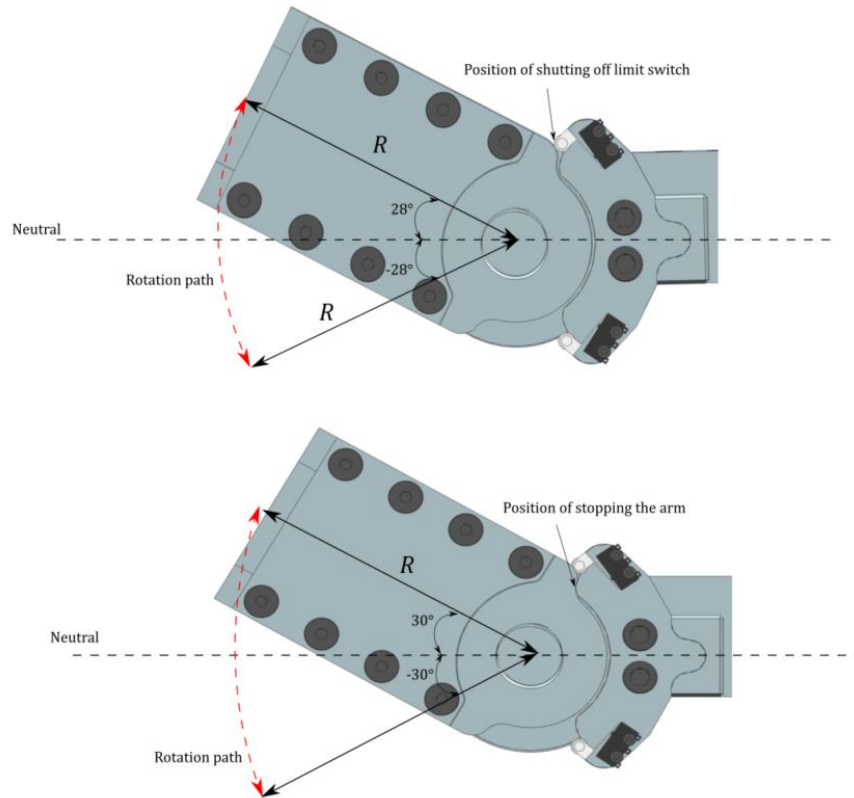
Figure 4.12: Rotation path of the hip roll arm.

4.2.3 Hip yaw

Fig. 4.13 displays the exploded view of the hip yaw assembly, which included the hip pitch housing as well. The movements of the hip yaw joint caused the pitch housing to move together. In addition, the pitch housing also played a critical role to clamp against the bearings inside the yaw housing. Table 4.7 shows names and functions of each callouts component.
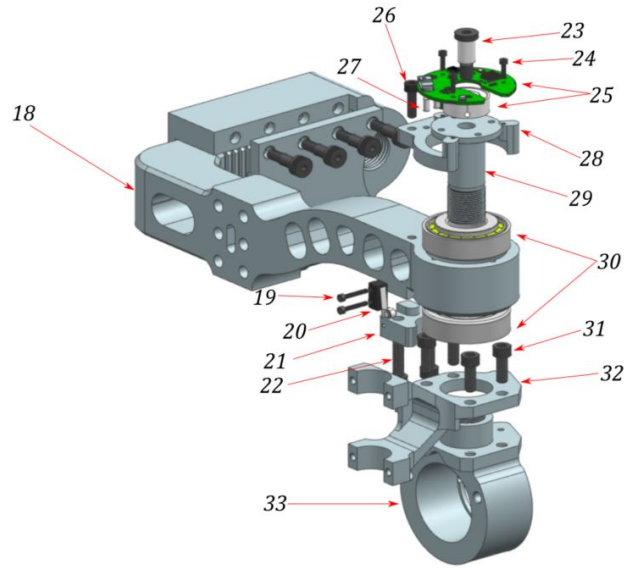
Figure 4.13: Exploded view of hip yaw assembly with labeled components.

Table 4.7: Summary of labeled components in hip yaw assembly

Label	Name	Functions
18	Hip yaw housing	Provides a connection between the roll and yaw joints
19	Socket head M2 bolt	Mounts the limit switches
20	Limit switch (one each side)	Shut off the power before hitting the hard stop
21	Hard stop	Stops the movement of the yaw joint at safe limits
22	Socket head M5 bolt	Mounts the hard stop in position
23	Bearing shaft M6	Clamps on the magnet ring
24	Socket head M2 bolt	Mounts the readhead board in position
25	Orbris$^{\text{TM}}$ encoder module	14 bits per revolution
26	Socket head M4 bolt	Mounts the encoder standoff in position
27	Dowel pin	Provides alignment for the standoff and the yaw lug
28	Readhead standoff	Keeps the readhead required distance from the encoder
29	Custom shaft bolt	Provides output transmission
30	Paired tapered roller bearings	Distribute radial and axial loads
31	Socket head M5 bolt	Mounts the hip yaw lug in position
32	Hip yaw lug	Supports the yaw actuator trunnion
33	Hip pitch housing	Provides the housing for pitch bearings
	Internal snap ring (not shown)	Retains the bearings from the other side

47

The hip yaw housing was one of the most significant parts in this yaw assembly because a variety of loads transmitted through this structure during operation of this exoskeleton. The load analysis of this piece was shown more in details in Section 5.1. Furthermore, it had other features besides serving as a housing. Fig. 4.14 illustrates the features this part possessed. As mentioned in the previous section, the frame part was fitted inside the U-channel of the roll arm (Fig. 4.10). The slotted channels were 4 mm spaced from center to center, and they were suited with the channels on the arm clamp (16). The clamp provided clamping forces on the housing frame, and the channels locked the frame in position, as shown in Fig. 4.15. A small clearance left between the clamp and the housing channels helped hold them tightly when clamping. Moreover, these channels could help adjust the hip breadth for different sizes of people. The maximum adjusting distance for each side was about one inch. A linear actuator was packaged at the side of this yaw housing to provide the output power for the yaw joint.
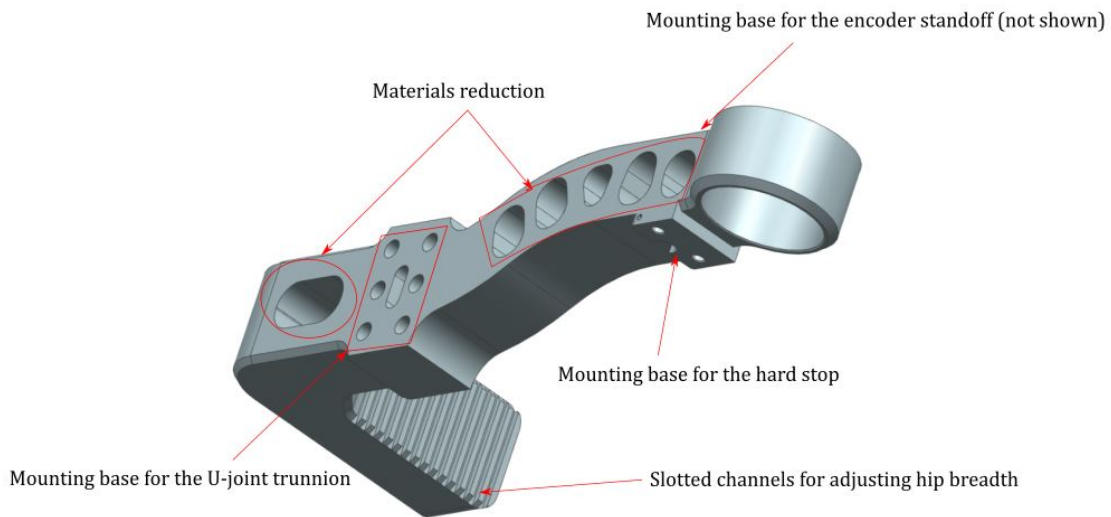
Figure 4.14: View of the hip roll housing with features.
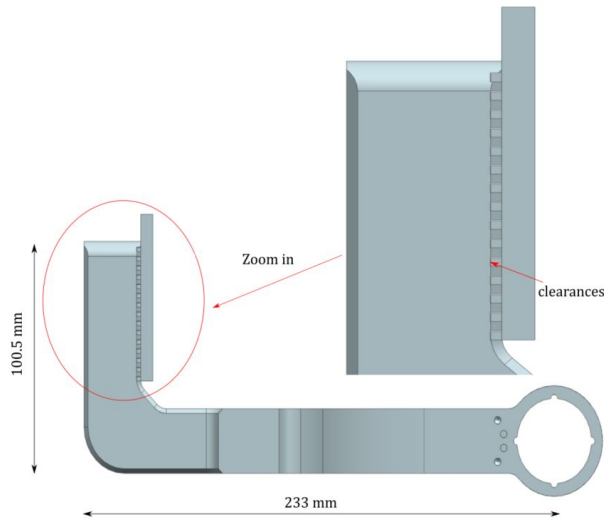
Figure 4.15: Top view of the yaw housing.

The design of the yaw joint was similar to the roll joint. As shown in the view-cut section of Fig. 4.16, the paired tapered roller bearings were clamped together inside the housing by the custom shaft bolt. Without the bearing spacer, the outer rings of these two bearings contact directly without touching inside cones. This back-to-back arrangement gave the effective load center-to-center distance of 19.03 mm, which was enough to distribute the radial loads. The selected encoder module was a non-touch true absolute rotary encoder, which was composed of a readhead board and a magnetized permanent ring. The encoder also had a feature of built-in self-calibration algorithm to improve the accuracy. The bearing shaft had a precision shaft diameter to hold the ring in position, as shown in Fig. 4.16.
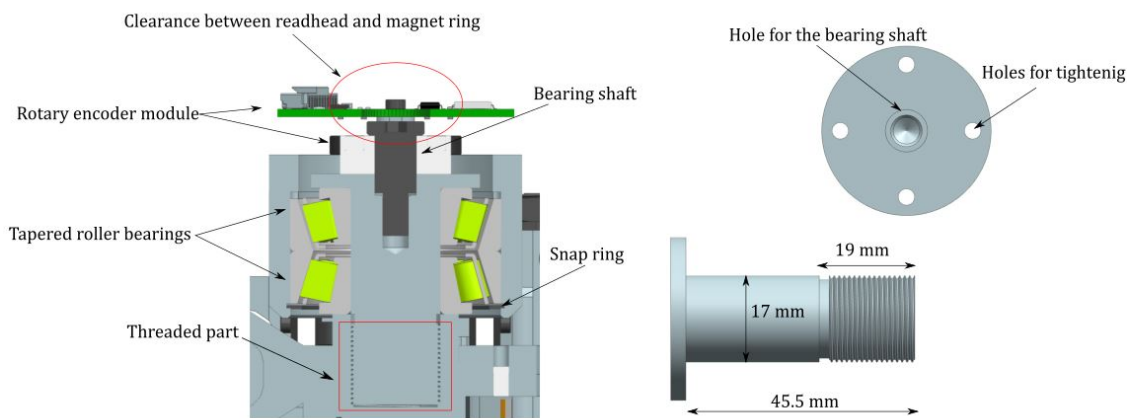
Figure 4.16: View-cut section of the hip yaw joint.

49

The movement path of the hip yaw joint was shown in Fig. 4.17. The external rotation was limited to 40°, while the internal rotation was limited to 30°. This range of motions was determined based on the travel length of the ball screw on the linear actuator. The moment arm R was 55.9 mm, which gave a peak angular velocity of 1.70 rad/s. The maximum impact load of hitting the hard stop was about 7.4 Ns at a 3g load. Similar to the roll joint, the limit switch was triggered first before the arm hit the hard stop, in order to protect the operator. Fig. 4.18 shows the moment when the yaw joint touched the hard stop.
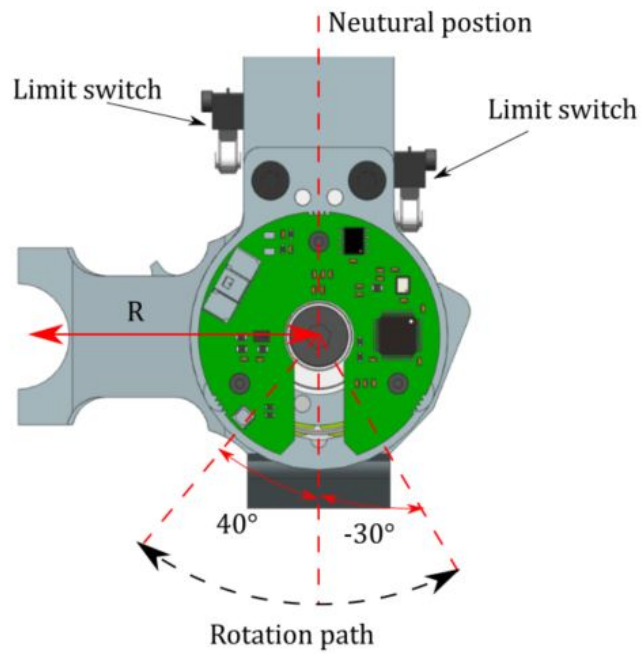
Figure 4.17: Top view of the movement path of the yaw joint.
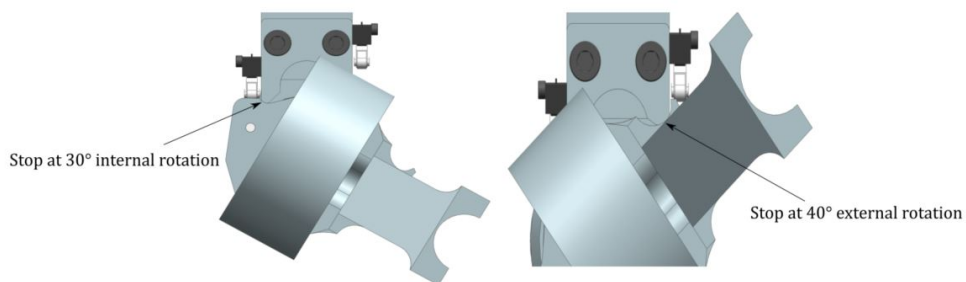
Figure 4.18: Bottom view of touching hard stop positions at the yaw joint.

4.2.4 Hip pitch

The design of the hip pitch joint focused on the bearing housing, bearings installation, the encoder installation, and the hard stop design. However, the packaging of the pitch actuator was not included because the design of the dual-motor actuator was not completed yet, and its packaging design will be involved the knee joint. The exploded view of the pitch assembly is shown in Fig. 4.19. The names and functions of each piece were listed in Table 4.8.
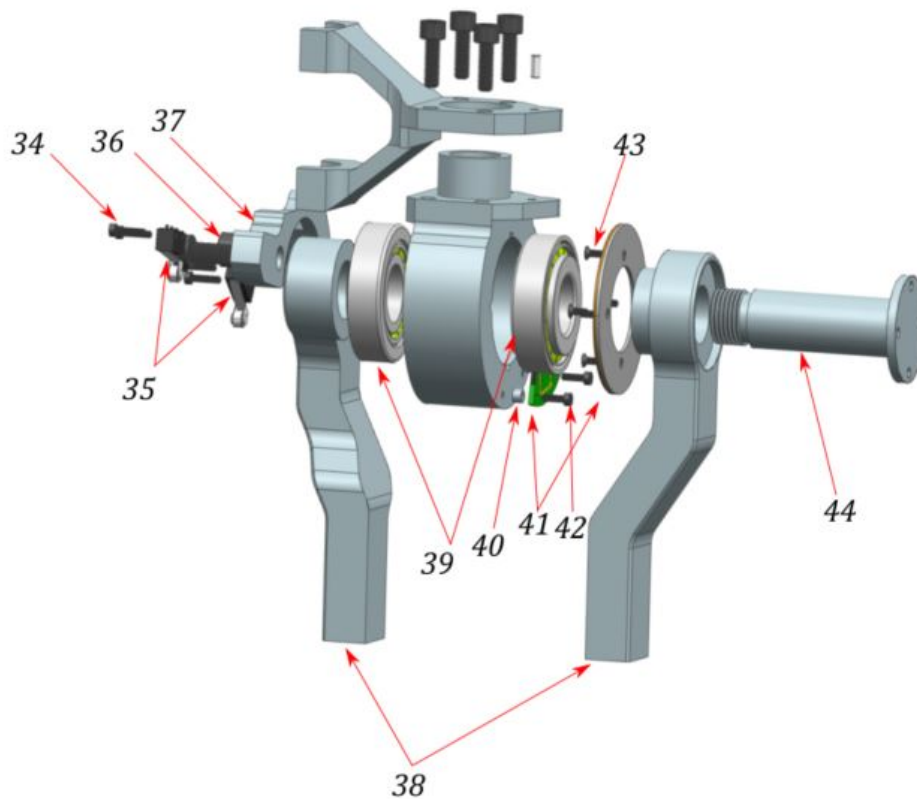
Figure 4.19: Exploded view of hip pitch assembly with labeled components.

Table 4.8: Summary of labeled components in hip pitch assembly

Label	Name	Functions
34	Socket head M2 bolts	Mount limit switches in position
35	Limit switches	Shut off the power before hitting the hard stop
36	Socket head M6 bolts	Mount the hard stop in position
37	Hard stop	Stops the movement of the roll joint at safe limits
38	Pitch arms	Transmit the motion of the hip pitch
39	Paired tapered roll bearings	Distribute radial and axial loads
40	Readhead standoffs	Keeps the readhead required distance from the encoder
41	AksIM^{TM} absolute ring encoder	16 bits per revolution
42	Socket head M2 bolts	Mount the readhead board in position
43	Flat head M2.5 bolts	Mount the magnet ring in position
44	Custom shaft bolt	Provides output transmission
	Internal snap ring (not shown)	Retains the bearings from the other side

The tapered roller bearings used for the pitch joint were the same as the ones for the yaw joint. The bearings were clamped inside of the pitch housing by a custom shaft bolt, which passed through pitch arms and the encoder. Fig. 4.20 displays a view cut section of the pitch joint. There was one pitch arm at each side of the housing, and they were both clamping against the inner cone of the bearings. This leads to a double-shear load applying on the joint for reducing individual bearing loads. The encoder module was the same type of encoder at the roll joint. The magnet ring was mounted on the backside of the pitch arm, and the readhead board was mounted on the side of the housing. This packaging of the encoder module made the whole joint assembly compact and, in the meantime, hid electronics away from the operator's body.
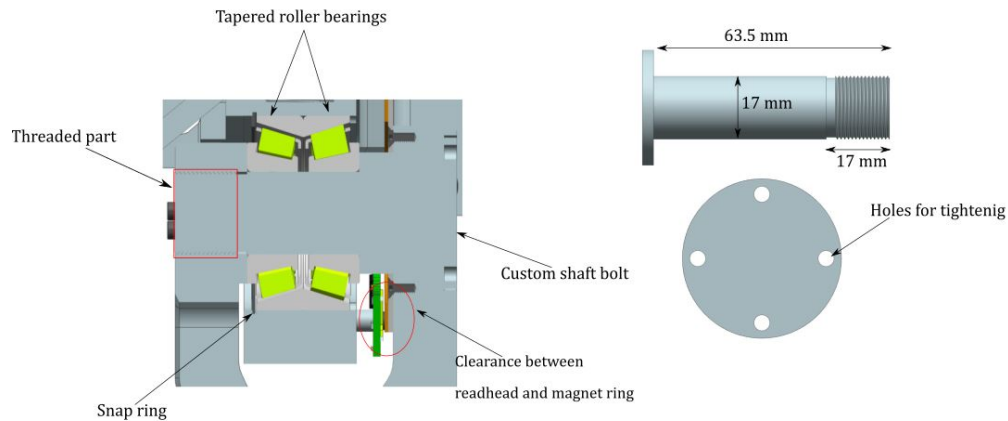
Figure 4.20: View cut section of the hip pitch joint.

As for the hard stop, it was placed on the other side of the housing and aligned with a pocket slot of the housing. The motion of the arm was limited to 100° for the leg flexion and 30° for the leg extension, as shown in Fig. 4.21. Note that the shape of the arm was designed to avoid interfering with the travel of the actuator ball screw. Since the pitch actuator has not been placed yet, the moment arm length was unknown at this time. The hard stop might need to be modified to accommodate to lower lever design.
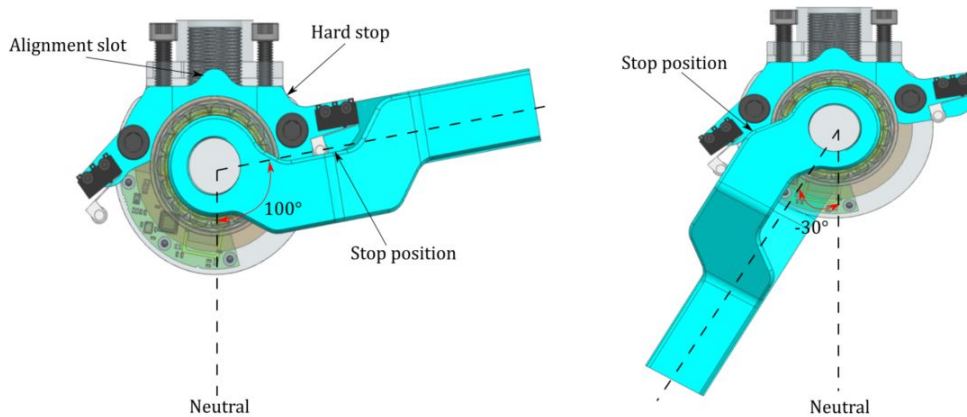
Figure 4.21: Side view of touching hard stop positions at the pitch joint.

4.3 Actuators Packaging

4.3.1 Introduction

Each joint at the hip exoskeleton was actuated by a linear actuator with a precision ball screws. Linear Series elastic actuators (LSEAs) were used for both roll and pitch joints, and there was no elastic component for the linear actuator at the yaw joint. A mechanical power generated by the motor increased the torque output through a gear reduction and transmitted the load through a ball screw to the actuated joint. The compliant element that was placed series with the actuator enabled impact resistance and energy storage. The overall packages of LSEAs gave an advantage of high bandwidth force control. Fig. 4.22 shows the single-motor and dual-motor actuators designed by my co-worker, John Kendrick. Table 4.9 gives some specifications of these actuators at each joint. In this chapter, the topics focus on the packagings of each actuator at roll and yaw joints, respectively. The packagings included a two-bar linkage mechanism, yokes and lugs design, a spring mount design, and bearings selection.
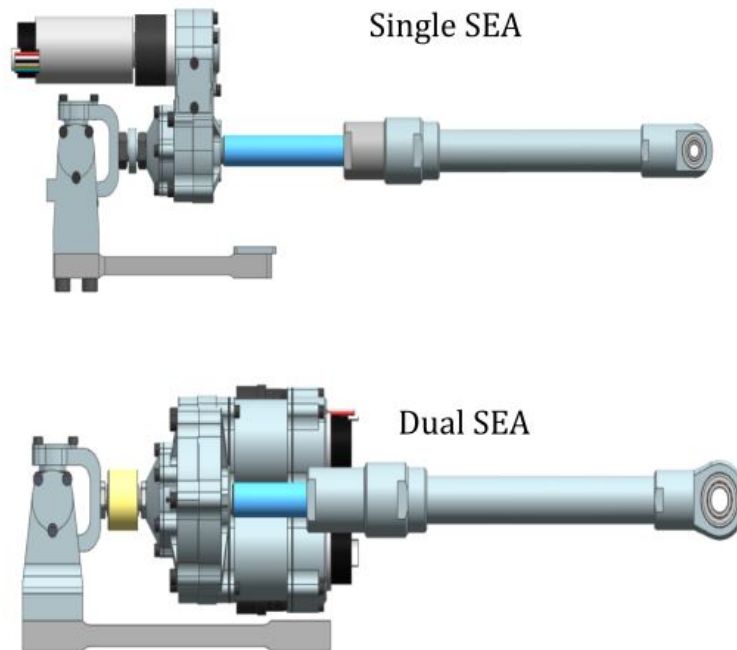
Figure 4.22: Single-motor and dual-motor actuators designed by John Kendrick.

Table 4.9: Summary of the actuators at each hip joint.

Joint	Linear velocity (m/s)	Peak force (N)
Roll	0.058	4649.7
Yaw	0.095	2818
Pitch	0.267	6730

4.3.2 Two-bar linkage mechanism

Fig. 4.23 displays a simple two-bar linkage mechanism used to drive the hip roll and yaw joint. $|\mathbf{AB}|$ was the constant moment arm between the joint and the force input position, while $|\mathbf{BC}|$ was the distance between the force input position and the universal joint. The ball nut started traveling at the neutral position, which was perpendicular to the moment arm. At the same time, the ball screw length between $\mathbf{B}$ and $\mathbf{C}$ would change until the arm hit the limit of the rotation. In order to better understand the relationships of each parameter, the position and force analysis was developed.
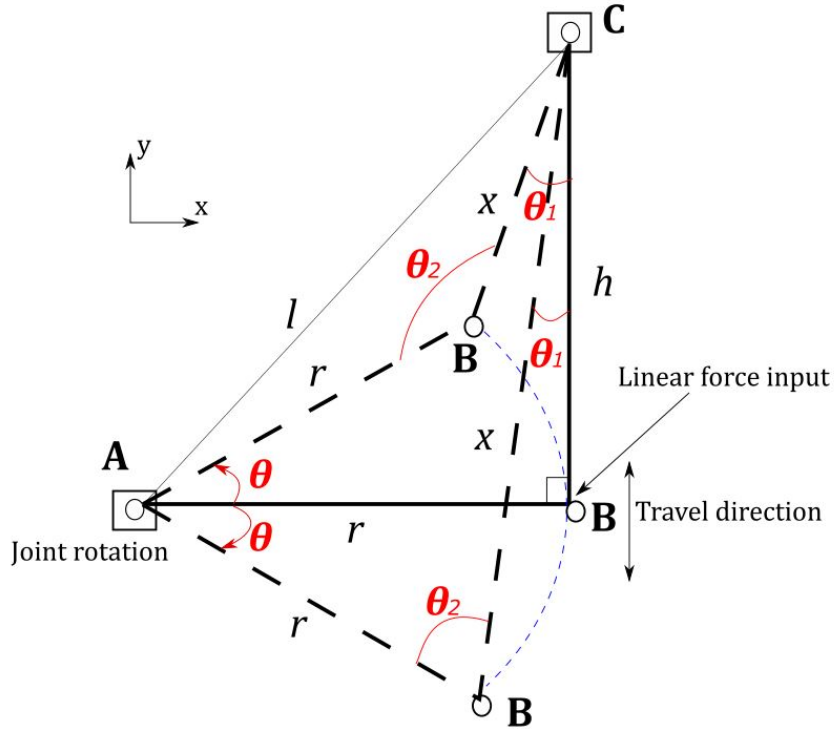
Figure 4.23: Two-bar linkage Mechanism used for geometric analysis.

Set $\mathbf{A}$ as origin, and use vector matrix to represent each point:

$$\mathbf{A} = \begin{Bmatrix} 0 \\ 0 \end{Bmatrix}, \quad \mathbf{B} = \begin{Bmatrix} r\cos\theta \\ r\sin\theta \end{Bmatrix}, \quad \mathbf{C} = \begin{Bmatrix} r \\ h \end{Bmatrix} \tag{4.5}$$

The distances of $|\mathbf{AB}|$, $|\mathbf{BC}|$, and $|\mathbf{AC}|$ can be determined as follows:

$$|\mathbf{AB}|^2 = r^2 \tag{4.6}$$

$$\begin{aligned} |\mathbf{BC}|^2 &= (\mathbf{B} - \mathbf{C}) \cdot (\mathbf{B} - \mathbf{C}) \\ &= r^2(2 - 2\cos\theta) + h^2 - 2rh\sin\theta \end{aligned} \tag{4.7}$$

$$|\mathbf{AC}|^2 = r^2 + h^2 \tag{4.8}$$

By using the triangle theorem, the angle of θ_2 is calculated as following:

$$\begin{aligned} \cos\theta_2 &= \frac{|\mathbf{AB}|^2 + |\mathbf{BC}|^2 - |\mathbf{AC}|^2}{2|\mathbf{AB}||\mathbf{BC}|} \\ &= \frac{r(2 - 2\cos\theta) - 2h\sin\theta}{2\sqrt{r^2(2 - 2\cos\theta) + h^2 - 2rh\sin\theta}} \end{aligned} \tag{4.9}$$

Therefore, by using equations calculated above, the universal joint angle, θ_1 and the travel distance of the ball nut , ΔX were calculated below:

$$\theta_1 = \theta_2 - \theta - 90° \tag{4.10}$$

$$\Delta X = h - x$$
$$= h - \sqrt{r^2(2 - 2\cos\theta) + h^2 - 2rh\sin\theta} \tag{4.11}$$

As for the force analysis, the input load was always transmitting along the ball screw, which was in the direction of **CB**. Since the longest moment arm was at the neutral position, the input load at this position gave the highest torque and speed. When the ball screw was not vertical with the moment arm, components of forces were generated. Expressions that showed the relationship of the torque and angular speed versus the angle between **AB** and BC are shown below:

$$T = Fr\sin\theta_2 \tag{4.12}$$

$$w = \frac{v\sin\theta_2}{r} \tag{4.13}$$

where F was the actuator input load, and v was the displacement velocity of the ball screw.

A MATLAB script was written to solve the results of the universal joint angle, ball screw travel length, the output torque, and the output angular velocity due to the rotation of each joint, as shown in Fig. 4.24 and Fig. 4.25. These results from calculations could help determine the length of the ball screw and the packaging size of the universal joint. Table 4.10 shows critical data from the MATLAB plots. Yaw joint had a much larger range of motion than the roll joint. Therefore, the required ball screw length for the yaw joint was going to be longer. As expected, the speed of the yaw joint was faster than the roll joint. The output speeds and torques almost all met the requirements in Table 3.11. However, the output speed of the yaw joint was only 0.1 rad/s off because of the limit of the packaging size for the actuator.

Table 4.10: Data from MATLAB results

Joint	Max. U-joint(deg.)	Total travel distance (mm)	Max. Torque (Nm)	Max. speed(rad/s)
Roll	2.29	46.37	215.75	1.25
Yaw	3.99	64.11	157.53	1.70
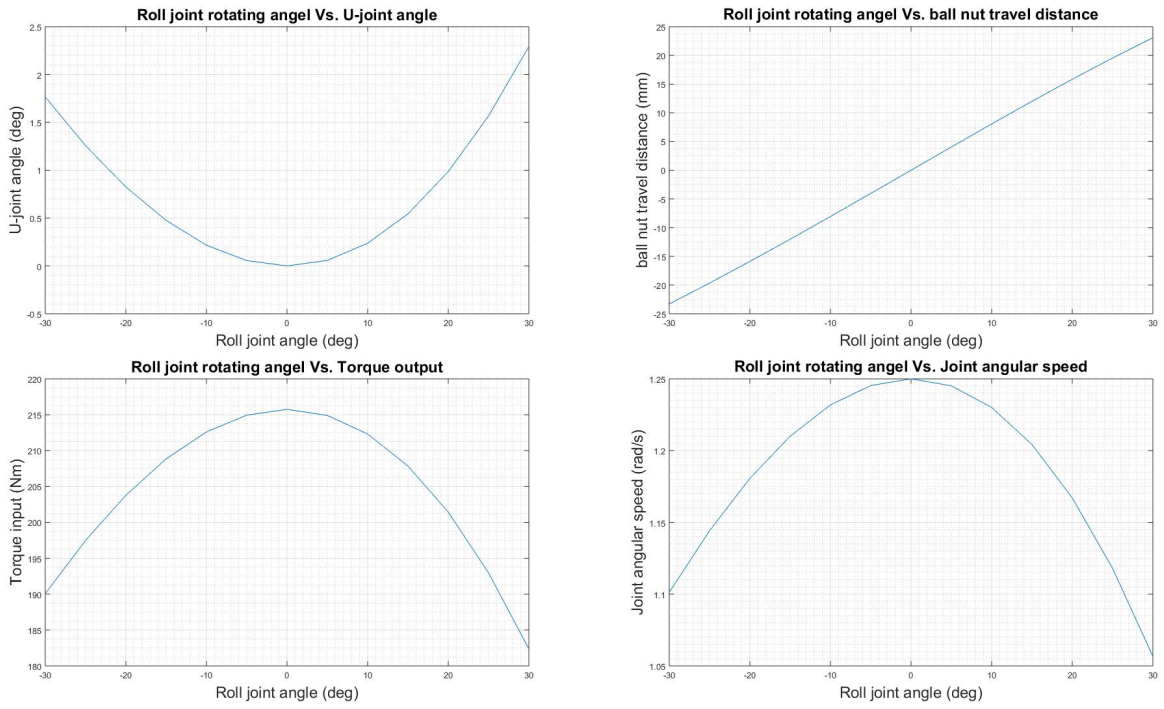
Figure 4.24: Roll joint data output window from MATLAB.
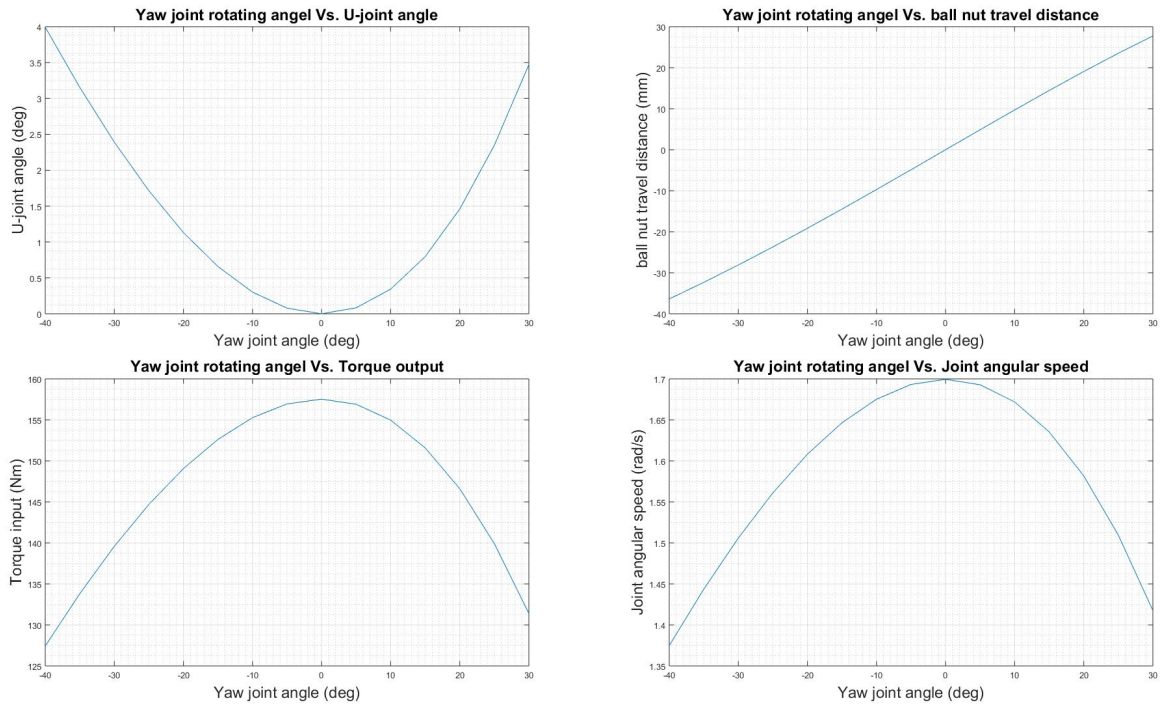
Figure 4.25: Yaw joint data output window from MATLAB.

4.3.3 Packaging

Fig. 4.26 displays an overview of the packaging of the actuator roll and yaw joints, respectively. The highlighted blue parts were custom-made to mount the actuator onto the exoskeleton structure, including leaf spring mounts, lugs, and yokes. The highlighted red parts were needle roller bearings used to support the input forces exerted by the actuators. The highlighted orange assemblies were the actuators designed by John Kendrick.
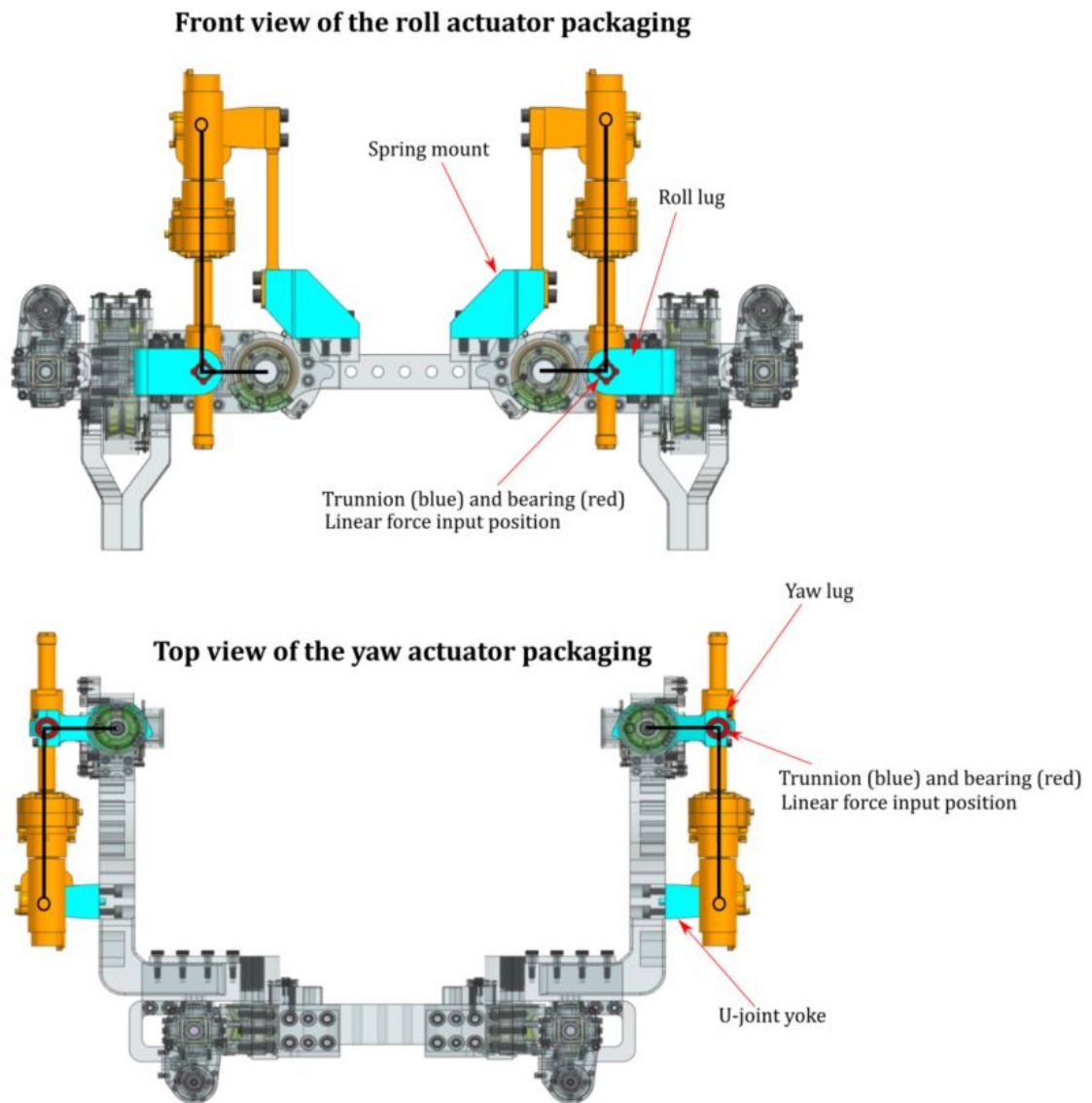
Figure 4.26: Views of the actuators packaging including two-bar linkage mechanism.

The spring mount was mounted on the hip roll housing, which was a fixed part relative to the operator's body. The spring was aligned and clamped inside of the pocket of the spring mount. Since the mount was off axis from the load center, both shear and moment reactions acted on this part, as shown in Fig. 4.27. The ramp shape of the mount made the structure stiff and stabilized the part. A pattern of M8 bolts was used to mount the spring mount and support a large amount of the axial and shear reaction forces.
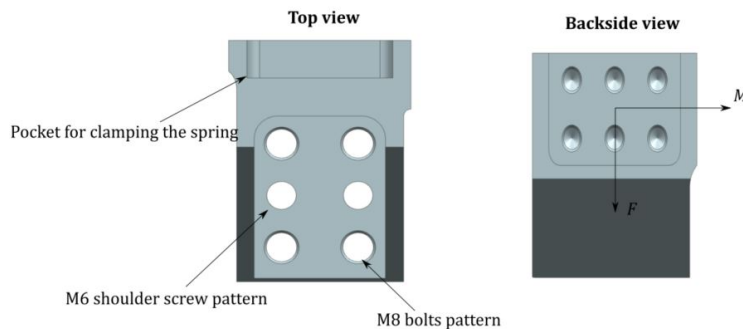
Figure 4.27: Views of the spring mount.

The yoke that supported the universal joint of the yaw actuator was mounted on the side of the hip yaw housing. A pattern of six M6 bolts helped secure the yoke, and these bolts purely experienced shear reactions due to the input of the actuator. The function of both roll and yaw lugs was to support the trunnion that was attached to the ball nut. The roll lug was designed to mount on the hip roll arm, as shown in Fig. 4.10. The lug was secured by M6 bolts, washers, and nuts, and these bolts would undergo shear and axial reactions. This bolted joint design left enough clearance spaces for the movement of the ball screw. As for the yaw lug, it was mounted on the top of the pitch housing. The inner pocket was used for alignment, and could slide fit onto the circular flange, which was used to clamp against on the bearings inside the yaw housing. The pattern of four M5 bolts was robust enough to handle the shear reactions due to the input force. The lips on the lug were used to do a normal contact with the limit switches. For installing the bearings, one bearing could fit directly into the housing at the roll arm, and the other bearing installed into the housing of the roll lug. There were removable clamps attached to the housing of the yaw lug providing a convenient installation of bearings. These needle roller bearings were selected to distribute the radial loads resulted from the force input. The maximum radial force exerted by the ball screw for one bearing was about 2.3 kN. However, the selected bearings had a static load of 8.15 kN and a dynamic load of 6.71 kN, which were both far above the maximum radial load. Maintaining the peak force below the static and dynamic ratings secured the lifetime of these bearings and protected the shaft of the trunnion from damages. Fig. 4.28 illustrates the features of the yaw yoke, the yaw lug, and the roll lug.
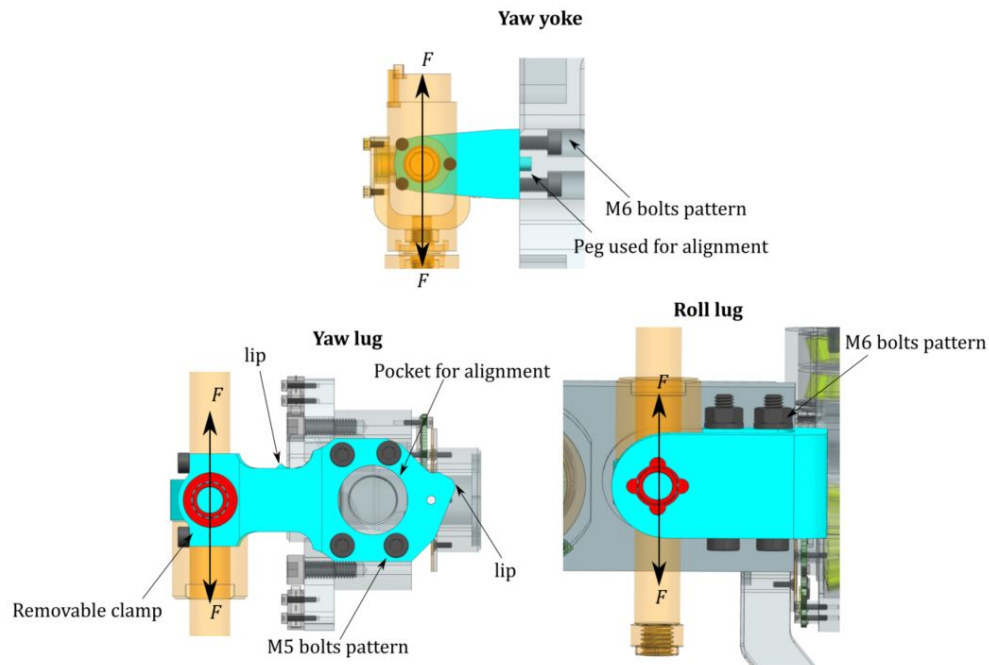
Figure 4.28: Views of the actuator fixtures.

4.4 Backpack Design and Packaging

Several electronics hardware needed to be carried as the operator driving the exoskeleton, such as batteries, a radiator, motor controller boards, power distribution boards, IMU, etc. The idea that was similar to other exoskeleton products was mounting heavy and large size of hardware onto the backpack of the exoskeleton. However, designing a whole backpack will be involved with harnessing problems. Harnessing can be another big topic, which is time-consuming and involved many test experiments. One creative idea was to draw on the experiences of off-the-shelf external frame backpacks.

One of the remarkable features of the off-the-shelf backpacks was the comfortable harnessing. External frame backpacks have been used for hiking and long journey trips for years. The theory of framing and comfortability has been developed by experts. Therefore, using an off-the-shelf backpack that had the proper size of the external frame for installing the hardware was a good option. Fig. 4.29 shows the external backpack frame product from KELTY [69] and the NX CAD modeled frame part. This CAD model restored the upper part of the frame. The lower part was replaced by a design of backpack plate, in order to accommodate to the exoskeleton structure.
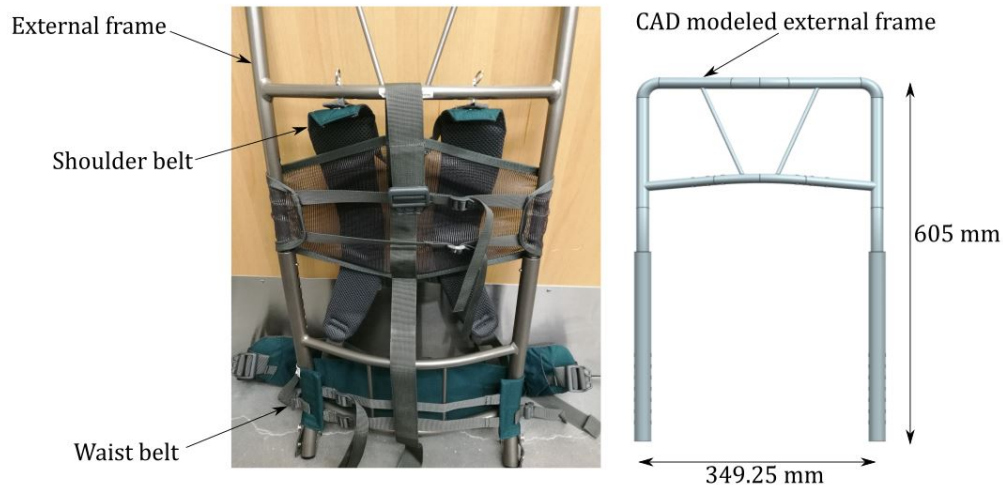
Figure 4.29: KELTY external frame backpack product (left picture) and its upper frame CAD model (right picture).

Fig. 4.30 shows the design of the backpack plate. The major functions of this plate were to provide a base for the external backpack frame and the waist belt harness. The height of this plate was designed to avoid interferences with the structures of the exoskeleton. Two cylinders were bolted on the top of the plate so that the backpack frame could slide onto them, and the frame was fixed by set pins. In addition, there was a pocket on the plate, which allowed for installing the battery cases. The case had slots for fitting buckle straps to fix batteries in position. Total two batteries were used to generate 22000 mAh and 50 V of power. The plate was set onto the hip roll housing by a pattern of M8 bolts, washers, and nuts. Between the plate and the housing, there was a removable spacer, as shown in red color in the right picture of Fig. 4.30. The purpose of this spacer was to adjust the housing's distance to the operator's back, in order to match the pitch joint of the exoskeleton with the operator's joint position. The spacer could be easily machined to be different thicknesses as necessary. In order to prevent the plate from bending due to payloads, a plate support that had a ramp shape connected the plate with the housing. In addition, a 1/4" thickness of ABS plastic sheet was clamped on the backpack frames as a mounting base for the hardware. ABS is a strong and light material, which can have over 44 MPa tensile strength [13]. The ABS sheet can be easily manufactured using a laser-cutting machine. Fig. 4.31 shows the first-cut layout of some electronics hardware attached to the plastic sheet. The highlighted blue part was the backpack plate, the pink part was the cylinders fitting into the backpack frame, green part was the battery case, red part was the spacer, and orange part was the plate support. The heavy and large hardware, such as batteries and the radiator was modeled and mounted close to the waist, in order to stabilize the whole system at the operator's gravity center. At this time, not all of hardware had been determined, so the details of the hardware layout can be further developed.
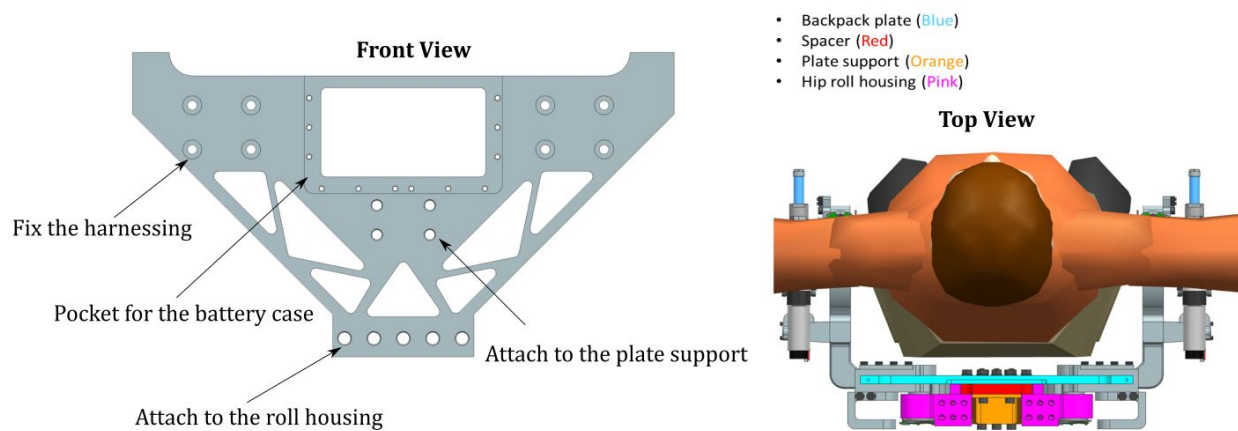
Figure 4.30: Views of the backpack plate.
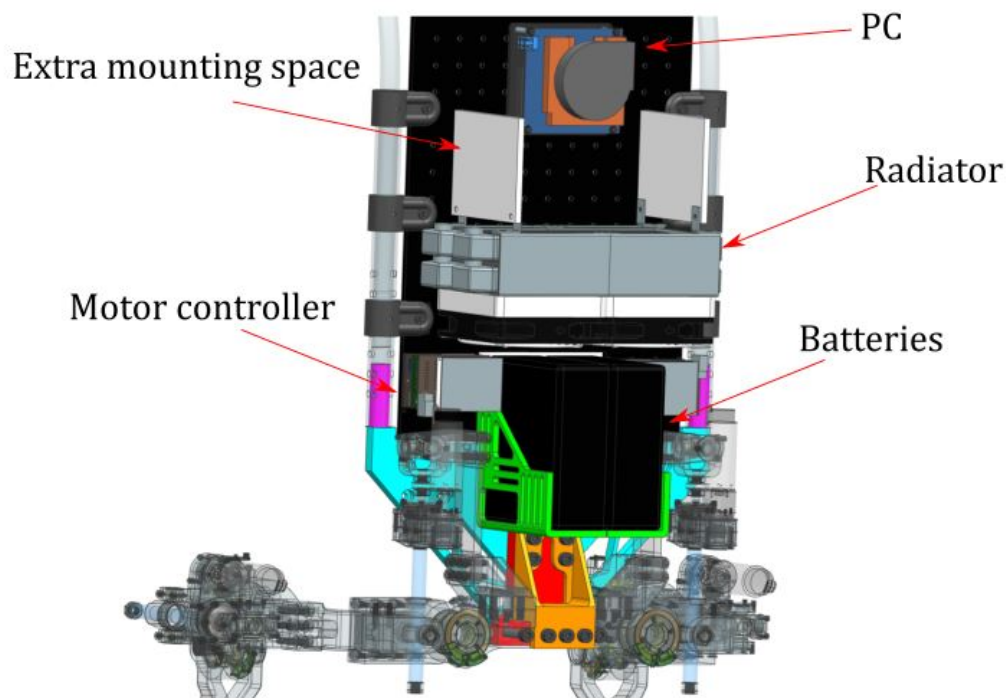
Figure 4.31: A layout of electronics hardware on the backpack.

Chapter 5

Verification

5.1 Finite Element Analysis

The robustness of the exoskeleton structure was the major concern before beginning manufacturing. Finite element analysis (FEA), as one of the computer-aided engineering (CAE) methods, provides a numerical solution for predicting the performance of the structures, especially showing stress concentrations for indicating whether the part will fail over the yield strength. In this section, FEA was conducted on critical parts of the hip exoskeleton by using ABAQUS software.

Before running the model of the components in ABAQUS, some preparations needed to be done, such as partitioning the model, assigning material properties, defining boundary conditions, creating interaction constraints, etc. One of the critical factors affecting results was selecting the element type for the mesh elements. Since the models were all in 3D solid, one possible element type was fully integrated hexahedral elements (C3D8), which has two degrees of freedom (DoF) in each coordinate direction and gives eight integration points in total. However, in some cases, shear locking can happen when the elements have a large aspect ratio. The shear locking can make the elements lose accuracy when simulating the performance of the local areas. In order to cope with this problem, Reduced Integration (C3D8R) and Incompatible Mode (C3D8I) were introduced. According to [70, 71, 72], both C3D8R and C3D8I have abilities to relieve shear locking problems. The pro of C3D8R is greatly reducing the solution times, while the con is that it has an issue of hourglassing, which leads to a lack of elements stiffness [70, 72]. On the other hand, C3D8I has one additional degree of freedom (total 24 DoF) to model the behaviors of elements better, but the downside of this element is that it can make elements too stiff [70, 72, 71]. Based on the tested results from [70, 72], C3D8I had better accurate simulations for the results and faster convergence for the model analysis than C3D8R, which might require very fine mesh to achieve good results. Therefore, C3D8I was chosen for the model analysis of the exoskeleton

structures.

Hip yaw housing

Hip yaw housing was one of the most critical components in this hip exoskeleton because all of three DoF were connected through this part, and their transmissions of loads and motions were through this part as well. There were multiple load cases needed to analyze. One of the most extreme ones was the ground reaction force, which was axially loaded on the yaw joint. In this case, the situation was assumed that the gravity of the operator and exoskeleton was acting on one leg at a 3g load condition. Thus, this situation resulted in a ground reaction force of 4500 N exerting on the yaw joint. Fig. 5.1 shows the boundary and load conditions for the partitioned yaw housing assembly in ABAQUS window. This assembly had following components: the roll arm, the roll shaft, the bearing of roll joint, the needle roller bearing for the roll actuator lug, and the yaw housing. For the constraint conditions, The yaw housing frame part was installed inside the roll arm constrained by surface-to-surface contact interactions. The shaft also passed through the pocket of the arm and the roll bearing hole, which were applied with contact interactions. For the boundary conditions, the roll arm should be constrained by both the roll joint bearing and the needle roller bearing at the roll arm. Thus, these two bearings were both fixed in axial rotations and displacements and radial displacements. However, the roll shaft was only constrained in axial displacement, in order to allow the shaft to rotate freely.
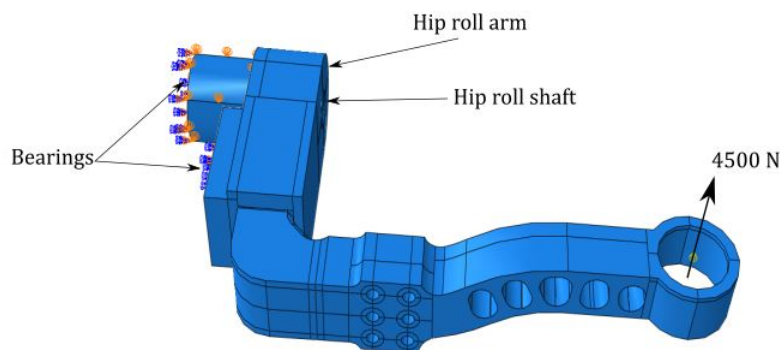
Figure 5.1: A 3g load of the ground reaction force at the yaw housing from ABAQUS window.

The material property used for the arm and the housing was Aluminum 7075 T6, which was described in Table. 4.4. With the C3D8I element type of the mesh and 1 mm of element size in edge seeding, the FEA results of this load case are shown in Fig. 5.2. The frame of the housing had an apparent failure in those gray areas where the frame had direct contacts at the corners of the roll arm. However, an observation at the failure positions

shows that only a few of the elements failed, and the failure did not penetrate across the frame. Therefore, there was a doubt if this failure was an artifact caused by singularities contacting sharp corners. One method was to check if there was a stress convergence at other stress concentration areas. If the other areas were converging much greater than the failure area, the failure probably was caused by an artifact.
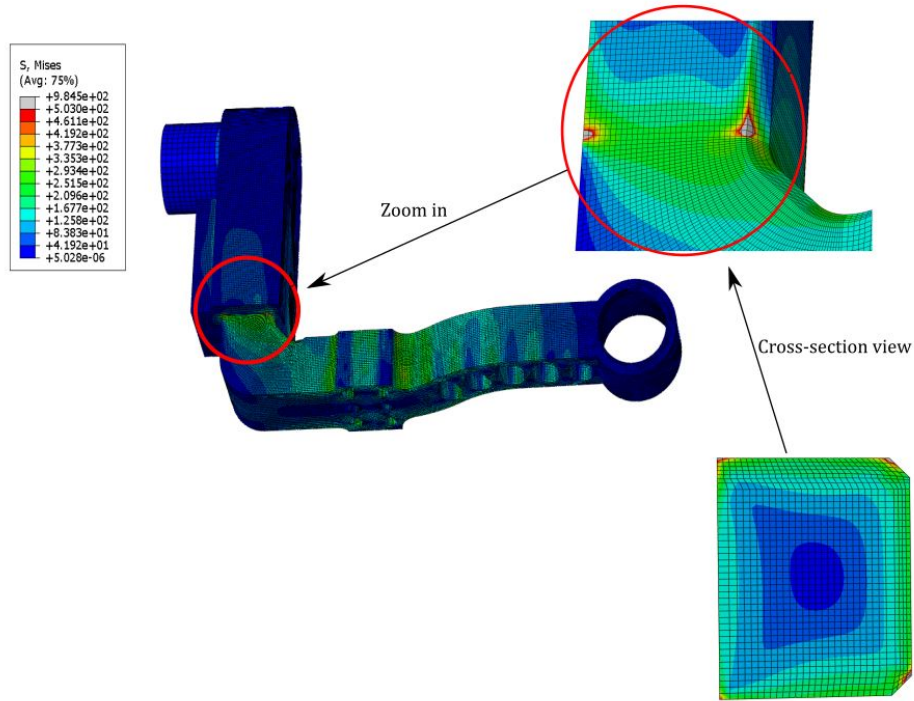
Figure 5.2: FEA results of the yaw housing at 1mm edge seeding size.

Fig. 5.3 displays FEA results from different sizes of elements. The stress concentration area was picked at the fillet. Table 5.1 lists the highest stress in this area compared to that at the failure position. From the table, the percentage difference at the fillet between 1 mm and 1.5mm was about 0.47%, while the percentage difference for the failure stress was over 10%. Moreover, as the element size became smaller, the stress at the fillet was obviously converging much faster than the stress at corners. Therefore, a reasonable conclusion was that the stresses at the corner contact were artifacts, and the elements there was not simulated accurately even in a finer mesh. A safe estimation of the maximum stress concentration for this housing was about 300 MPa because this maximum stress was found in most of the concentration areas. Therefore, this gave a factor safety of 1.67 with 503 MPa yield strength for Aluminum 7075 T6.
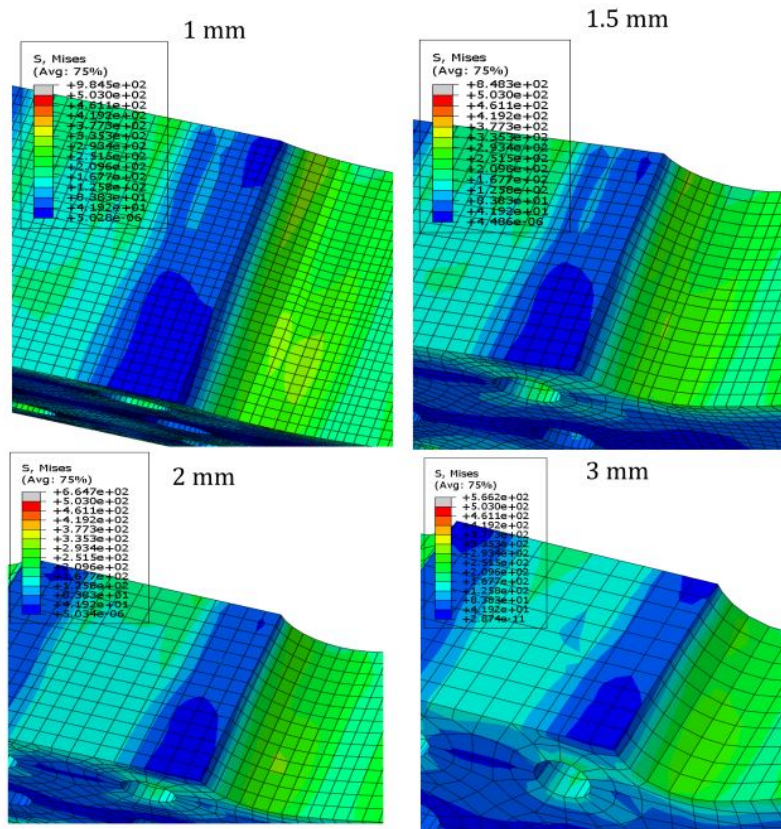
Figure 5.3: FEA results of the yaw housing at the fillet with different mesh element sizes.

Table 5.1: Highest stresses comparisons at different mesh sizes of elements.

Element size	Max. stress at the fillet (MPa)	Failure stress at corners (MPa)
1 mm	299.331	939.81
1.5 mm	297.915	848.26
2 mm	295.693	664.7
3 mm	287.081	566.2

After examining the FEA results of the yaw housing, some areas had very low stresses, even zero stresses. Thus, these materials could be eliminated to reduce the weight of the part. The other situation for this load case was that the frame part was moved out one inch from the roll arm. As shown in Fig. 5.4, the stress artifacts still happened at the corners as the frame part moved out. However, the maximum stress in stress concentration areas was around 330

MPa, which provided a safety factor of 1.5. Therefore, one inch was a safe adjustability for this load case.
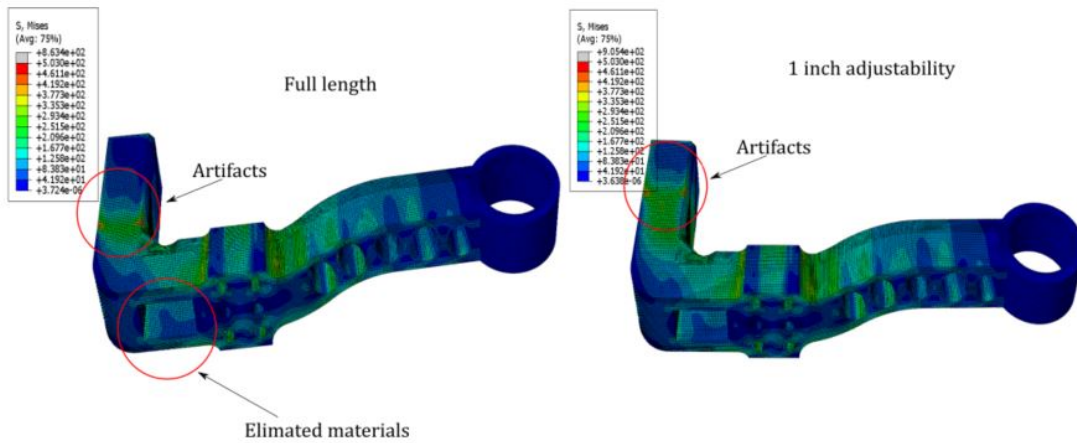
Figure 5.4: FEA results of 1 inch adjustability the yaw housing.

There were other extreme situations, which made the yaw joint experience radial reaction loads. Fig. 5.5 displays the load cases in ABAQUS window for the yaw housing in 100° flexion and 30° abduction, respectively. The FEA results of 1 mm edge seeding sizes are shown in Fig. 5.6, which also includes the adjustability condition. Note that there were artifacts in hip flexion cases because of hitting the corners of the roll arm. The factor safety of these cases were all greater than 1.26, which was fine given in a 3g load condition.
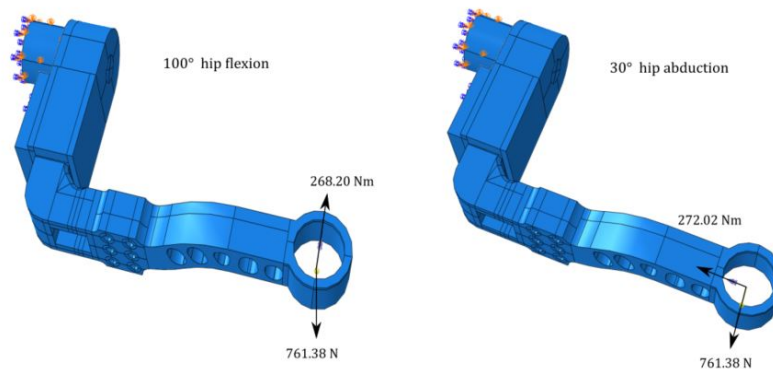
Figure 5.5: A 3g load of reacting moments and forces at the yaw housing.
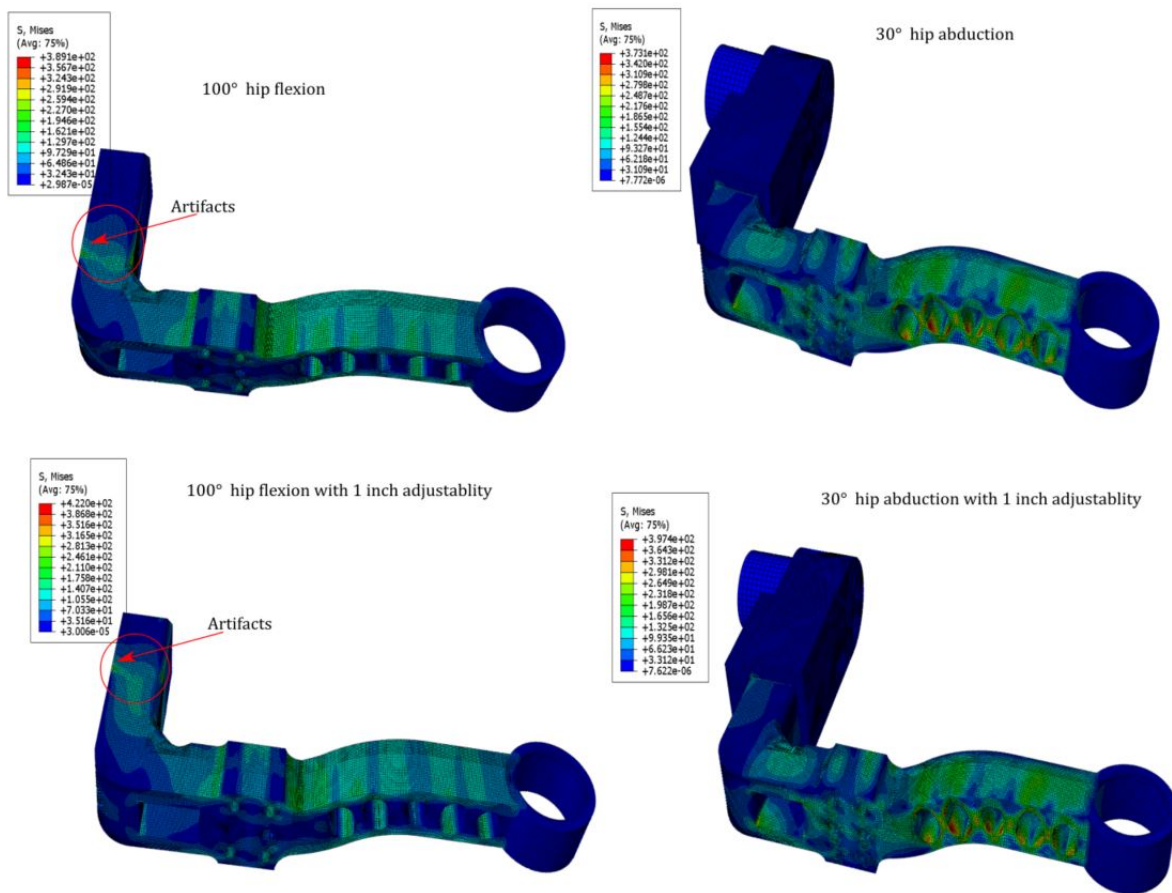
Figure 5.6: FEA results of reacting moments in hip flexion and abduction, respectively.

Hip pitch housing

Another important part was the pitch housing, which experienced reacting moments and forces at the limits of the range of motions. As shown in Fig. 5.7, the partitioned pitch housing assembly (left picture) was composed of the pitch housing, the yaw bearing, and the shaft custom bolt. The bearing was axially fixed in both rotation and displacement. There were surface-to-surface contact interactions between the bearing and the shaft bolt. The threaded part of the shaft bolt was tied-constraint into the pocket of the pitch housing. The performance of the shaft bolt would experience a bending condition. The FEA result (right picture) of 1 mm mesh sizes shows that the stress concentration was at where the shaft contacted with the edge of the bearing. The reason for this was that the reacting moment exerted on the housing caused the yaw shaft to bend against the edge of the bearing. In fact, the stress concentration there could be relieved more if chamfers were added to the

edge of the bearing. But the feature of chamfers was not easily partitioned in the ABAQUS and most often caused zero or negative elements. In this assembly, the shaft was made of StressProof® 1144, which has 689 MPa of the yield strength, as shown in Table. 4.4. Therefore, safety factor at this extreme stress situation was achieved over 1.43.
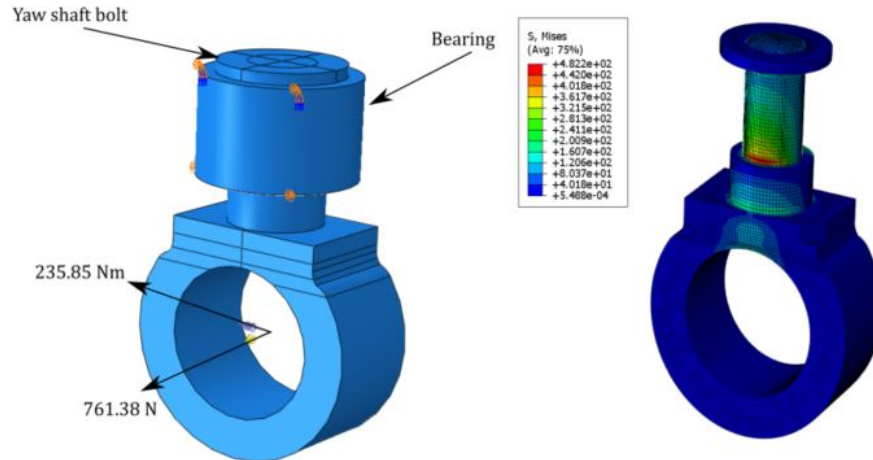
Figure 5.7: 3g loads of reacting moment and force at the pitch housing.

Hip roll housing

The hip roll housing took the most reacting moments among the three joints, so the strength of its frame structure must be tested. Fig. 5.8 shows the partitioned roll housing assembly and the FEA result. With one end fixed on the bearing, the other end experienced the reacting moment and load at a 3g factor. From the FEA result, it was shown that the stress distributions at the housing beam part were induced by torsions, and the stresses were concentrated around the holes. In the updated model shown in Fig. 4.9, the hole pattern was reduced to five holes, which increased the gap between holes and reduced the stress concentrations around holes. Therefore, the safety factor of this part was greater than 1.5 for the material made of Aluminum 7075 T6.
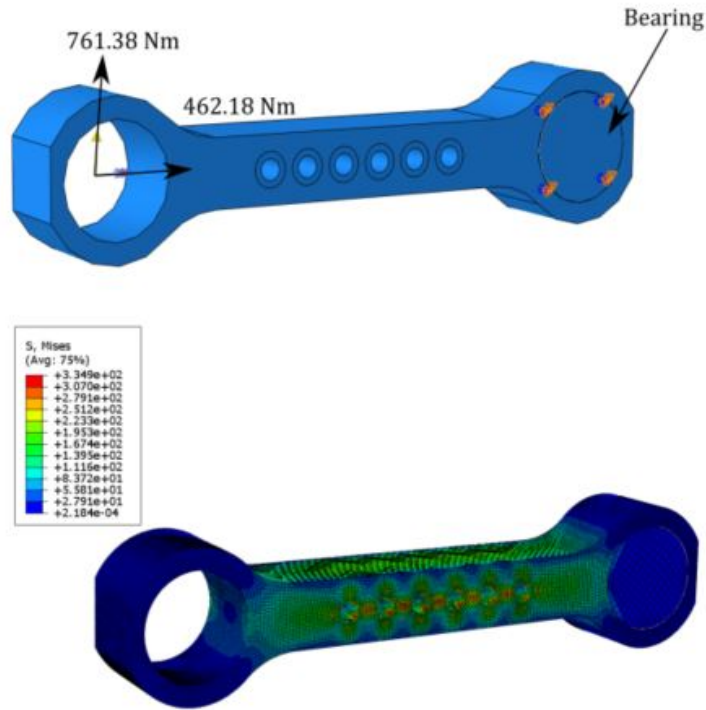
Figure 5.8: A 3g load of the reacting moment and force at the roll housing.

Leaf Spring Mount

Fig. 5.9 displays the FBD of the partitioned leaf spring assembly when the leaf spring experienced the input force in either direction. The clamp plate, the leaf spring, and the yoke in this assembly were all modeled by my co-worker, John Kendrick. The input actuation force acted at the center of the yoke that held the universal joint. The spring mount was bolted onto a base, which was fixed as a boundary condition. The upper side of the leaf spring was mounted with the yoke, and the bottom side was clamped inside the pocket of the spring by M6 bolts. The spring had surface-to-surface contact interactions with both the spring mount pocket and the yoke. The bolts were all exerted by a certain amount of preload to provide clamping forces starting at the initial stage of the simulation.
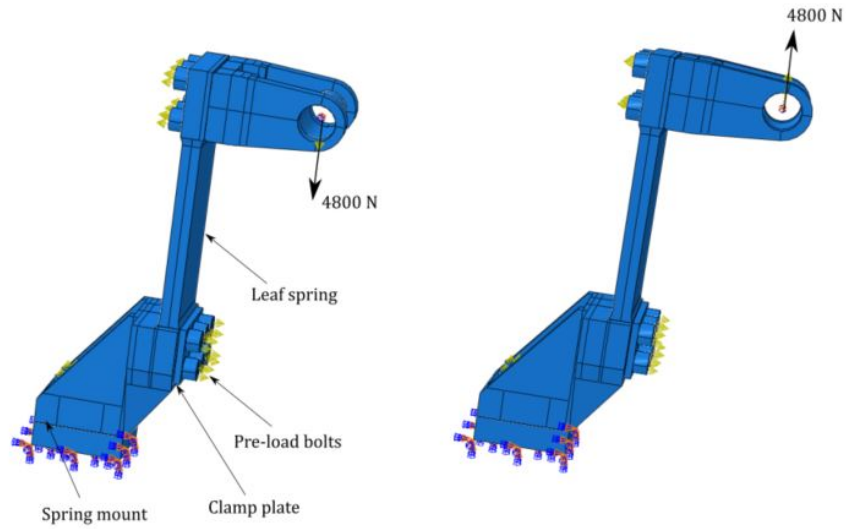
Figure 5.9: An assembly of the spring mount with the leaf spring exerted by an input force.

Fig. 5.10 shows the FEA results of the spring mount. The spring mount experienced shear forces and moments as the input force acting at the U-joint. As shown in the figure, there were stress concentrations around the bolt holes inside the pocket. These stresses were caused by the reaction forces on the bolts when the spring was pulled by the input force. However, this part was still robust enough to provide the safety factor over 1.4.
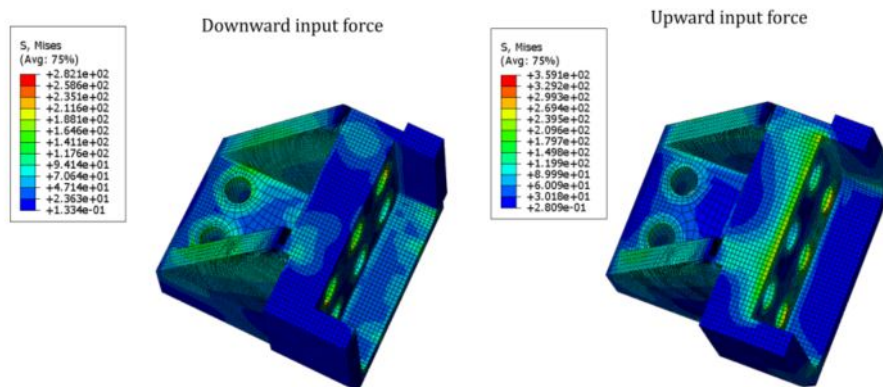
Figure 5.10: FEA results of the spring mount in either force direction.

Fig. 5.11 shows the FEA results of the stresses and displacements for the leaf spring in either force direction. These FEA simulations were developed by John Kendrick. The spring length in total was 144 mm with effective elastic length of 114 mm. The thickness of the spring was 8 mm, and the moment arm was 50 mm. His designed dimensions of this spring were calculated from the equations developed in Section 2.1. The magnitudes of the deflections at the center of the yoke were 9.72 mm and 9.62 mm in two force directions, respectively. Thus, the elastic stiffness of the leaf spring was about 500 N/mm. The safety factor of the spring was 1.25 for the material of Titanium T6-6Al-4V.
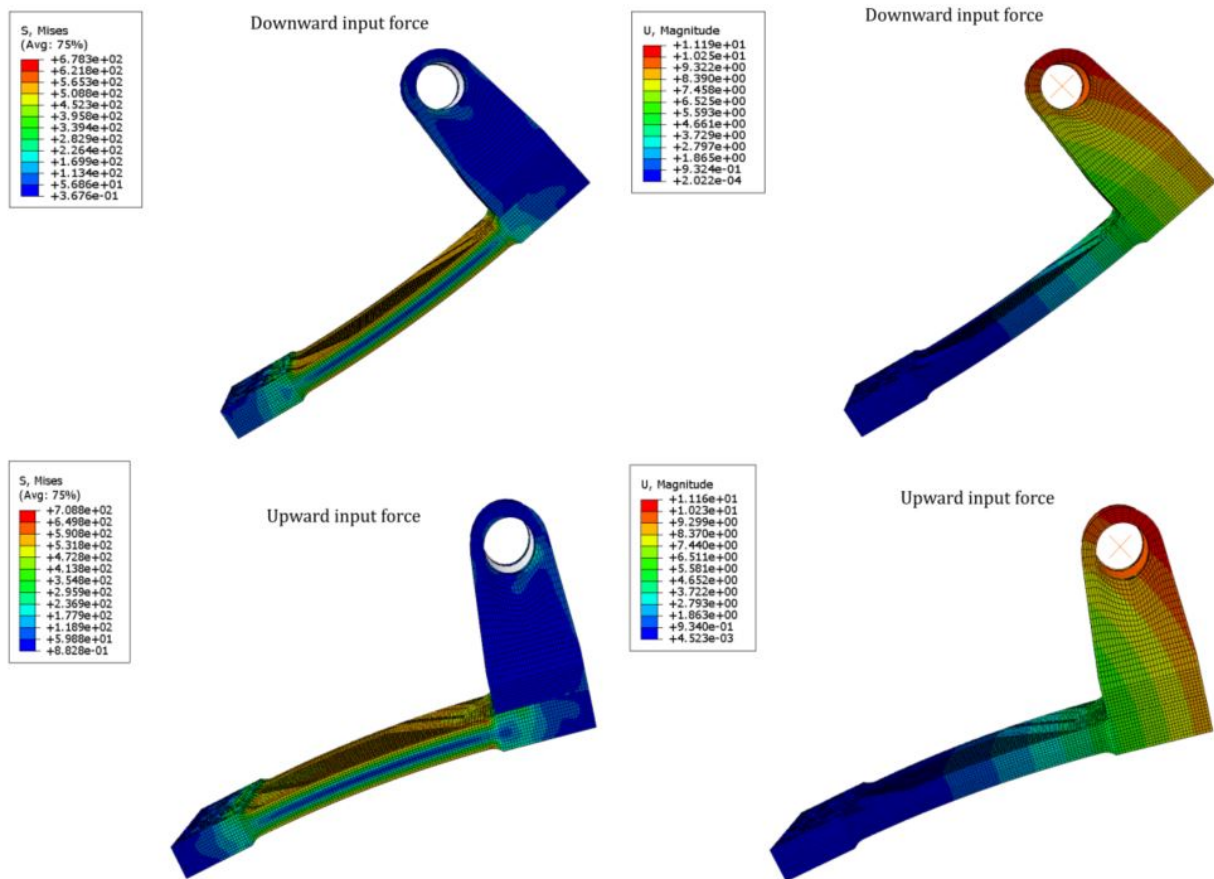
Figure 5.11: FEA results of the leaf spring in either force direction.

Lug and yoke

The lugs and yokes working as fixtures for the actuators were exerted by the input forces. Thus, it was critical to conduct FEA in these parts, in order to show the robustness. Fig.

5.12 shows the partitioned assemblies including the yaw yoke, the roll lug, and the yaw lug. Each part experienced the input force due to the actuator at each joint. The yaw yoke, which was bolted on the side of the yaw housing, provided support the universal joint. The yaw lug was bolted on the top base of the pitch housing. Both the yaw and roll lugs were used to support the trunnion that attached to the ball nut. All those bolts in assemblies were preloaded at the initial stage of the simulation and propagated with the external input force. Fig. 5.13 shows the FEA results of these parts. As expected, the highest stress concentrations were most around the holes. The safety factors for the yaw yoke and the roll lug were 1.43 and 2.09, respectively, when they were made in Aluminum 6061 T6. The safety factor for the yaw lug was 1.51 for the material of Aluminum 7075 T6.
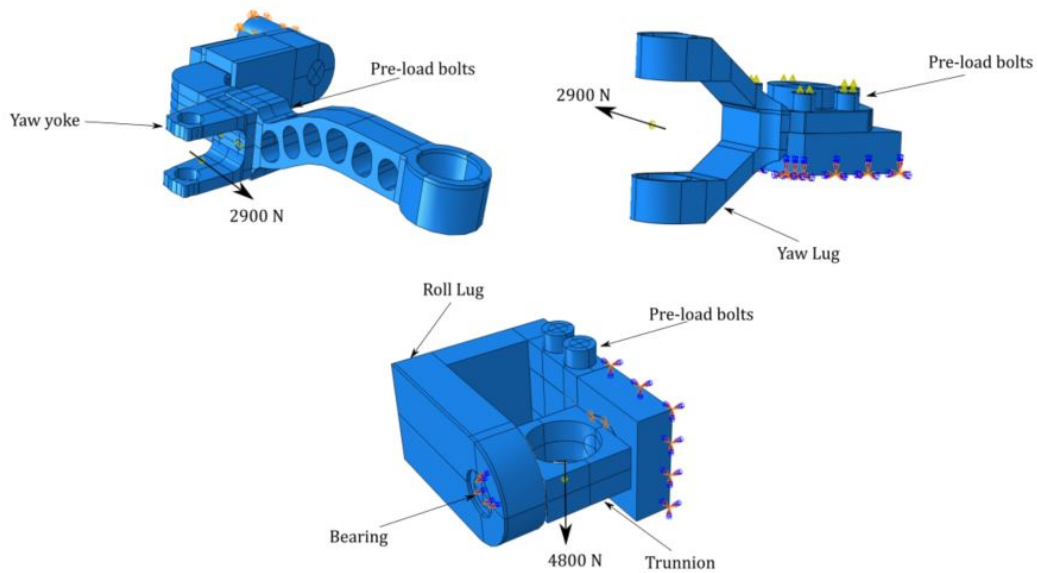
Figure 5.12: Assemblies of the yoke and lugs in ABAQUS window.
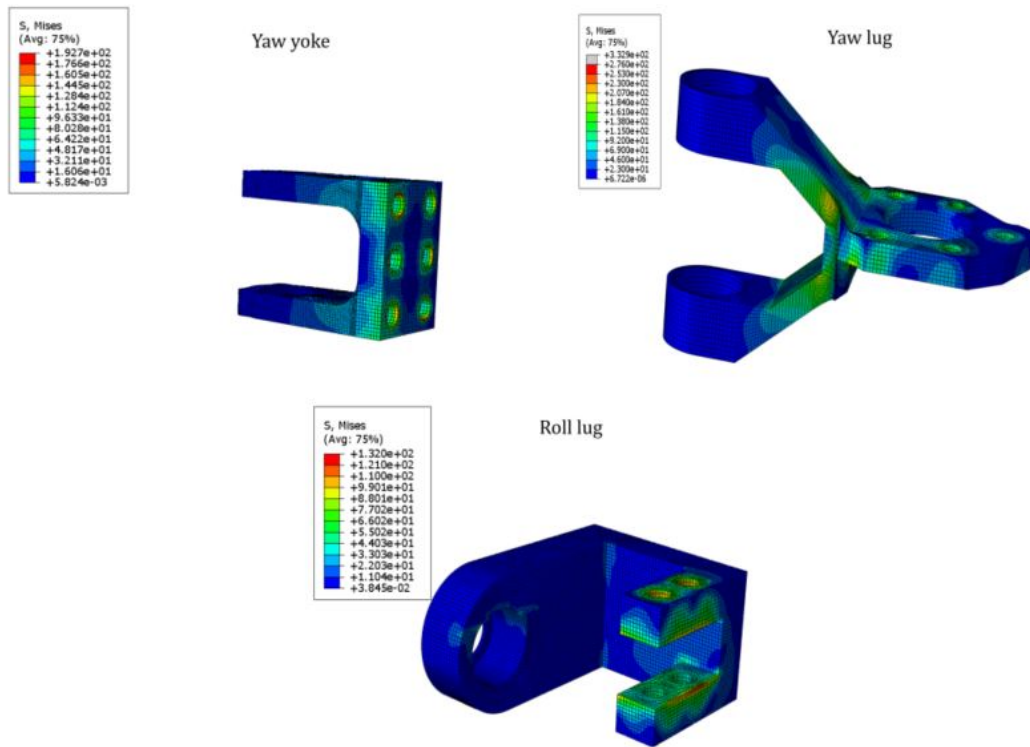
Figure 5.13: FEA results of the yoke and lugs.

5.2 Bolt Preload Documentation

Figuring out the amount of the bolts preload on the exoskeleton was necessary. There was a significant amount of the output torques at each joint. Therefore, it was significant to make sure that the external forces on the jointed design should not exceed the clamping forces by the fasteners. There were two types of reaction forces exerted on bolts: tension and shear. Bolts could experience the combination of these two types of reactions. In these cases, checking if the bolts would survive from the reaction loads was important as well. Proper bolts preload can help prevent fatigue failure, joint separation, and self-loose on jointed designs. In this section, the bolt preload on the critical exoskeleton structures was documented.

The online tool that was used to calculate the bolt preload was called Bolted Joint Analysis (BJA) [73]. It provided convenient calculations for the bolt analysis in jointed designs. For calculating reactions in bolt patterns, BJA required inputs of the external forces and the

coordinates of each bolt. Use the spring mount as an example. Fig. 5.14 shows the bolt pattern used to clamp the spring mount on the roll housing. The bolts in the spring mount experienced plenty of tension reactions because of the off-axis actuator input force. In the figure, the BJA generated the 2-D plane coordinates for each bolt and the input force. The generated results of the axial reaction loads are shown in Table 5.2. In order to overcome the reaction loads, 1, 2, 5, and 6 were chosen to be M8 bolts, and the suggested preload for them were 10,543 N, which gave a safety factor 1.26 for the shear force on the internal thread of the hole. 3 and 4 used M6 shoulder bolts because they only needed preload of 6,439 N, which provided a safety factor of 1.55 for not stripping the internal thread.
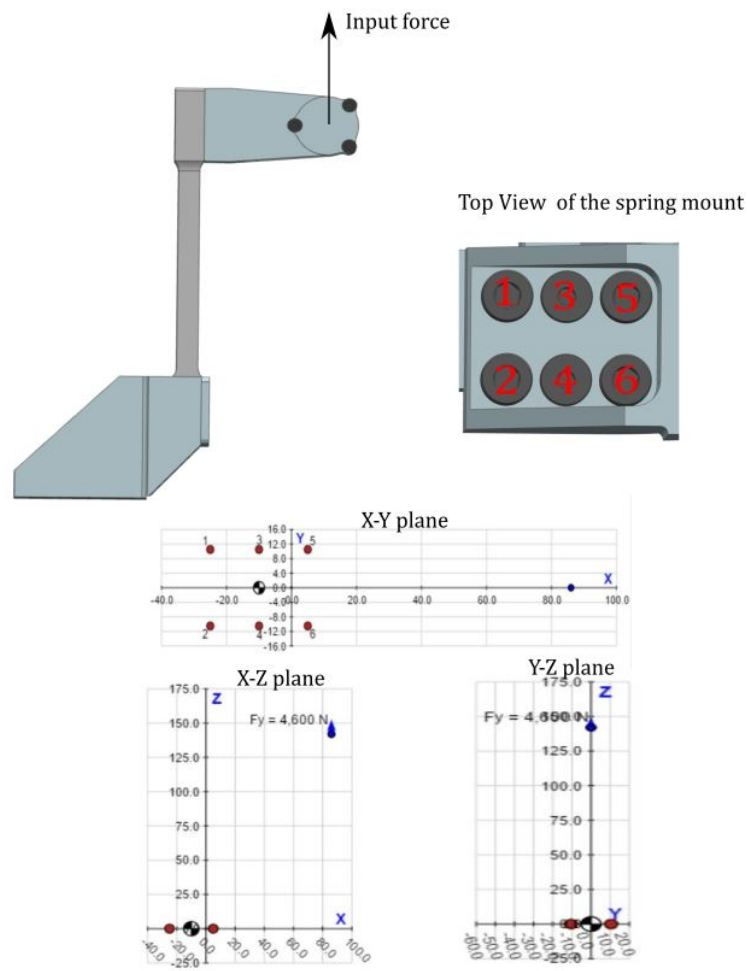
Figure 5.14: Bolts pattern on the spring mount with generated 2-D coordinate plane by BJA.

Table 5.2: Bolt preload results for the spring mount.

Bolt #	Axial Force (N)
1	-6,593
2	-6,593
3	766.17
4	766.17
5	8,127
6	8,127

Fig. 5.15 displays the results of bolt preloads for critical components of the exoskeleton. By using BJA tool, the generated required bolts preload and the safety factor for the internal thread are shown in Table 5.3.
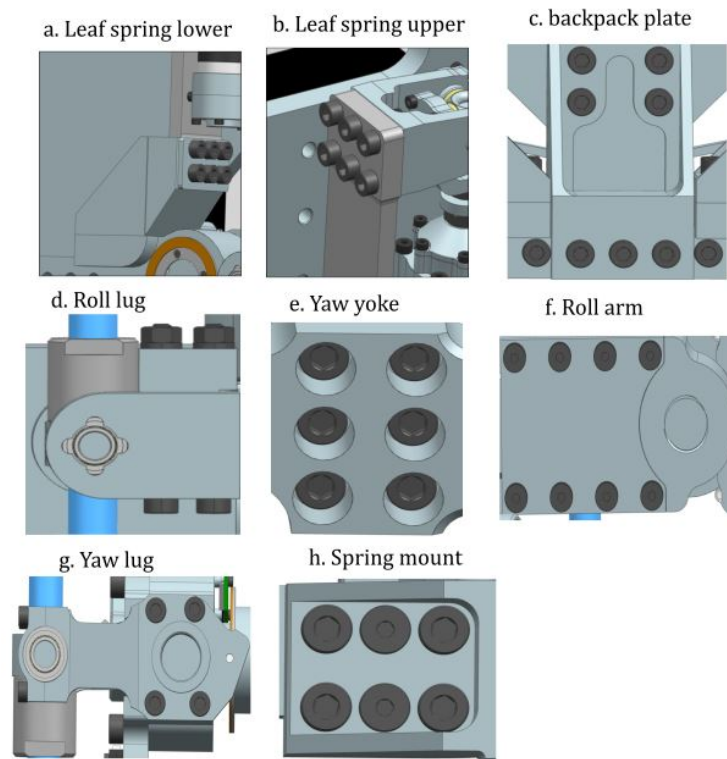
Figure 5.15: Critical bolted joints for each part.

Table 5.3: Summary of bolts preload (N) and safety factor (in parentheses) in Fig. 5.15.

Parts	M5	M6	M8
a	-	5,796 (1.25)	-
b	-	5,796 (1.37)	-
c	-	-	4,922 (2.64)
d	-	6,439 (3.54)	-
e	-	6,439 (1.4)	-
f	4,085 (1.19)	-	-
g	4,538 (1.58)	-	-
h	-	6,439 (1.55)	10,543 (1.26)

5.3 Fit Testing

In order to test the fitness and improve the design of the hip exoskeleton, 3D printing technology was used to print components of the exoskeleton. Those parts were printed with FDM technique on Lulzbot Taz 6 with PLA materials. Fig. 5.16 shows the initial version of the 3D printed prototype and the improved 3D printed prototype. There were major three problems found in the initial 3D printed prototype. In Fig. a, the external backpack frame was too close to the person so that the external frame bent when the person pushed on the backpack plate. This discomfort was caused by the curved feature of the frame support on the backpack plate. The recent version of the backpack plate as shown in Fig. 4.30 removed the curved feature and made the whole plate flat. The second problem was found in Fig. b, which showed that the yaw housing was not long enough to reach the joint of the person's leg. In order to solve this problem, a spacer (Fig. 4.31, the highlighted red part) was added in between the backpack plate and the roll housing. The spacer can be replaced with different thicknesses in order to fit for different sizes of operators. Finally, an unused space was found between the roll arm and the person's hip, as shown in Fig. c. In order to reduce this unused space, the roll arm was moved to the inside as well as the hard stops and the hip yaw housing, as shown in the top view of Fig. 4.26. The improved version of 3D printed prototype is shown in Fig. 5.17. For this prototype, each joint was installed with tapered roller bearings, hard stops, limit switches, and the encoders. In addition, the actuators were printed as well. The ball screw was prototyped with the same size of a rod. The improved version of 3D printed assembly showed that the harnessing used from the external backpack product was comfortable and convenient, and the 6 DoF of the exoskeleton worked well with the operator's joints.
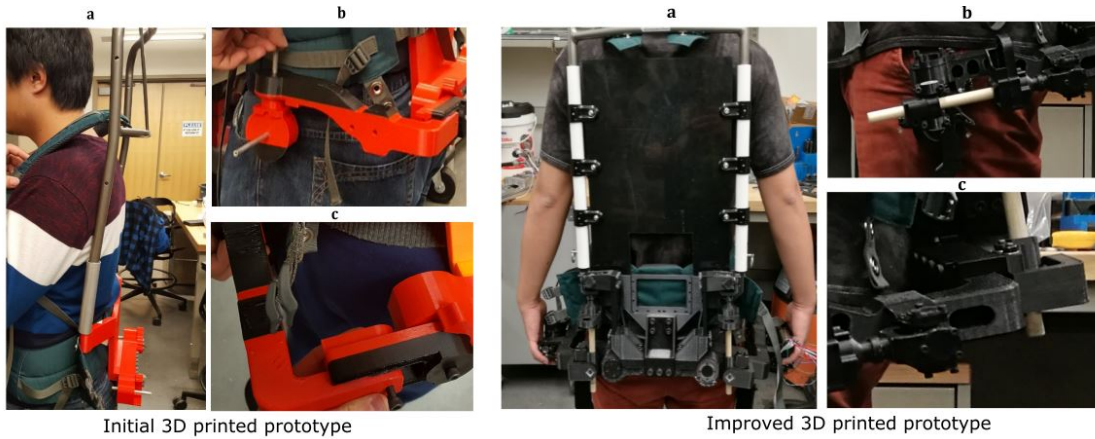
Figure 5.16: Improved 3D printed prototype with solved problems.
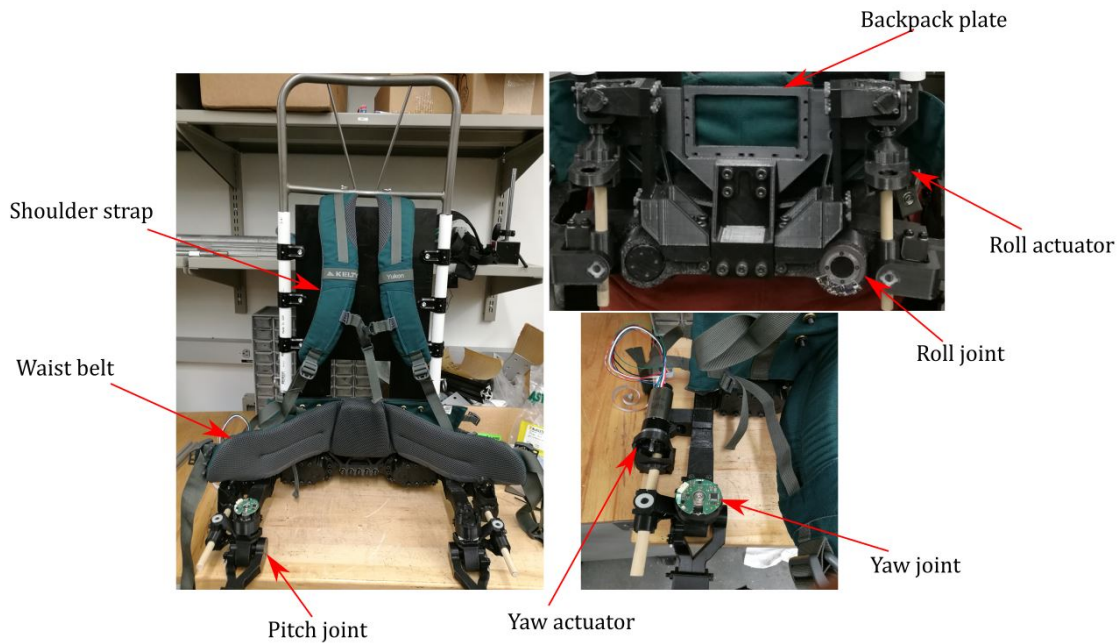
Figure 5.17: The recent version of a 3D printed prototype.

Fig. 5.18 shows each joint hit their limits of the movements, and at the meantime, the limit switches were triggered. The limit switches and hard stops were mounted in the positions as CAD modeled. According to the demonstrations of the prototype, each joint triggered the limit switches at the expected positions of the movements. Fig. 5.19 illustrates the two-bar linkage mechanism of the roll and yaw joints, respectively. As expected, each joint worked well with this linkage mechanism.
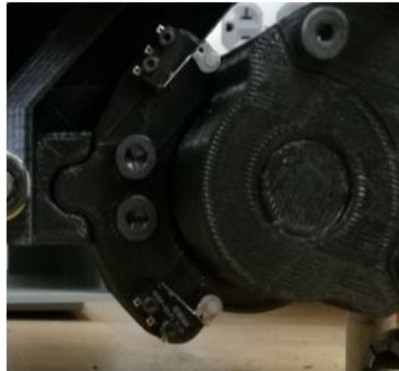
Figure 5.18: Joints limit of motion testing.
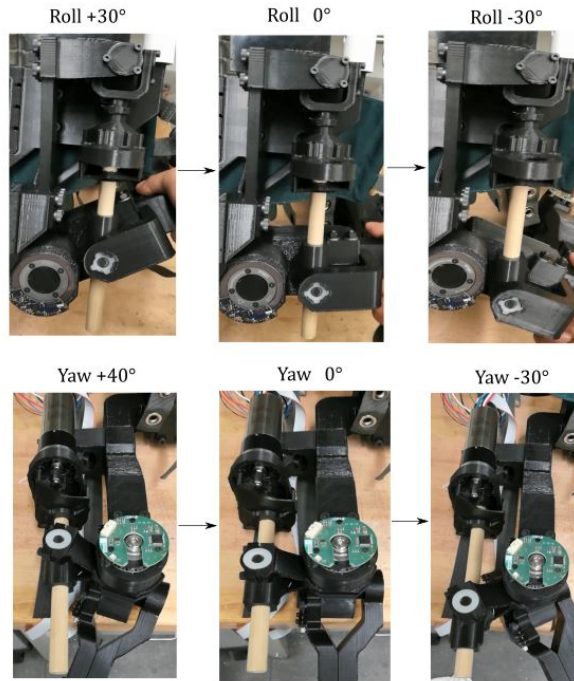
Figure 5.19: Roll and yaw linkages mechanism testing.

Finally, this prototype was worn to test the comfortability and each joint's configuration. Fig. 5.20 displays demonstrations of wearing the 3D printed prototype. The waist belt was worn close to the operator's waist, in order to match the roll joints at the person's hip. The shoulder straps attached to the external frame could be tightened to make the backpack plate firmly against the operator's back. Before putting on, it was necessary to measure the size of the person's hip breadth first, and then adjust the suit through the adustability features. The harnessing of the leg was not complete, so the simple buckle straps could not attach the prototype to the person's leg firmly. However, the prototype still proved that each joint position matched closely to the operator's, and the backpack harnessing was comfortable.

Figure 5.20: Experiments with wearing the 3D printed prototype.

Chapter 6

Conclusion

The design of the 6-DoF hip exoskeleton was aimed to provide design references for continuing the development of the lower level of the 12-DoF lower-body exoskeleton. In this thesis, a wearable 6-DoF hip exoskeleton was developed starting from the human data research to the prototype developments, mechanical designs and packagings, FEA simulations, and the 3D printed prototype demonstrations. The whole process can be a valuable experience for the future development of the exoskeleton project.

In summary, each joint has been designed and packaged with housings, selected bearings, encoders and hard stops. The range of motion of the roll joint was $\pm30°$, for the yaw joint was -30° to 40°, and for the pitch joint was -30° to 100°. LSEAs were packaged to power the roll joint, and a single-motor linear actuator was packaged to power the yaw joint. These two joints were both actuated using linear actuators with two-bar linkage mechanisms. The peak torque and velocity for the roll joint were 215.75 Nm and 1.25 rad/s, respectively, and for the yaw joint, the peak torque and velocity were 157.53 Nm and 1.70 rad/s, respectively. In the end, FEA was conducted on some critical components to ensure the strength of the whole structural design, and the functionalities of each joint design were tested with three wearable prototypes. As a result, the total weight of the hip exoskeleton without the hardware was 32.1 kg, which still left 15 kg from the weight budget to incorporate the other hardware, such as wiring, electronics, and cooling pumps.

6.1 Recommendations and Future Work

The major future work will focus on the development on packaging the hip pitch actuator and designing the structural frame that will be connected with the knee joint. The frame should be adjustable for accommodating to the different leg lengths. Also, FEA should be conducted in order to ensure the robustness of the pitch actuator fixtures and the frame structure. There are still needed improvements and developments on the harnessing. Adding paddings onto

the ABS plastic sheet can help prevent the bolt nuts from touching the operator's body. Also, the design of the harnessing for the leg frame should be firmly attached to the person's leg, in order to make sure the mobilities of the yaw and pitch joints to match with the person's hip joint.

The layout of electronics hardware on the backpack has not been finished yet, since some of the hardware still needs to be determined. The size of radiator shown in Fig. 4.31 was not finalized. Depending on the results of the motor cooling experiments, the radiator can be smaller. It is necessary to build all the CAD models of the hardware and put them onto the backpack assembly, in order to have an overview of packaging sizes.

Covers will be needed for the final product. The exoskeleton will be exposed to the environment for testing all the time. The dust or smoke can damage the system because of long-time exposure. Additionally, proper covers can help protect the exoskeleton from the impact in case of falls. The covers used on ESCHER was made of polystyrene, but those covers were comprised after the first fall on the competition [1, 74]. Therefore, it was necessary to design covers to protect vital areas. When covering on the electronics hardware, the operating temperature of the hardware should be analyzed [74]. Moreover, the covers should cover the pinch positions of the exoskeleton for protecting the operator. The pinch positions should be documented and analyzed to aid the design of the covers. Overall, covers should have properties of lightweight, waterproof, and not interfere with the mobility of the exoskeleton.

Bibliography

[1] C. Knabe, R. Griffin, J. Burton, G. Cantor-Cooke, L. Dantanarayana, G. Day, O. Ebeling-Koning, E. Hahn, M. Hopkins, J. Neal *et al.*, "Designing for compliance: Escher, team valors compliant biped," *Tech. Rep.*, 2015.

[2] C. S. Knabe, "Design of linear series elastic actuators for a humanoid robot," Master's thesis, Virginia Tech, 2015.

[3] A. B. Zoss, H. Kazerooni, and A. Chu, "Biomechanical design of the berkeley lower extremity exoskeleton (bleex)," *IEEE/ASME Transactions On Mechatronics*, vol. 11, no. 2, pp. 128–138, 2006.

[4] MatWeb, *Titanium Ti-6Al-4V (Grade 5), Annealed*, accessed: 2017-04-11. [Online]. Available: http://www.matweb.com/search/DataSheet.aspx?MatGUID= a0655d261898456b958e5f825ae85390&ckck=1

[5] A. Roaas and G. B. Andersson, "Normal range of motion of the hip, knee and ankle joints in male subjects, 30–40 years of age," *Acta Orthopaedica Scandinavica*, vol. 53, no. 2, pp. 205–208, 1982.

[6] W. G. Allread and E. W. Israelski, "Anthropometry and biomechanics," in *Handbook of Human Factors in Medical Device Design*. CRC Press, 2010, pp. 97–151.

[7] B. Appleton, "Stretching and flexibility," *Retrieved on May*, vol. 31, p. 2013, 1993.

[8] G. Karimi and O. Jahanian, *Genetic Algorithm Application in Swing Phase Optimization of AK Prosthesis with Passive Dynamics and Biomechanics Considerations*. IN-TECH Open Access Publisher, 2012.

[9] D. A. Winter, *Biomechanics and motor control of human movement*. John Wiley & Sons, 2009.

[10] S. Cho, J. Park, and O. Kwon, "Gender differences in three dimensional gait analysis data from 98 healthy korean adults," *Clinical biomechanics*, vol. 19, no. 2, pp. 145–152, 2004.

[11] G. K. Seidel, D. M. Marchinda, M. Dijkers, and R. W. Soutas-Little, "Hip joint center location from palpable bony landmarksa cadaver study," *Journal of biomechanics*, vol. 28, no. 8, pp. 995–998, 1995.

[12] G. Daysal, B. Goker, E. Gonen, M. Demirag, S. Haznedaroglu, M. Ozturk, and J. Block, "The relationship between hip joint space width, center edge angle and acetabular depth," *Osteoarthritis and Cartilage*, vol. 15, no. 12, pp. 1446–1451, 2007.

[13] MatWeb, *MatWeb*, accessed: 2017-06-13. [Online]. Available: http://www.matweb.com/index.aspx

[14] G. Colombo, M. Wirz, and V. Dietz, "Driven gait orthosis for improvement of locomotor training in paraplegic patients." *Spinal cord*, vol. 39, no. 5, 2001.

[15] A. Esquenazi, M. Talaty, A. Packel, and M. Saulino, "The rewalk powered exoskeleton to restore ambulatory function to individuals with thoracic-level motor-complete spinal cord injury," *American journal of physical medicine & rehabilitation*, vol. 91, no. 11, pp. 911–921, 2012.

[16] A. Tsukahara, Y. Hasegawa, and Y. Sankai, "Gait support for complete spinal cord injury patient by synchronized leg-swing with hal," in *Intelligent Robots and Systems (IROS), 2011 IEEE/RSJ International Conference on*. IEEE, 2011, pp. 1737–1742.

[17] R. J. Farris, H. A. Quintero, T. J. Withrow, and M. Goldfarb, "Design of a joint-coupled orthosis for fes-aided gait," in *Rehabilitation Robotics, 2009. ICORR 2009. IEEE International Conference on*. IEEE, 2009, pp. 246–252.

[18] A. Chu, H. Kazerooni, and A. Zoss, "On the biomimetic design of the berkeley lower extremity exoskeleton (bleex)," in *Robotics and Automation, 2005. ICRA 2005. Proceedings of the 2005 IEEE International Conference on*. IEEE, 2005, pp. 4345–4352.

[19] J. W. McDonald and C. Sadowsky, "Spinal-cord injury," *The Lancet*, vol. 359, no. 9304, pp. 417–425, 2002.

[20] K. A. Curtis, G. A. Drysdale, R. D. Lanza, M. Kolber, R. S. Vitolo, and R. West, "Shoulder pain in wheelchair users with tetraplegia and paraplegia," *Archives of physical medicine and rehabilitation*, vol. 80, no. 4, pp. 453–457, 1999.

[21] E. G. Pearson, P. W. Nance, W. D. Leslie, and S. Ludwig, "Cyclical etidronate: its effect on bone density in patients with acute spinal cord injury," *Archives of physical medicine and rehabilitation*, vol. 78, no. 3, pp. 269–272, 1997.

[22] J. Wall, "Preventing pressure sores among wheelchair users." *Professional nurse (London, England)*, vol. 15, no. 5, pp. 321–324, 2000.

[23] D. F. Lahr, "Design and control of a bipedal robot," Ph.D. dissertation, Virginia Polytechnic Institute and State University, 2014.

[24] B. K. T.-S. Lee, "Design of a humanoid robot for disaster response," Ph.D. dissertation, Virginia Tech, 2014.

[25] M. Vukobratovic, D. Hristic, and Z. Stojiljkovic, "Development of active anthropomorphic exoskeletons," *Medical and Biological Engineering*, vol. 12, no. 1, pp. 66–80, 1974.

[26] Y. Sankai, "Leading edge of cybernics: Robot suit hal," in *SICE-ICASE, 2006. International Joint Conference.* IEEE, 2006, pp. P–1.

[27] ——, *HAL: Hybrid Assistive Limb Based on Cybernics.* Berlin, Heidelberg: Springer Berlin Heidelberg, 2011, pp. 25–34. [Online]. Available: http://dx.doi.org/10.1007/978-3-642-14743-2_3

[28] T. Hayashi, H. Kawamoto, and Y. Sankai, "Control method of robot suit hal working as operator's muscle using biological and dynamical information," in *Intelligent Robots and Systems, 2005.(IROS 2005). 2005 IEEE/RSJ International Conference on.* IEEE, 2005, pp. 3063–3068.

[29] H. Kawamoto and Y. Sankai, "Comfortable power assist control method for walking aid by hal-3," in *Systems, Man and Cybernetics, 2002 IEEE International Conference on*, vol. 4. IEEE, 2002, pp. 6–pp.

[30] S. Lee and Y. Sankai, "Power assist control for walking aid with hal-3 based on emg and impedance adjustment around knee joint," in *Intelligent Robots and Systems, 2002. IEEE/RSJ International Conference on*, vol. 2. IEEE, 2002, pp. 1499–1504.

[31] ——, "Power assist control for leg with hal-3 based on virtual torque and impedance adjustment," in *Systems, Man and Cybernetics, 2002 IEEE International Conference on*, vol. 4. IEEE, 2002, pp. 6–pp.

[32] H. Kawamoto, S. Kanbe, and Y. Sankai, "Power assist method for hal-3 estimating operator's intention based on motion information," in *Robot and human interactive communication, 2003. proceedings. ROMAN 2003. The 12th IEEE international workshop on.* IEEE, 2003, pp. 67–72.

[33] H. Kawamoto, S. Lee, S. Kanbe, and Y. Sankai, "Power assist method for hal-3 using emg-based feedback controller," in *Systems, Man and Cybernetics, 2003. IEEE International Conference on*, vol. 2. IEEE, 2003, pp. 1648–1653.

[34] S. Lee and Y. Sankai, "The natural frequency-based power assist control for lower body with hal-3," in *Systems, Man and Cybernetics, 2003. IEEE International Conference on*, vol. 2. IEEE, 2003, pp. 1642–1647.

[35] H. Kawamoto and Y. Sankai, "Power assist method based on phase sequence driven by interaction between human and robot suit," in *Robot and Human Interactive Communication, 2004. ROMAN 2004. 13th IEEE International Workshop on.* IEEE, 2004, pp. 491–496.

[36] ——, "Power assist method based on phase sequence and muscle force condition for hal," *Advanced Robotics*, vol. 19, no. 7, pp. 717–734, 2005.

[37] A. Chu, H. Kazerooni, and A. Zoss, "On the biomimetic design of the berkeley lower extremity exoskeleton (bleex)," in *Robotics and Automation, 2005. ICRA 2005. Proceedings of the 2005 IEEE International Conference on.* IEEE, 2005, pp. 4345–4352.

[38] J. Ghan and H. Kazerooni, "System identification for the berkeley lower extremity exoskeleton (bleex)," in *Robotics and Automation, 2006. ICRA 2006. Proceedings 2006 IEEE International Conference on.* IEEE, 2006, pp. 3477–3484.

[39] H. Kazerooni, R. Steger, and L. Huang, "Hybrid control of the berkeley lower extremity exoskeleton (bleex)," *The International Journal of Robotics Research*, vol. 25, no. 5-6, pp. 561–573, 2006.

[40] H. Kazerooni, J.-L. Racine, L. Huang, and R. Steger, "On the control of the berkeley lower extremity exoskeleton (bleex)," in *Robotics and automation, 2005. ICRA 2005. Proceedings of the 2005 IEEE international conference on.* IEEE, 2005, pp. 4353–4360.

[41] H. Kazerooni, A. Chu, and R. Steger, "That which does not stabilize, will only make us stronger," *The International Journal of Robotics Research*, vol. 26, no. 1, pp. 75–89, 2007.

[42] R. Steger, S. H. Kim, and H. Kazerooni, "Control scheme and networked control architecture for the berkeley lower extremity exoskeleton (bleex)," in *Robotics and Automation, 2006. ICRA 2006. Proceedings 2006 IEEE International Conference on.* IEEE, 2006, pp. 3469–3476.

[43] R. V. Ham, T. G. Sugar, B. Vanderborght, K. W. Hollander, and D. Lefeber, "Compliant actuator designs," *IEEE Robotics Automation Magazine*, vol. 16, no. 3, pp. 81–94, September 2009.

[44] J. Pratt, B. Krupp, and C. Morse, "Series elastic actuators for high fidelity force control," *Industrial Robot: An International Journal*, vol. 29, no. 3, pp. 234–241, 2002.

[45] J. E. Pratt and B. T. Krupp, "Series elastic actuators for legged robots," *Proc. SPIE*, vol. 5422, pp. 135–144, 2004.

[46] T. Morita and S. Sugano, "Design and development of a new robot joint using a mechanical impedance adjuster," in *Robotics and Automation, 1995. Proceedings., 1995 IEEE International Conference on*, vol. 3. IEEE, 1995, pp. 2469–2475.

[47] A. De and U. Tasch, "A two-dof manipulator with adjustable compliance capabilities and comparison with the human finger," *Journal of Field Robotics*, vol. 13, no. 1, pp. 25–34, 1996.

[48] S. Kawamura, T. Yamamoto, D. Ishida, T. Ogata, Y. Nakayama, O. Tabata, and S. Sugiyama, "Development of passive elements with variable mechanical impedance for wearable robots," in *Robotics and Automation, 2002. Proceedings. ICRA'02. IEEE International Conference on*, vol. 1. IEEE, 2002, pp. 248–253.

[49] C. Casavola, C. Pappalettere, and F. Tattoli, "Experimental and numerical study of static and fatigue properties of titanium alloy welded joints," *Mechanics of Materials*, vol. 41, no. 3, pp. 231 – 243, 2009.

[50] L. Hangzhou Speedway Import & Export Co., *Hangzhou Speedway Import & Export Co., Ltd.*, accessed: 2017-07-12. [Online]. Available: http://www.cnspeedway.com/

[51] C. DRUGA, C. RADU, D. BARBU, and I. SERBAN, "Determination of dynamical parameters of the human gait using force plate," 2009.

[52] C. L. Vaughan, B. L. Davis, and J. C. O'connor, *Dynamics of human gait.* Human Kinetics Publishers Champaign, Illinois, 1992, vol. 2.

[53] V. Inman, H. Ralston, and F. Todd, "Human walkingwilliams and wilkins," *Baltimore, London*, 1981.

[54] M. Hartmann, F. Kreuzpointner, R. Haefner, H. Michels, A. Schwirtz, and J. Haas, "Effects of juvenile idiopathic arthritis on kinematics and kinetics of the lower extremities call for consequences in physical activities recommendations," *International journal of pediatrics*, vol. 2010, 2010.

[55] M. Iosa, A. Fusco, F. Marchetti, G. Morone, C. Caltagirone, S. Paolucci, and A. Peppe, "The golden ratio of gait harmony: repetitive proportions of repetitive gait phases," *BioMed research international*, vol. 2013, 2013.

[56] C. Mummolo, L. Mangialardi, and J. H. Kim, "Quantifying dynamic characteristics of human walking for comprehensive gait cycle," *Journal of biomechanical engineering*, vol. 135, no. 9, p. 091006, 2013.

[57] T. Bhosale, H. Kudale, V. Kumthekar, S. Garude, and P. Dhumal, "Gait analysis using wearable sensors," in *Energy Systems and Applications, 2015 International Conference on.* IEEE, 2015, pp. 267–269.

[58] T. Kodek and M. Munih, "An identification technique for evaluating body segment parameters in the upper extremity from manipulator-hand contact forces and arm kinematics," *Clinical Biomechanics*, vol. 21, no. 7, pp. 710–716, 2006.

[59] W. S. Erdmann, "Geometry and inertia of the human body-review of research," *Acta of Bioengineering and biomechanics*, vol. 1, no. 1, pp. 23–35, 1999.

[60] W. T. Dempster, "Space requirements of the seated operator: geometrical, kinematic, and mechanical aspects of the body, with special reference to the limbs," 1955.

[61] R. N. Hinrichs, "Adjustments to the segment center of mass proportions of clauser et al.(1969)," *Journal of Biomechanics*, vol. 23, no. 9, pp. 949–951, 1990.

[62] G. Robertson, G. Caldwell, J. Hamill, G. Kamen, and S. Whittlesey, *Research methods in biomechanics, 2E.* Human Kinetics, 2013.

[63] W. T. Dempster, W. C. Gabel, and W. J. Felts, "The anthropometry of the manual work space for the seated subject," *American journal of physical anthropology*, vol. 17, no. 4, pp. 289–317, 1959.

[64] R. Drillis, R. Contini, and M. Bluestein, *Body segment parameters.* New York University, School of Engineering and Science Research Division, NY, 1966.

[65] M. R. Yeadon and M. Morlock, "The appropriate use of regression equations for the estimation of segmental inertia parameters," *Journal of biomechanics*, vol. 22, no. 6-7, pp. 683–689, 1989.

[66] J. Bellemans, W. Colyn, H. Vandenneucker, and J. Victor, "The chitranjan ranawat award: is neutral mechanical alignment normal for all patients?: the concept of constitutional varus," *Clinical Orthopaedics and Related Research®*, vol. 470, no. 1, pp. 45–53, 2012.

[67] Anthropometry, *Chapter 2-Definition and applicability of anthropometric data*, accessed: 2017-04-11. [Online]. Available: http://personal.cityu.edu.hk/~meachan/Online%20Anthropometry/Chapter2/Ch2-19.htm

[68] S. S. R. company, *SMALLEY*, accessed: 2017-07-12. [Online]. Available: http://www.smalley.com/

[69] KELTY, *SANITAS 34*, accessed: 2017-07-12. [Online]. Available: https://kelty.com/sanitas-34/

[70] J. Brown, "Characterization of msc/nastran & msc/abaqus elements for turbine engine blade frequency analysis," in *Proc. MSC Aerospace Users' Conference.* Citeseer, 1997.

[71] S. Selamet and M. Garlock, "Guidelines for modeling three dimensional structural connection models using finite element methods," in *International Symposium: Steel Structures: Culture & Sustainability*, 2010.

[72] E. Q. Sun, "Shear locking and hourglassing in msc nastran, abaqus, and ansys," in *Msc software users meeting*, 2006.

[73] MechaniCalc, *Bolted Joint Analysis*, accessed: 2017-06-30. [Online]. Available: https://mechanicalc.com/calculators/bolted-joint-analysis/

[74] J. M. Seminatore, "Upper body design of a humanoid robot for the darpa robotics challenge," Ph.D. dissertation, Virginia Tech, 2016.

Appendix A

Figure 1.1

test of

Fair Use Factor	In Favor of Fair Use	In Favor of Copyright Holder (not fair use)
Purpose and Character of Use		
commercial or educational use for profit or not	X Research	Commercial activity
	X Scholarship	Profit (monetarily) from use
degree of transformation; value added	X Nonprofit university	Entertainment
for criticism, commentary, news reporting, teaching, scholarship, research	Criticism	Bad-faith behavior
	X Comment	Denying credit to original author
	Transformative: changes the original work for new purpose	
	Parody	
Nature of the Copyrighted Work		
character of the work	X Published work	Unpublished work
for example, fact or fiction	X Factual or non-fiction based	Highly creative work (art, music, novels, films, plays)
worthy of (extensive) protection?	Important to favored educational objectives	Fiction
Amount and Substantiality		
use only what's necessary	X Small quantity of the work	Large poprtion or whole work used
quantity and quality in relation to the whole work	X Portion used is not central or significant to entire work	Portion used is central to work or "heart of the work"
	Amount is appropriate for favored educational purpose	
Effect		
harm to potential market or value of a work after a portion has been used separately from the whole	X User has lawfully acquired copy of the original work	Could replace sale of copyrighted work
	X One or fewer copies made	Significantly impairs market or potential market for copyright work or derivative
	X No significant effect o the market or potential market of copyrighted work	Reasonably available licensing mechanism for use of the copyrighted work
	X No similar product marketed by the copyright holder	Affordable permission available for using work
	Lack of licensing mechanism	Numerous copies made
		X You made it accessible on Web or in other public forum
		Repeated or long term use

Figure A1: A test of fair use for Figure 1.1.

Figure 2.1

As a test of fair use in ETDs at Virginia Tech: _____
test of

Fair Use Factor	In Favor of Fair Use		In Favor of Copyright Holder (not fair use)
Purpose and Character of Use			
commercial or educational use	X	Research	Commercial activity
for profit or not	X	Scholarship	Profit (monetarily) from use
degree of transformation; value added	X	Nonprofit university	Entertainment
for criticism, commentary, news reporting, teaching, scholarship, research		Criticism	Bad-faith behavior
	X	Comment	Denying credit to original author
		Transformative: changes the original work for new purpose	
		Parody	
Nature of the Copyrighted Work			
character of the work	X	Published work	Unpublished work
for example, fact or fiction	X	Factual or non-fiction based	Highly creative work (art, music, novels, films, plays)
worthy of (extensive) protection?		Important to favored educational objectives	Fiction
Amount and Substantiality			
use only what's necessary	X	Small quantity of the work	Large poprtion or whole work used
quantity and quality in relation to the whole work	X	Portion used is not central or significant to entire work	Portion used is central to work or "heart of the work"
		Amount is appropriate for favored educational purpose	
Effect			
harm to potential market or value of a work after a portion has been used separately from the whole	X	User has lawfully acquired copy of the original work	Could replace sale of copyrighted work
	X	One or fewer copies made	Significantly impairs market or potential market for copyright work or derivative
	X	No significant effect o the market or potential market of copyrighted work	Reasonably available licensing mechanism for use of the copyrighted work
	X	No similar product marketed by the copyright holder	Affordable permission available for using work
		Lack of licensing mechanism	Numerous copies made
			X You made it accessible on Web or in other public forum
			Repeated or long term use

Figure A2: A test of fair use for Figure 2.1.

Figure 3.2 (left picture)

As a test of fair use in ETDs at Virginia Tech: _____

test of

Fair Use Factor		In Favor of Fair Use		In Favor of Copyright Holder (not fair use)
Purpose and Character of Use				
commercial or educational use	X	Research		Commercial activity
for profit or not	X	Scholarship		Profit (monetarily) from use
degree of transformation; value added	X	Nonprofit university		Entertainment
for criticism, commentary, news reporting, teaching, scholarship, research	X	Criticism		Bad-faith behavior
	X	Comment		Denying credit to original author
	X	Transformative: changes the original work for new purpose		
		Parody		
Nature of the Copyrighted Work				
character of the work	X	Published work		Unpublished work
for example, fact or fiction	X	Factual or non-fiction based		Highly creative work (art, music, novels, films, plays)
worthy of (extensive) protection?		Important to favored educational objectives		Fiction
Amount and Substantiality				
use only what's necessary	X	Small quantity of the work		Large poprtion or whole work used
quantity and quality in relation to the whole work	X	Portion used is not central or significant to entire work		Portion used is central to work or "heart of the work"
		Amount is appropriate for favored educational purpose		
Effect				
harm to potential market or value of a work after a portion has been used separately from the whole	X	User has lawfully acquired copy of the original work		Could replace sale of copyrighted work
	X	One or fewer copies made		Significantly impairs market or potential market for copyright work or derivative
	X	No significant effect o the market or potential market of copyrighted work		Reasonably available licensing mechanism for use of the copyrighted work
	X	No similar product marketed by the copyright holder		Affordable permission available for using work
		Lack of licensing mechanism		Numerous copies made
			X	You made it accessible on Web or in other public forum
				Repeated or long term use

Figure A3: A test of fair use for Figure 3.2